

# **Corrosion and scaling in utilization of geothermal energy in the Upper Rhine graben**

Zur Erlangung des akademischen Grades eines  
DOKTORS DER NATURWISSENSCHAFTEN

von der Fakultät für  
Bauingenieur, Geo- und Umweltwissenschaften

des Karlsruher Instituts für Technologie (KIT)

genehmigte

DISSERTATION

von

Dipl.-Geol. Niklas Mundhenk

aus Hamburg

Tag der mündlichen

Prüfung: 09.12.13

Referent: Prof. Dr. rer. nat. Thomas Kohl

Korreferent: Prof. Dr. Dieter Landolt

Karlsruhe (2013)



## Abstract

Geothermal energy can contribute a significant portion of electricity to the future energy mix. However, technical challenges towards a viable use of these virtually infinite resources remain unsolved. In Germany and France, the Upper Rhine graben (URG) offers favorable conditions for geothermal utilization and several projects emerged in the last decades producing electricity in binary-type power plants (e.g. Soultz and Bruchsal). With the kind permission of the operators, GEIE and EnBW AG, we had the possibility to access these geothermal sites, to use on-site instrumentation and to sample brine for analysis and laboratory experiments. The geothermal waters are extracted with temperatures  $>120\text{ }^{\circ}\text{C}$  from deep water-saturated rock formations (depths  $> 2.5\text{ km}$ ) and are usually highly saline, which is why they are often referred to as geothermal brines. The salinity of brines from different sites often exceeds  $100\text{ g l}^{-1}$ .

An *in situ* physicochemical monitoring program has been performed in Soultz. It identifies Na, Ca, and Cl as the main constituents of the brine, contributing to more than 95% of the total salinity ( $\text{TDS} \approx 98\text{ g l}^{-1}$ ). K, Mg,  $\text{SO}_4$ , Br, B,  $\text{NH}_4$ , Li, and Sr contribute to the overall chemistry in stable amounts. F, Ba, Ti, As, Rb, Cs, Fe, Ni, Cu, Co, Cr, Cd, Zn, Ag, and Pb are present in unstable concentrations. The presence of  $\text{CO}_2$  as a dissolved gas phase increases the acidity to a pH less than 5.

The chemical characteristics in combination with elevated temperatures account for a high corrosivity of these brines and common construction materials are often challenged. Usually, metallic construction materials are used for the components, such as the production pump, the heat exchanger etc. The aim of this experimental approach is to understand the interaction between various construction metals and different brines in *in situ* and simulated (laboratory) brine environments by using different techniques of corrosion research (weight loss and electrochemical methods).

The outcome of this research campaign can be subdivided in rather fundamental aspects and in rather practical finding. Fundamental means that observations can now be comprehended by basic processes on the brine-electrolyte interface. Practical means, that results and experiences can be implemented in existing systems in order to enhance the integrity of components.

Following conclusions could be drawn from corrosion experiments. Mild steels (**P110**, **N80**, **P235GH**, and **P265GH**) suffer long-term uniform corrosion rates below  $0.2\text{ mm y}^{-1}$  in  $80\text{ }^{\circ}\text{C}$  Soultz brine, which corresponds to a wall thickness reduction of less than 4 mm within 20 years of service life. Both, autoclave and *in situ* exposure experiments lead to the formation of a corrosion scale, mainly composed of siderite.

Generally, this layer lowers the corrosion intensity over time. However, incomplete of loose coverage may lead to localized forms with considerable depths (>1 mm), such as filiform corrosion.

Autoclave exposure experiments in Soultz brine with different temperatures (20, 80, and 160 °C) reveal a complex interaction between corrosion and scaling on mild steel coupons. Both, temperature and time play a significant role. A decrease of the corrosion rate over time documents the precipitation of siderite and the build-up of a successively adherent and dense layer. The highest corrosion rate was discerned in the 80 °C environment and a local corrosion rate maximum below 100 °C is therefore hypothesized.

The newly formed siderite layer has a rough surface and provides the substrate for brine-related scaling (e.g. Ba/Sr-sulfates and Pb-sulfides). The potentially toxic and radioactive nature of these deposits has consequences for cleaning procedures and disposal.

Alloys and non-ferrous metals corrode to a much lower extent than mild steels and only a weak scale adherency could be observed. Conventional stainless steels Cr-stainless steel **430F** and CrNiMo stainless steel **316L** undergo pitting corrosion in 80 °C environments, mainly associated with chemical heterogeneities. Manganese sulfide inclusions in the **430F** microstructure act as preferred pit initiation sites. Post-exposure coupons of **316L** also show pitting on open surfaces. The exposure results could partly be corroborated by electrochemical techniques. Deficient passivity is indicated by an unsteady *OCP* evolution with massive drops and short-term fluctuations (activation/passivation changes). The open circuit potential *OCP* strongly approaches the repassivation potential  $E_R$  and leads to metastable, or even stable, pitting. Higher-alloyed stainless steels **904L** and **318LN** do not undergo pitting corrosion in the 80 °C exposure environment but electrochemical measurements indicate that these alloys are also challenged to suffer spontaneous pitting. In case of a “zero-corrosion allowance” high-strength CrNiMo alloys with a  $PREN > 36$  or non-ferrous materials, e.g. Titanium, have to be chosen. These alloys spontaneously passivate in the test environment and even in case of corrosion it would occur in a uniform manner.

## Zusammenfassung

Die Geothermie kann einen signifikanten Beitrag zur zukünftigen Stromgewinnung liefern. Jedoch stehen technische Herausforderungen einer nachhaltigen und sicheren Nutzung dieser praktisch unerschöpflichen Energiequelle im Wege. Aufgrund eines erhöhten Wärmeflusses bietet der Oberrheingraben günstige Bedingungen für eine geothermische Stromproduktion und mehrere (Binär-) Kraftwerke entstanden in den letzten Jahren, sowohl auf der deutschen als auch auf der französischen Seite (z. B. Soultz-sous-Forêts, Bruchsal). Mit freundlicher Genehmigung der Betreiber GEIE und EnBW AG konnten vor Ort Experimente durchgeführt werden, sowie Proben für Analysen und Laborexperimente genommen werden. Die Geothermalwässer werden mit einer Temperatur von  $>120\text{ °C}$  aus einer Tiefe von mehr als 2.5 km gefördert. Aufgrund ihres hohen Salzgehalts von häufig mehr als  $100\text{ g l}^{-1}$  handelt sich bei den Wässern um Solen.

Diese Arbeit beinhaltet ein *in situ* Monitoringprogramm des Geothermalwassers in Soultz, welches einzigartig für einen Oberrheingrabenstandort ist und eine detaillierte physiko-chemikalische Charakterisierung ermöglicht. Na, Ca und Cl sind die Hauptionen und tragen zu mehr als 95% zur Gesamtlösungsfracht (ca.  $98\text{ g l}^{-1}$ ) bei. K, Mg,  $\text{SO}_4$ , Br, B,  $\text{NH}_4$ , Li und Sr sind ebenfalls in konstanten Konzentrationen enthalten. Die Konzentrationen von F, Ba, Ti, As, Rb, Cs, Fe, Ni, Cu, Co, Cr, Cd, Zn, Ag und Pb sind sehr schwankend. Hinzu kommen hohe Konzentrationen an gelöstem  $\text{CO}_2$ , welches den pH-Wert unter 5 absenkt.

Die chemische Zusammensetzung in Kombination mit der hohen Temperatur bewirkt eine hohe Korrosivität gegenüber den eingesetzten Werkstoffen. Üblicherweise werden für die Komponenten (z.B. die Pumpe, der Wärmetauschen etc.) metallische Werkstoffe, wie Stähle und Legierungen eingesetzt. Ziel dieser Arbeit ist das Verständnis der Wechselwirkung zwischen gängigen Konstruktionswerkstoffen und Geothermalwässern in simulierten und *in situ* Korrosionsumgebungen. Hierbei sind sowohl konventionelle Auslagerungsversuche (Massenverlustbestimmung) als auch elektrochemische Methoden (Korrosionspotentialmessungen und potentiodynamische Polarisation) zum Einsatz gekommen.

Die Beobachtungen dieser Arbeit können in eher grundlegende als auch in praktische Ergebnisse unterteilt werden. Grundlegend in dem Sinne, als dass zugrunde liegende Prozesse nun besser nachvollzogen werden können. Praktisch in dem Sinne, als dass die Beobachtungen in existierenden Anlagen implementiert werden können. Die Arbeit gibt Grundlagen, technische Informationen, Erfahrungen und Strategien, die zu

einem sicheren Betrieb von Geothermieranlagen beitragen können. Zudem können die Ergebnisse bei der Materialauswahl für anspruchsvolle Geothermieranwendungen dienen.

Aus den Korrosionsexperimenten konnten folgende Schlussfolgerungen gezogen werden. Gleichförmiger Abtrag ist die dominante Form der Korrosion von unlegierten Baustählen, wobei die Rate bei unter 0.2 mm/Jahr liegt. Über eine 20-jährige Laufzeit würde dies eine maximale Wandstärkenreduzierung von 4 mm bedeuten. *In situ* Auslagerung führt zur Bildung von Siderit, der die Korrosionsintensität über die Zeit mindert und eine Art Passivschicht darstellt. Jedoch erhöht die Bedeckung mit Siderit die Gefahr von lokaler Korrosion (u.a. filiforme Korrosion), die Eindringtiefen von mehr als 1 mm erreichen kann.

Auslagerungsexperimente wurde mit Baustählen in Soultzwasser bei unterschiedlichen Temperaturen (20, 80, 160 °C) durchgeführt. Diese zeigen einen komplexen Zusammenhang zwischen Korrosion und Scaling auf Baustahlcoupons. Die Auslagerungszeit, sowie die Temperatur spielen eine entscheidende Rolle. Zunächst ist eine Abnahme der Korrosionsrate über die Zeit zu beobachten, die die Bildung einer zunehmend dichten und anhaftenden Sideritschicht dokumentiert. Die höchste Korrosionsrate ist in den 80 °C Versuchen zu beobachten. Ein lokales Korrosionsratenmaximum unter 100 °C wird daher vermutet.

Der neu gebildete Siderit hat eine raue Oberfläche und bildet das Substrat für Scaling aus dem Geothermalwasser, überwiegend Ba/Sr-Sulfat und Pb-Sulfide. Diese Schwefelablagerungen sind häufig giftig und teilweise radioaktiv, weshalb angemessene Maßnahmen bezüglich deren Handhabung und Entsorgung ausgearbeitet werden müssen.

Die getesteten Legierungen korrodieren in einem deutlich geringeren Ausmaß. Wenn keine Lochkorrosion zu beobachten ist liegen die Korrosionsraten unter 0,005 mm/Jahr. Bei 80 °C zeigen Coupons von **430F** und **316L** Lochkorrosion auf offenen Flächen, bevorzugt entlang chemischer Heterogenitäten (z.B. Mangansulfidausscheidungen), die bevorzugten Angriffspunkte darstellen. Das Korrosionsverhalten der Legierung wurde auch mit Hilfe elektrochemischer Methoden messtechnisch erfasst. Die Beobachtungen aus den Auslagerungsversuchen konnten hierbei weitgehend bestätigt werden. Eine spontane Passivierung drückt sich durch einen signifikanten Anstieg des freien Korrosionspotentials *OCP* aus, die für alle Legierungen beobachtet werden konnte. Jedoch zeigen die am niedrigsten legierten Werkstoffe ab dem Überschreiten eines gewissen Potentials eine unbeständige Entwicklung (Fluktuationen, spontane Abfälle) des *OCPs*, welches metastabile oder sogar stabile Lochkorrosion anzeigt. Die Lage des *OCPs* bewegt sich hierbei im Bereich des

Repassivierungspotentials  $E_R$ . Die höher legierten Edelstähle **904L** und **318LN** zeigen keine Lochkorrosion in den 80 °C Auslagerungsversuchen, jedoch deuten die elektrochemischen Messungen an, dass auch diese Werkstoffe lochkorrosionsgefährdet sind. Um signifikanter Korrosion vorzubeugen, sollten CrNiMo Werkstoffe mit einer  $PREN > 35$  oder Nichteisenmetalle wie z.B. Titan gewählt werden, die in der Testumgebung spontan passivieren.





# Contents

<b>Abstract</b>	<b><i>i</i></b>
<b>Zusammenfassung</b>	<b><i>iii</i></b>
<b>Contents</b>	<b><i>vii</i></b>
<b>1 Introduction</b>	<b>1</b>
1.1 Geothermal energy	1
1.2 Engineering challenges for geothermal development	3
<b>2 Thesis structure</b>	<b>7</b>
<b>3 The Upper Rhine graben (URG) geothermal resource</b>	<b>11</b>
3.1 Geology and geothermal characteristics of the URG	12
3.2 Hydrochemistry of URG geothermal waters	12
3.3 Geothermal site description: Soultz-sous-Forêts and Bruchsal	15
3.3.1 Soultz-sous-Forêts	16
3.3.2 Bruchsal	17
<b>4 Corrosion of metals</b>	<b>19</b>
4.1 Corrosion in the geothermal context	22
4.1.1 Role of CO <sub>2</sub>	24
4.1.2 Role of chloride	25
<b>5 Scaling</b>	<b>27</b>
<b>6 Applied methods and experimental</b>	<b>31</b>
6.1 Weight loss method and exposure instrumentation	31
6.1.1 On-site corrosion bypass Soultz-sous-Forêts, France	32
6.1.2 Laboratory autoclave	33
6.2 Electrochemical experiments	34
6.2.1 Setup	34
6.2.2 Methods and electrochemical basics	34
6.3 Test metals	38
6.4 Test solutions	40
6.5 Analysis of post-exposure coupons	41
6.6 $E_h$ -pH diagrams	41
<b>7 Laboratory and on-site studies on metal corrosion</b>	<b>43</b>
7.1 Objectives	43
7.2 Methodology and experimental	43
7.3 Results and discussion	44
7.3.1 Mild steels	44
7.3.2 Stainless steels	46
7.3.3 Ni-based alloy	49
7.3.4 Method comparison	49
7.4 Concluding remarks	51

<b>8 Corrosion and scaling in an operating geothermal power plant</b>	<b>53</b>
8.1 Objectives	53
8.2 Methodology and experimental	53
8.3 <i>In situ</i> brine monitoring during operation	54
8.4 Results and discussion	59
8.4.1 Mild steels	59
8.4.2 Corrosion and scaling observations on alloyed and non-ferrous metals	63
8.5 Concluding remarks	68
<b>9 Electrochemical study on corrosion of different alloys</b>	<b>71</b>
9.1 Objectives	71
9.2 Methodology and experimental	71
9.3 Results and discussion	72
9.3.1 Passivation observations	72
9.3.2 Stability evaluation and corrosion observations	77
9.4 Concluding remarks	83
<b>10 Conclusions</b>	<b>85</b>
10.1 Outlook and perspective	88
<b>References</b>	<b>91</b>
<b>Declaration of authorship</b>	<b>99</b>
<b>Acknowledgements</b>	<b>101</b>
<b>Curriculum Vitae</b>	<b>103</b>

# 1 Introduction

Renewable energy sources have a large potential to displace emissions of greenhouse gases from the combustion of fossil fuels and thereby to mitigate climate change. Renewables can contribute to social and economic development, to energy access, to a secure and sustainable energy supply, and to a reduction of negative impacts of energy provision on the environment and human health (IPCC, 2012). In fact, renewable energies are gaining more and more importance. In Germany, the current share of electricity from renewable energies to the total production is 20%. In the year 2050 about 80% of the power supply is aimed to be covered by renewable energies (BMWi, 2012).

Today, wind, solar, and biomass are the main producers of renewable energy. However, the power supply from wind and solar varies with weather and daytime and for base load power provision they require storage solutions. Fuel produced from biomass can be stored but expanding bioenergy production will require sophisticated land and water use management (IPCC, 2012). The use of geothermal resources, which can be found anywhere, is a promising option, as the accessible underground hosts gigantic amounts of energy (Bertani, 2009). Geothermal energy has undeniable advantages when compared to other renewable energies. The simultaneous provision of base load power and heat with low environmental impact is one of the superior characteristics. In addition, a variable operation mode allows covering of the seasonal and daily demand. It is especially suitable for supplying base-load power, but also can be dispatched and used to meet peak demand. Hence, geothermal electric power can complement variable electricity generation. However, one obstacle towards a more dynamic development of geothermal utilization is that high investments for drilling arise at the beginning of each project. These costs are coupled with a relatively high uncertainty for success (Huenges, 2010).

## 1.1 Geothermal energy

Geothermal resources consist of thermal energy from the Earth's interior stored in both rock and trapped steam or liquid water. The main sources of this energy are the crustal rocks. They contain radioactive isotopes, in particular uranium (U-235, U-238), thorium (Th-232), and potassium (K-40) which decay continuously and release heat that

reaches the surface (Birch, 1954). Geothermal resources as they are currently exploited occur in a number of geological settings where the temperatures and depths vary accordingly. High-enthalpy resources ( $>180\text{ }^{\circ}\text{C}$ ) are usually associated with recent volcanic activity and are found near tectonic plate boundaries or at crustal and mantle hot spot anomalies. Low ( $<100\text{ }^{\circ}\text{C}$ ) to medium ( $100\text{-}180\text{ }^{\circ}\text{C}$ ) enthalpy resources are also found in continental settings with above-average radioactive heat production or where aquifers are charged by circulating waters along deeply penetrating faults. Geothermal energy is considered as a renewable resource as the tapped heat from an active reservoir is continuously restored by natural heat production, conduction and convection from surrounding hotter regions. The extracted geothermal water is replenished by natural recharge and by reinjection of the spent water.

First attempts to use earth's heat as a source of energy were made in the early 20<sup>th</sup> century, when electricity was produced for the first time from steam at Larderello, Italy (Burgassi and Cappetti, 2004). Today, more than 20 countries generate base load electricity from geothermal energy and about 60 countries make direct use of the heat. Globally, the total installed capacity is about 8000 MW<sub>e</sub>, with an estimated 67.2 TWh<sub>e</sub> yr<sup>-1</sup> of supply provided in 2008 at a global average capacity factor of 74.5% (IPCC, 2012). The capacity for direct use is more than 15000 MW<sub>t</sub>, generating 224 TWh<sub>t</sub> yr<sup>-1</sup> (Gupta and Roy, 2007; IPCC, 2012). Most of these sites produce energy from easily developed, economically competitive high enthalpy resources (e.g. USA, Philippines, Indonesia, NZ). But the deeper, stored thermal energy, which is present anywhere is gaining more and more attention (MIT, 2006). Thermal surface manifestation (e.g. hot springs, geysers) are usually absent in such systems, which requires a sophisticated resource assessment and exploration strategy. An important challenge would be to prove that enhanced geothermal systems (EGS) can be deployed economically, sustainably and widely.

The global average annual growth rate of installed geothermal capacity for power generation over the last five years (2005-2010) was 3.7%, and 7% over the last 40 years (1970-2010) (IPCC, 2012). In order to achieve a more dynamic market development in the future several technical (e.g. reservoir understanding, proper handling of the geothermal water, and well-engineered design of the geothermal cycle) and non-technical barriers (e.g. public acceptance, economic barriers, and institutional barriers) have to be addressed.

The same applies for the Upper Rhine graben (URG) geothermal resource which offers favorable conditions for geothermal utilization. Several projects emerged in the last decades producing water from greater depth to generate electricity in binary-type power plants (e.g. Soultz, Bruchsal, and Landau). However, the hydrochemical characteristics account for different issues and engineering challenges remain on the way to a viable use of this vast resource.

## 1.2 Engineering challenges for geothermal development

An important challenge for the successful utilization of geothermal energy is related to geochemical and process engineering issues. In order to tap the full potential of this vast resource and to take advantage of its superior characteristics a high availability of geothermal power plants and a reliable power provision have to be achieved. The availability of these technical installations mainly depends on the integrity of components (e.g. the pump, casing, and the heat exchanger) which are in contact with the geothermal water. Usually metallic construction materials are used for these components. A reasonable material selection, taking into account economic considerations can lower the operating costs of geothermal facilities (DeBerry *et al.*, 1978; Conrad *et al.*, 1983; Carter and Cramer, 1992). The aim of corrosion engineering must be to ensure continuous operation. The most critical components in the geothermal loop are the production pump and the heat exchanger and their malfunction results in extensive downtime periods with no power production (Frick, 2011). Both components are subjected to very harsh conditions not only because of electrochemical corrosion processes but also because of mechanical abrasion by suspended solids.

The great majority of existing geothermal power plants have therefore been constructed in accord with historical “rules of thumb”, often adapted from the hydrocarbon industry. Two fundamental design concepts exist: (1) using corrosion-resistant materials throughout the system or (2) using low-cost materials and accepting replacement in case of failure. However, high-quality materials are inevitable for some process components when conventional materials have failed or are expected to lack performance. This includes equipment that is required to have a high reliability and near-zero corrosion allowance for reasons of performance, maintenance, and safety (Thomas, 2003).

The conditions in geothermal operation are different to related industries and waters with their unique natural characteristics have to be handled at high temperatures and high flow rates. The processed geothermal waters are often referred to as “hot rock soup” as they contain high amounts of dissolved solids and gases (Miller, 1980). Some ubiquitous constituents are known for their corrosive properties and will challenge the materials. The combination of these factors sets up a very harsh environment, which challenges the performance of many engineering materials and leads to the corrosion and scaling. Consequences may be the failure of components, clogging of pipes with possibly toxic precipitates, and a decline in efficiency. The prediction of material behavior in geothermal environments is challenging owing to the complex system chemistry.

A profound understanding of the environment to which materials are exposed to is therefore inevitable to find improved strategies to avoid undesired processes such as corrosion and scaling. Throughout Germany, there are only few operating geothermal sites which support scientific investigations. The prime motivation for most operators is to maintain operational safety in their existing plants. However, in order to tap the full potential and to achieve a sustainable development of geothermal energy, corrosion and scaling have to become controllable by taking adequate measures.

A lot of site-specific corrosion and scaling research has been carried out on corrosion and scaling in the 70s and 80s, mainly in the US, but also in New Zealand (DeBerry *et al.*, 1978; Conover *et al.*, 1980; Lichti *et al.*, 1981; Conrad *et al.*, 1983). In the following decades a lot of research on the fundamentals of corrosion in saline environments has been carried out (*i.a.* MacDonald *et al.* 1979; Miller, 1980; Palacios and Shadley, 1991; Linter and Burstein, 1999), while the efforts on application oriented research lessened. In the last years an increased interest in studying corrosion and scaling in geothermal environments is apparent (*i.a.* Bäßler, 2009; Baticci, 2009; Pfennig and Bäßler, 2009, Pfennig and Kranzmann, 2012; Pfennig *et al.*, 2013; Zhu, 2011; Klapper, 2011, 2012; Karlsdottir, 2012; Scheiber, 2013). Most of today’s research is carried out from a material qualification viewpoint in simulated geothermal environments and by using synthetic geothermal brines or waters. Nevertheless, application oriented on-site studies, particularly in the central-European geothermal sites, are still rare and only few comparative conclusions can be drawn. For this reason, the performed research program has a unique character and combines on-site and lab experiments studies by using different methods and natural geothermal brines as “test” waters. This more integrated approach is intended to give us a better understanding of the whole dynamic of corrosion

and scaling. It is accepted in corrosion research, that best material test is conducted in the environment of the intended use where all influencing parameters contribute to the corrosion process. However, using electrochemical techniques with simplified setups is often more productive and may give valuable information about the thermodynamic behavior of various metals in simulated laboratory environments.





## 2 Thesis structure

This work is a cumulative dissertation and contains three individual studies (chapter 7, 8, and 9). The first two are published in ISI-reviewed journals and the last is close to submission. The studies are ordered chronologically and were performed independently by using well-established methods and techniques from corrosion research and analysis.

In close cooperation with Petra Huttenloch (European Institute for Energy Research Eifer) and with the technical help of other colleagues, *i.a.* Roman Zorn (Eifer), Hagen Steger (KIT), Julia Scheiber and Albert Genter (both GEIE Exploration Minière de la Chaleur), following work has been carried out:

- Setup of the laboratory instrumentation (autoclave and the three-electrode measurement cell) to perform corrosion experiments with geothermal brines.
- Regular sampling of water from Bruchsal and Soultz-sous-Forêts for the laboratory experiments and on-site measurements.
- Planning and realization of the laboratory experiments and data acquisition.
- On-site experiments at Soultz in close cooperation with GEIE and ThyssenKrupp VDM

The performed experiments were very productive and a lot of data could be generated. Different questions emerged during the research and were subsequently tackled. Hereby, it is obvious that new studies always incorporate experiences from preceding ones which leads to a methodological “train of thought”. The following points describe the evolution of the work:

- (1) The first publication (chapter 7) represents the foundation for the corrosion and scaling research. It comprises results from potentiodynamic polarization using Soultz brine and from *in situ* exposure tests in Soultz. One important question which has been tackled was to check the applicability and the reproducibility of electrochemical measurements. Furthermore, the effect of the chloride concentration on the pitting and repassivation behavior has been evaluated. The *in situ* experiments led to the formation of scaling on the exposure coupons. Thus, the impact of scaling on the corrosion process was firstly recognized and traced in the following research.
- (2) The second publication (chapter 8) was intended to tie in with the first publication. The *in situ* monitoring program was very helpful to define the

corrosion/scaling environment and to deliver key information for the laboratory experiments. One aim was to investigate the interrelation between corrosion and scaling and to establish a better understanding of the dynamic. The comparison between *in situ* and autoclave exposure experiments led to interesting insights into the corrosion intensity at different temperatures and exposure conditions. It could be discovered that mild steels corrode with a long-term corrosion rate of less than  $0.2 \text{ mm y}^{-1}$ . The material loss, however, is replaced by a Fe-carbonate (siderite) corrosion product, which lowers the corrosion intensity over time. Scaling and corrosion are inextricably linked in geothermal environments and we could demonstrate that different forms of scaling occur on corroding metal surfaces: either substrate-related corrosion scaling (e.g. Fe-carbonate) or brine-related scaling (e.g. Ba/Sr-sulfates and Pb-sulfides). The construction material acts in two ways: it may corrode itself accompanied by the formation of a corrosion scale, and it may act as a catalyst for scaling to precipitate.

- (3) The third publication (chapter 9) is a pure laboratory work and comprises the application of different electrochemical methods in order to evaluate the corrosion behavior of alloyed materials exposed to deaerated  $80 \text{ }^\circ\text{C}$  geothermal brine containing  $\text{CO}_2$ . After having touched the subject of electrochemical measurements in the first publication, we pursued this topic with more profound techniques. The question is: how do these metals react in such a corrosive environment and in which way do we measure ongoing corrosion processes? Potentiodynamic polarization and *OCP* measurements were extremely useful to study the behavior of a wide range of materials and provide insights into processes on the metal-electrolyte interface at elevated temperatures.  $E_h$ -*pH* diagrams have also been computed to corroborate or complement the experimental results. These can help to comprehend the breakdown of passivity and the onset of pitting. The combined use of different methods enables us to give a good prediction whether or not a given material is prone to suffer pitting corrosion. In contrast to the prior publications, this work was performed by using two different URG brines (Soultz and Bruchsal), with their own hydrochemical characteristics.

The given studies are embedded in a wider frame, which provides the current status of geothermal energy utilization among the other renewable energies and addresses engineering issues which have to be resolved on the way to a sustainable use. The Upper Rhine graben geothermal resource (URG) is described from a “geo”-perspective, which includes the geology, the hydrogeology, the geothermal characteristics, and the hydrochemistry of deep-seated waters. Two URG geothermal sites, Bruchsal (Germany) and Soultz-sous-Forêts (France), are of prime importance for this work and the main part of this work relies on these sites. These are focused with their individual geochemical and operational characteristics. Before the studies are summarized, basic principles and methods from corrosion chemistry and research are given in chapter 4. This carries over into the geothermal context, where the process environment is different from other industries and unique observations with regard to corrosion and scaling have to be expected (chapter 4.1 and 5). Information about the *in situ* and laboratory experiments and the available instrumentation which was used in this study are given in the experimental section (chapter 6). Chapter 10 summarizes and discusses the major achievements of the research and provides directions for future research.



### 3 The Upper Rhine graben (URG) geothermal resource

The Upper Rhine graben (URG) is one of the geological structures with an elevated heat flow where a utilization of a medium enthalpy resource is currently developing. At different stratigraphic levels the deeper underground hosts hot water resources, which can be used for electricity production and heating. Several projects (e.g. Soultz, Basel, Landau, and Insheim) emerged in the last decades, producing geothermal highly saline waters from different lithologies. The brines are usually produced with 120-160 °C, cooled to about 70-80 °C and reinjected into the same rock formation. Originally planned to provide electricity, current projects aim for a cogeneration of heat and power. For instance, the Landau project generates about 2.9 MW<sub>e</sub> on a typical year and provides heat to the district heating system (Baumgärtner, 2007).

This chapter provides an overview over the URG conditions described from a “geo”-perspective. Fig. 1 depicts the locations of the geothermal projects Soultz, Bruchsal, and Landau in the border area of Germany and France. A detailed description of Soultz-sous-Forêts (France) and Bruchsal (Germany), which were of special importance for this work, is given in chapter 3.3. The available infrastructure and the well-meaning cooperation with different partners and suppliers were very conducive to this work.

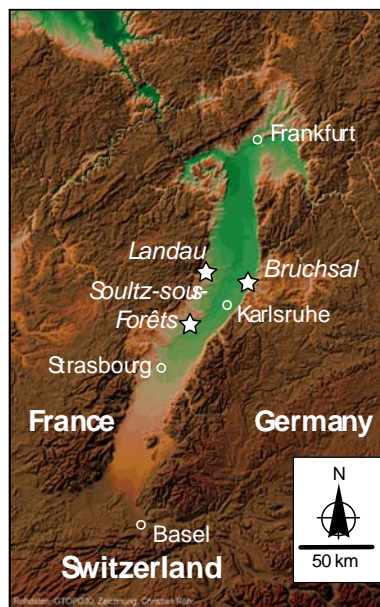


*Fig. 1 Location of the geothermal sites (asterisks) in the Upper Rhine graben in the German-French-Swiss border region (base map from [www.oberrheingraben.de](http://www.oberrheingraben.de)).*

### 3.1 Geology and geothermal characteristics of the URG

The URG is a major feature of the Cenozoic Rift system of Western and Central Europe. It extends over 300 km from Basel (Switzerland) to Frankfurt (Germany) with an average width of 40 km (Ziegler, 1992). The graben was formed by up-doming of the crust-mantle boundary due to magmatic intrusions in 80-100 km depth. It therefore offers favorable conditions for geothermal exploration with a high heat flow of 100-120 mW m<sup>-2</sup>, compared to 80 mW m<sup>-2</sup> in the surrounding area (Pribnow and Schellschmidt, 2000). Three major temperature anomalies could be identified: Landau, Soultz and Speyer, all confined to the graben borders, where the major graben faults are located. For example, Soultz is characterized by an exceptionally high near-surface gradient (approx. 110 °C), about three times higher than normal. Convection plays a major role in this geologic setting, lifting high-temperature brines close to the surface (Kohl *et al.*, 2000). All thermal anomalies lie near the western graben border. Two different processes have been identified to explain this asymmetry: (1) a general east-west flow pattern with ascending flow in high-permeability zones (Gerard *et al.*, 1984) and (2) the depth of the crystalline basement, as a radiogenic heat source, increases eastwards.

The deeper underground in the URG hosts hot water resources, which can be used for heating or even electricity production. Targets for geothermal exploration are the hydrothermal reservoirs of the Buntsandstein, the Upper Muschelkalk, and the lesser important Hauptrogenstein, which is confined to the southern part of the URG (Stober and Jodocy, 2011). Another important geothermal resource is the granitic crystalline basement of the URG, which offers high temperatures at practically-drillable depth. It is characterized by the occurrence of natural brine in the fractured crystalline rock. The permeability, however, is very low due to a poor hydraulic connection in the fracture network and “stimulation procedures” are necessary to achieve adequate productivity (Genter *et al.*, 2010).

### 3.2 Hydrochemistry of URG geothermal waters

The presence of deep-seated waters in the granitic basement and overlying sedimentary rock of the URG is well documented from numerous deep boreholes, mainly drilled for hydrocarbon exploration. A summary of hydrochemical data from the URG is given in Stober & Jodocy (2011). Several studies focus on hydrochemical

aspects of the brines (Pauwels *et al.*, 1993; Aquilina *et al.*, 1997; Stober and Jodocy, 2011). The dating of the brines is generally very difficult, but it can be expected that the residence time in the host rock is presumably in the range of  $10^5$ - $10^6$  years. The genesis can be traced by evaporation, mixing and water-rock-interaction processes. Fig. 2 gives a schematic overview of proposed processes which dictate the chemistry of the URG brines (Pauwels *et al.*, 1993; Aquilina *et al.*, 1997; Stober and Jodocy, 2011). However, there is still need to improve the knowledge of the chemical processes in order to better localize the source of the fluids. The URG brines do not satisfactorily fit into the established classification for high-enthalpy geothermal waters, which was presented in a fundamental work by Ellis and Mahon (1977). For this reason it is inevitable to have a closer look on the characteristics of these brines. With regard to a geothermal utilization the discovery of circulation patterns, flow paths and high-temperature zones within the strata is highly important. The history of the brine in contact with the surrounding host rock is the key to understand its tendency to form scalings. Under reservoir conditions it is close to thermodynamic equilibrium, which is very sensitive and easily disturbed due to a change in the p-T-conditions or of the pH. This, obviously, is inevitable in the geothermal cycle, which is the reason why geothermal waters must be regarded with respect to their scaling potential.

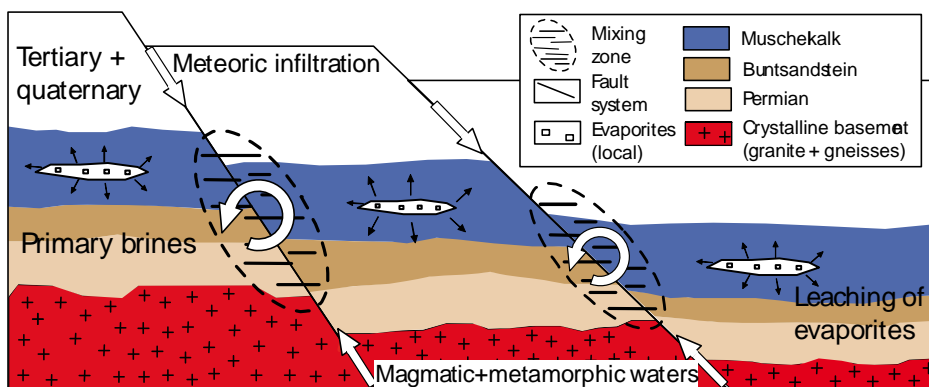


Fig. 2 Schematic of water evolution, circulation, and mixing in the URG strata near the graben boundary.

The URG geothermal brines are complex multi-component systems with numerous dissolved constituents and gases. For example, Soultz brine contains more than 20 dissolved species with concentration of more than 10 mg l<sup>-1</sup>. The chemistry is the result from long-term interaction with the surrounding host rock and therefore bears characteristic rock signatures. Most deep URG waters span a range of 50-200 g l<sup>-1</sup> TDS (total dissolved solids). It is evident that dilution with less mineralized surface water contributes to the overall chemistry. This is corroborated by the observation that the mineralization increases with increasing depth (Fig. 3a). However, the highest salt concentrations (>200 g l<sup>-1</sup>) can be found in the Hauptrogenstein and may be related to local evaporite occurrences (Stober and Jodocy, 2011).

Among the considered waters of the URG two groups can be distinguished (Fig. 3b). The dominating type is the Na-Cl water whereas Ca is present in variable amounts. The second type is less distinct and contains Na-Ca-SO<sub>4</sub>-HCO<sub>3</sub> mixture waters, with SO<sub>4</sub> as the main anion and a minor component of Cl. There is no clear correlation between lithology and water type. For instance, Na-Ca-SO<sub>4</sub>-HCO<sub>3</sub> waters occur in the Hauptrogenstein, in the Muschelkalk and in the Buntsandstein. At the same time Na-Cl dominated waters also occur in within the three lithologies. Mg is only a minor component in all waters.

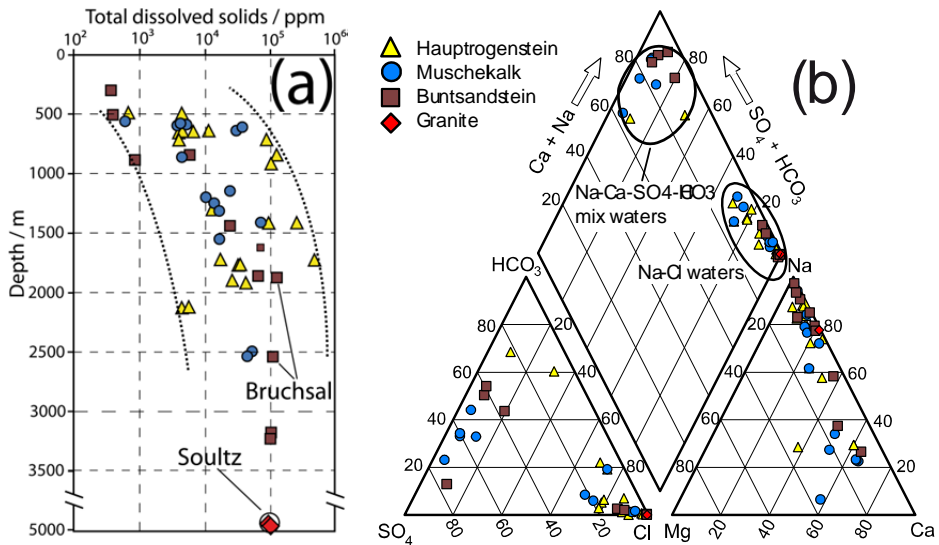


Fig. 3 (a) Total dissolved solids vs. depth diagram of deep wells of the URG; (b) Piper diagram of deep waters from the URG (data from Stober and Jodocy, 2011).



The deep waters from the URG often contain significant amounts of dissolved gases. Gas compositions from several sampling campaigns in Soultz are reported in Sanjuan *et al.* (2010). For instance, the gas liquid ratio (GLR) of the GPK2 brine can reach 40 vol%, at other sites even considerably higher. The gas composition is strongly dominated by CO<sub>2</sub> with minor fractions of N<sub>2</sub>, CH<sub>4</sub>, H<sub>2</sub>, and He. The presence of CO<sub>2</sub> increases the acidity and most waters have a pH of 5 to 7. The gas phase is most likely associated with the occurrence of hydrocarbons in the surrounding area of Soultz (e.g. Pechelbronn oil field).

For the Soultz brine, Sanjuan *et al.* (2010) demonstrated that the deep native brine is close to equilibrium with respect to a sedimentary mineral assemblage, containing quartz, albite, K-feldspar, calcite, dolomite, gypsum, at 230 - 240 °C. The use of geothermometers is widely accepted for geothermal waters (Fournier, 1977). Chemical and isotopic characteristics indicate a common origin, regardless whether sampled in the granite or in the overlying sedimentary cover. Interstratigraphic circulation would be possible along deep reaching fractures (Pauwels *et al.*, 1993). The chemical signature of the fluid suggests a sedimentary host rock (Buntsandstein) rather than a granitic. Chemical equilibration most probably took place close to the graben center, where the Triassic reservoir rock reaches temperatures up to 230 °C (Sanjuan *et al.*, 2010). Geothermometry calculations indicate that the some fluids reached temperatures up to 260 °C before upflow to shallower depths. Especially, the Na/K and Na/Li geothermometer preserve the best memory for the equilibrium temperature reached earlier.

### **3.3 Geothermal site description: Soultz-sous-Forêts and Bruchsal**

This work focuses on two of the URG geothermal sites: Bruchsal (Germany) and Soultz (France). With the kind permission of the operators (EnBW AG and GEIE) we could sample water for laboratory experiments, perform *in situ* exposure tests and carry out on-site measurements. Like in most URG geothermal projects, the produced waters are used for power generation in binary-type cycles (ORC or Kalina). In these systems a second medium is used to produce steam and to drive the turbine before it is condensed via a cooling tower. The spent geothermal water is then reinjected in one (Bruchsal) or more (Soultz) reinjection wells. In the following the two sites are described in more detail.

### 3.3.1 Soultz-sous-Forêts

The Soultz geothermal project history goes back more than 25 years when a French-German team started first investigations (Genter *et al.*, 2010). The original European Hot Dry Rock (HDR) project at Soultz-sous-Forêts was renamed as an Enhanced Geothermal System (EGS) project in 2001 after discovering that the fractured granitic basement contained large volumes of hot brine (Genter *et al.*, 2010). The aim was to develop, test and model two geothermal reservoirs at 3.5 and 5 km depth. The 5 boreholes GPK1-4 and EPS1 penetrate the Paleozoic granitic basement in a depth of about 1400 m. The basement mainly consists of a porphyritic granite with some local paleoweathering zones in the upper section. At greater depth it is intensively faulted and bears significant amounts of amphibole and biotite. The lower sections of GPK2 and 3 are in the two-mica granite, which is interpreted as a post-magmatic intrusion (Hooijkaas *et al.*, 2006). The natural transmissivity of flow paths is very low and various stimulation techniques have been applied and tested at the Soultz site. For instance, the initial injectivity/productivity index of GPK-2 was low, but was increased by a factor of 20 by the stimulation procedures.

Today, after more than 20 years of scientific investigation, the geothermal site of Soultz has reached the long-term operation stage and represents a unique opportunity to carry out scientific and technical monitoring programs at one of the first EGS installations. Over the last years different well configurations have been tested. At the moment GPK2 is the producing well and GPK3 and GPK4 the reinjection wells. In 2007, a 1.5 MW<sub>e</sub> power plant was built. The produced brine has a temperature of about 165 °C and is used to evaporate isobutane in the binary ORC cycle (Genter *et al.*, 2010). A schematic ORC cycle of the Soultz-type is given in Fig. 4.

The produced brine is characterized by a TDS of approx. 100 g/l, with Na<sup>+</sup>, Ca<sup>2+</sup>, and Cl<sup>-</sup> being the main ions. The *in situ* pH is < 5. An extensive sampling campaign has been carried out by Sanjuan *et al.* (2010). The sampling point is located near the wellhead of GPK3. Preliminary research on corrosion and material testing in the Soultz geothermal cycle has been carried out by Baticci *et al.* (2009, 2010). Recently, corrosion and scaling research as well as material testing is conducted by Julia Scheiber from GEIE (Scheiber *et al.*, 2013).

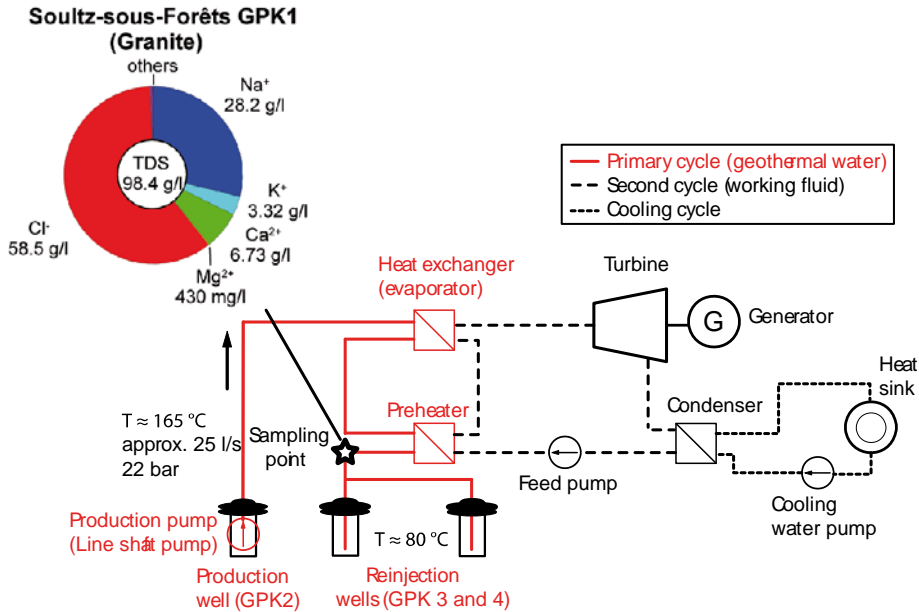


Fig. 4 Simplified schematic of an ORC binary power system (Soulz-type) (modified after Huenges (2010), DiPippo (2012); water analysis from Pauwels et al. (1993); the red color marks the stream sections and components where the produced and spent geothermal brine is in contact with construction materials.

### 3.3.2 Bruchsal

The Bruchsal geothermal project was initiated in 1983 when the GB1 was drilled to a depth of 1932 m. Later on the borehole had to be backfilled to 1877 m due to gas ingress. Highly saline brine was encountered at depth, which made a disposal into a surface water body impossible. GB2 with a depth of  $\approx 2500$  m was therefore drilled to reinject the water into the same rock formation. Today, Bruchsal is a classical hydrothermal “doublet” project run by the EnBW AG. Both boreholes penetrate the deep-seated aquifer of the Buntsandstein in an intensively fractured and sheared zone near the main graben boundary fault. The horizontal distance between the two wellheads is approx. 1400 m (Herzberger, 2008).

The aquifer hosts brine with a temperature of about  $125^\circ\text{C}$  and a TDS of approx. 123 g/l. The main ions are Na, Ca, and Cl and the pH is  $<5$ . Interestingly, the salinity in the two wells is very similar, although GB2 is 600 m deeper. At the same time the geothermal gradient is higher in GB1, which indicates an upflow zone.

The downhole pump produces brine with a rate of about 24 l/s which is used in the Kalina process to produce electricity (about 550 kW<sub>e</sub>). The working fluid is a water-ammonia mixture. Fig. 5 gives a schematic of the Kalina binary power system used in Bruchsal. A sampling point is located near the wellhead of the production well GB2.

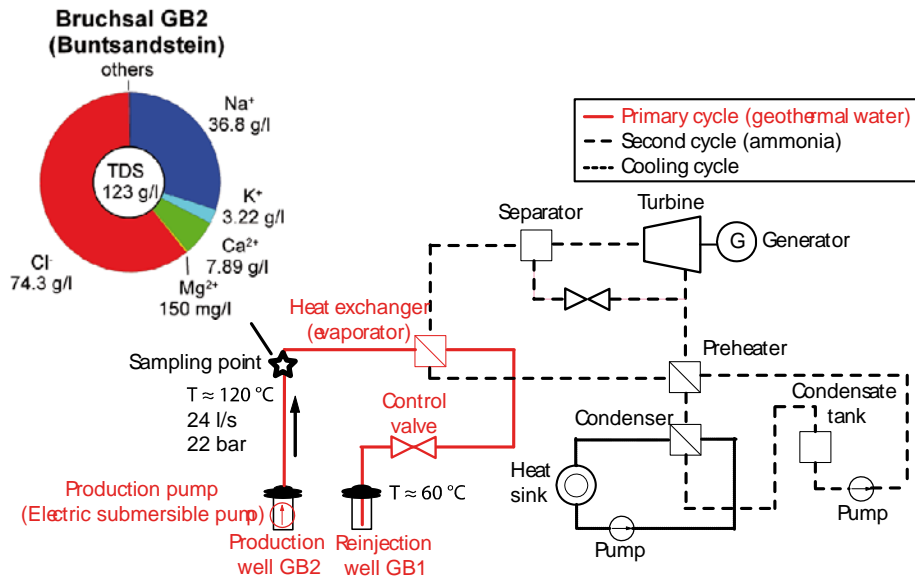


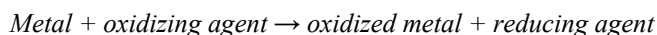
Fig. 5 Simplified schematic of a Kalina binary power system (Bruchsal-type) (modified after Mergner et al., 2012, water analysis from Pauwels et al., 1993); the red color marks the stream sections and components where the produced and spent geothermal brine is in contact with construction materials.

## 4 Corrosion of metals

Components in many engineering systems are made of metal, because they differ from other materials by a number of favorable properties, e.g. ductility, high tensile strength, temperature resistance, electrical and thermal conductivity, and ease of joining and machining. Common engineering metals are iron, chromium, nickel, copper, aluminum, titanium, and zinc or alloys which contain combinations of these constituents. However, most metals are thermodynamically not stable in contact with the atmosphere and will spontaneously react with the surrounding medium (Landolt, 2007).

Corrosion is the degradation of a material or of its functional properties through an electrochemical reaction with the environment. Materials can also be damaged by abrasion, which results from rubbing of solid surfaces. Only in some cases (e.g. improved corrosion resistance by oxidation, decorative aspects) corrosion is a welcome phenomenon. “Corrosion is an irreversible interfacial reaction of a material with its environment, resulting in the loss of material or in the dissolving of one of the constituents of the environment into the material” (Landolt, 2007). This definition is therefore a more generalized form and includes the positive and negative aspects of corrosion. The term corrosion is not only used for metals, but also for other materials (e.g. polymers, ceramics).

Corrosion of a metal occurs due to an irreversible redox reaction in the presence of an oxidizing agent. The electrochemical potential of the reduction reaction is thereby higher (more noble) than that of the oxidation reaction. A generalized form of a corrosion reaction is:



The overall redox reaction splits up into two partial reactions: the oxidation reaction with the liberation of electrons, referred to as the anodic partial reaction; and the reduction reaction with the consumption of the electrons, referred to as the cathodic partial reaction. Both partial reactions are inextricably linked by the principle of electroneutrality. In most aqueous systems two principal oxidizing agents are encountered: solvated protons and dissolved oxygen (Tab. 1). Taking iron as an example, the reaction with solvated protons results in the formation of ferrous iron and gaseous hydrogen (acid corrosion). In neutral and alkaline aqueous environments oxygen

will be the dominant reactant to form ferrous and the ferric iron, which then precipitates as low-soluble rust (oxygen corrosion).

*Tab. 1 Common types of corrosion reactions encountered in natural systems.*

Acid corrosion	Oxygen corrosion
$Fe \rightarrow Fe^{2+} + 2e^-$ (anodic)	$Fe \rightarrow Fe^{2+} + 2e^-$ (anodic)
$2H^+ + 2e^- \rightarrow H_2$ (cathodic)	$Fe^{2+} \rightarrow Fe^{3+} + e^-$ (anodic)
$Fe + H_{(aq)}^+ \rightarrow Fe_{(aq)}^{2+} + H_{2(g)}$ (overall)	$O_2 + 2H_2O + 4e^- \rightarrow 4OH^-$ (cathodic)
	$4Fe + 3O_2 + 2H_2O \rightarrow 4FeOOH$ (overall)

The given examples should demonstrate that the availability of certain species in the environment controls the corrosion process. Obviously, these are very simplified schemes of corrosion. In natural or engineering environments corrosion is controlled by several processes. Knowing the physico-chemical characteristics (e.g. pH, temperature, chemistry, redox state) but also hydrodynamic parameters of an environment is therefore highly important. Corrosion has to be considered as a system behavior, and depends on the material, the medium and the environment (Fig. 6). It cannot be adequately described by its single elements. Consequently, corrosion resistance is a system property and not a material property.

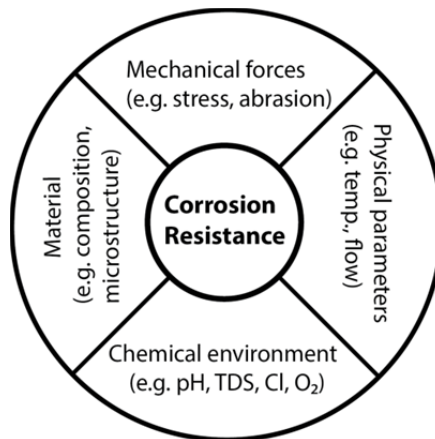


*Fig. 6 Corrosion system with factors of influence; modified after Landolt (2007).*

In which form corrosion occurs mainly depends on the considered metal/alloy and the chemistry of the surrounding medium. Uniform corrosion is characterized by a surface recession over the whole surface and can be expressed by a rate of corrosion (e.g. surface recession per unit of time). The service life of a component can be determined by the material thickness. For example, mild steels in low-pH chloride solutions will most likely suffer uniform corrosion, as iron as the main constituent does not form a passivating oxide (Pourbaix, 1973).

In a given environment, alloyed materials usually show lower uniform corrosion rates than mild steels but are prone to suffer localized corrosion (e.g. pitting and crevice corrosion). High dissolution rates occur locally while the remainder of the surface is passive. If the attack initiates on an open surface, it is called pitting corrosion; at an occluded site, it is called crevice corrosion. Both forms of localized corrosion are autocatalytic in nature and can lead to accelerated failure of components by perforation of the material (Frankel, 2003). Localized corrosion is strongly promoted by the presence of aggressive anionic species. For example, chloride has a high diffusivity and strongly interferes with the passive film to initiate pitting. In sulphate solutions no clear tendency to undergo pitting corrosion could be discerned (Leckie and Uhlig, 1966; Linter and Burstein, 1999). In some cases sulfate ions may also have an inhibiting effect in the presence of chloride. This example shows that dissolved constituents can have different effects, both individually and through their interaction.

In many environments alloyed materials are passive and therefore show a high resistance against corrosion. Passivity can be described as the phenomenon that “a metal substantially resists corrosion in a given environment despite a marked thermodynamic tendency to react”, e.g. high corrosion resistivity at relatively high electrochemical potentials (Han *et al.*, 2011). This behavior is related to the formation of thin oxide films (1-3 nm thick) which greatly reduce the rate of corrosion (Olsson and Landolt, 2003). Thus, the integrity and characteristics of the passivating oxide film, and the corrosion resistance of an alloy, strongly depends on the content of alloying elements, such as chromium, nickel, and molybdenum. While nickel is less readily oxidized, chromium and molybdenum are easily incorporated in the passive film (Lu *et al.*, 1993; Ilevbare and Burstein, 2001). Especially, molybdenum shows a complex oxide chemistry with different state of oxidation. A static passive film does not exist. Depending on environmental parameters such as potential, the presence of halides in the electrolyte, pH, and temperature, film growth and dissolution, adsorption, and ion incorporation takes place (Olsson and Landolt, 2003).

An adverse property of the passive film is the susceptibility to localized attack, particularly in the presence of aggressive anionic species, such as chloride ions (Leckie and Uhlig, 1966; Linter and Burstein, 1999; Frankel, 2003). Previous electrochemical studies of pitting corrosion suggest that characteristic electrochemical potentials exist, which can be used to assess the susceptibility to pitting corrosion (Leckie and Uhlig, 1966; Frankel, 2003). The effect of the electrochemical potential on the corrosion behavior, which includes passivity and pitting, can best be understood with the schematic polarization curve which explains the meaning of these potentials (Fig. 10). Their determination, however, is closely related to the potentiodynamic polarization technique and will be discussed in chapter 6.2.2.

## 4.1 Corrosion in the geothermal context

Controlling corrosion in geothermal operation is regarded as a major challenge and many material testing campaigns, mostly in the US, have been carried out in the early days of geothermal development. The aim was to understand the degradation process and to identify suitable materials. However, most of this work has been carried out in volcanic high-enthalpy systems and there is a general difficulty in transferring these experiences to other evolving geothermal sites worldwide.

On the way through the production – reinjection cycle the geothermal water is in contact with metallic components. The red color in Fig. 4 and Fig. 5 marks the stream sections and components where the produced and spent geothermal brine is in contact with construction materials and where the main corrosion is expected. Besides the casing/tubing in the production and reinjection well, other components, such as pipelines, separators, valves, heat exchangers and the production pump are exposed to fast-flowing and hot geothermal water. Sure enough, the construction material will somehow react with the surrounding medium. For many materials and components the question is not if it corrodes, but how fast it corrodes and what are the operational consequences in the case of corrosion.

Natural geothermal waters are different from corrosive media (e.g. chemicals, cooling waters), which are processed in other industries. They are complex multi-component systems with often high contents of dissolved solids and are also characterized by their chemical variability. Not only are there differences in the water



chemistry and temperature from one site to another but there may also be variations from one well to another within one site. Several factors make a geothermal corrosion environment special. These include the hydrochemistry, high flow rates, high temperature, and the presence of solid particles in suspension. These factors set up a corrosion environment, which challenges the many construction materials and limits the applicability of many metals.

The corrosivity generally arises from the combination of elevated temperatures and the presence of corrosive key species in the processed brine (MacDonald *et al.*, 1979). Of the many constituents in geothermal brines, seven key species were identified that account for most corrosion phenomena: oxygen, hydrogen sulfide, carbon dioxide, ammonia, chloride, sulphate, and hydrogen ions (pH) (DeBerry *et al.*, 1978; Conover *et al.*, 1980; Czernichowski-Lauriol and Fouillac, 1991). The presence of some constituents, mainly chloride and carbon dioxide, is very common in geothermal waters worldwide. Others are ubiquitous (e.g. sulphate, ammonia), but mostly at minor concentrations. Some constituents, such as oxygen and hydrogen sulfide, facilitate corrosion even in very low concentrations of a few ppm. However, corrosion in geothermal environments usually occurs in the absence of oxygen (Czernichowski-Lauriol and Fouillac, 1991). The presence of hydrogen sulfide is associated with volcanic activity and/or microbial activity (e.g. sulphate reducing bacteria SRB). However, it should be noted that not only hydrochemical characteristics, but also other factors (e.g. flow conditions, temperature, and stress) contribute to the harshness of an environment (DeBerry *et al.*, 1978).

In the URG the many produced geothermal waters have to be referred to as brines, which means that they contain a certain amount of dissolved solids and gases. Some of these constituents, e.g. chloride are ubiquitous in many brines and chloride-induced pitting is therefore a very likely corrosion mechanism. Carbon dioxide and its speciation products are mild oxidizing agents, but primarily affect the pH by the formation of carbonic acid. This corrosion mechanism has been described earlier as acid corrosion. Corrosion in the presence of carbon dioxide is often referred to as 'sweet corrosion' and is often observed in the hydrocarbon industry. The hydrogen ion released by the speciation of carbonic acid is probably the dominating oxidizing agent in the corrosion system. Dissolved oxygen, as a powerful oxidizing agent, is virtually absent in the pristine brine and is an indicator for atmospheric contamination. In Soultz, microbial activity of sulphate-reducing bacteria (SRB) was identified. Most probably, they are the source of  $S^{2-}$  ions in the brine. This clearly leads to a local change in the  $E_h$ -pH

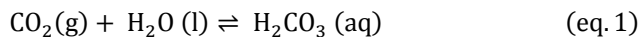
environments and corrosivity is increased (Scheiber *et al.*, 2012). However, the share of microbial induced corrosion (MIC) in overall corrosivity has not yet been determined and remains to be studied.

To sum up, different constituents account for the corrosivity of the URG brines. Generally, the presence of oxidizing agents in a chloride-containing environment is extremely detrimental and will further enhance corrosion. From a corrosion point of view, CO<sub>2</sub>-corrosion in combination with chloride-induced corrosion is the dominant mechanism in URG geothermal environments. To give an example, Pfennig and Bäßler (2009) showed that substantial corrosion occurred on 13% Cr alloys in 60 °C CO<sub>2</sub>-saturated synthetic brine.

#### 4.1.1 Role of CO<sub>2</sub>

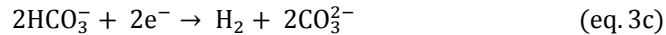
Corrosion in the presence of CO<sub>2</sub> has gained much attention by industry, since CO<sub>2</sub> is a common by-product in hydrocarbon and geothermal exploration (Linter and Burstein, 1999; Lopez *et al.*, 2003; Zhao *et al.*, 2009). Several authors suggest that the mechanisms of CO<sub>2</sub> corrosion change considerably near 60 °C and that the temperature range from 60 to 100 °C is a transition region for CO<sub>2</sub> corrosion (Schmitt and Rothman, 1978; DeWarrd and Lozt, 1993; Zhu *et al.*, 2011). Given this information, it becomes obvious that CO<sub>2</sub> corrosion dynamics has to be considered in the geothermal framework.

Carbon dioxide is a mild oxidizing agent that causes increased corrosion. However, it primarily affects the pH (Miller, 1980). According to Eq. (1), carbon dioxide dissolves in aqueous solutions to form carbonic acid.



Several mechanisms have been proposed for the dissolution of metals in oxygen-free CO<sub>2</sub> solutions. The main corrosion process can be summarized by one anodic (Eq. (2)) and three cathodic (Eqs. (3a–c)) reactions (Heuer and Stubbins, 1999; Lopez *et al.*, 2003).





#### 4.1.2 Role of chloride

Geothermal waters worldwide have a wide range of salinities, with chloride often being the main anion. While some geothermal waters have almost drinking water quality, the geothermal brines from Salton Sea (California) are an extreme example with chloride concentrations up to 200,000 ppm (Hoffmann, 1975). Chloride-induced corrosion therefore often is a big concern of operators.

The effect of chloride on the corrosion behavior of many metals and alloys has been widely discussed (Leckie and Uhlig, 1966; Sedriks, 1979; Gräfen and Kuron, 1996; Frankel, 2003; Anderko *et al.*, 2004; Burstein, 2004). It is known for destabilizing oxide films on passivating metals and for promoting localized corrosion, such as pitting. In general, pitting and passivity are inextricably interlinked. Pitting is initiated at electrochemical potentials higher than those at which passivation starts and therefore is a transpassive process (Burstein, 2004). Chloride causes local breakdown of passive films which protect passivating metals from uniform attack and leads to the more severe localized corrosion (Gräfen and Kuron, 1996; Burstein, 2004). Pit formation is induced by forming metal chlorides on the metal/film interface, which causes expansive stress leading to the rupture of the oxide film in the form of a nanoscopic explosion (Burstein, 2004). The effect of different chloride concentrations on pitting corrosion has been studied by other authors (Gräfen and Kuron, 1996; Anderko *et al.*, 2004).



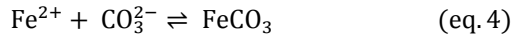
## 5 Scaling

Scaling in geothermal cycles is another concern for operators and occurs in many varieties worldwide. Scaling is a process which describes the precipitation of solids due to oversaturation and/or redox reactions in the processed geothermal water (Miller, 1980). The need to control scaling is due to three major difficulties: (1) the clogging of wells and pipes, (2) the decrease in the efficiency of pumps, heat exchangers, and turbines, and (3) the freezing of valves, which renders these components inoperative (Phillips *et al.*, 1980). However, scaling and geothermal waters may also be beneficial, as they can be regarded as important sources of a variety of elements, such as lithium and zinc (Gallup, 1998).

Precipitation preferably takes place on solid surfaces, such as pipe wall, where the precipitation reaction is catalyzed. Scaling occurs as a consequence of pressure drop, temperature changes, oxygen ingression, and/or corrosion, which are mostly inevitable effects during water processing. Scaling may result in the clogging of pipes, a loss in heat transfer efficiency and freezing of valves. Another concern is the potential toxicity of scaling and filter residues. All these processes require time-consuming cleaning and disposal procedures. Obviously, the type of scaling occurring in the geothermal cycle is coherent with the composition of the geothermal water. Common types worldwide are silica, carbonates, and sulfur minerals, each having individual characteristics in terms of formation and consequences. For example, heat extraction in many high-temperature sites is restricted by silica scaling as the water cools down.

The formation of a corrosion product is another form of scaling and is referred to as corrosion scale. It is associated to the degradation of the construction materials, which releases metal ions into the solution to form solids by the reaction with compounds in the flowing brine (Miller, 1980; Palacios and Shadley, 1991).

In CO<sub>2</sub>-bearing environments, material–brine interaction may also have beneficial effects, as newly formed corrosion scales may be capable to inhibit corrosion. The formation of siderite (FeCO<sub>3</sub>) according to Eq. (4) has often been observed in geothermal pipes and oil industry (Heuer and Stubbins, 1999), whereas the ferrous ion is principally released by the anodic partial reaction (Eq. (2)). Siderite is only slightly soluble in water. According to Benezeth *et al.* (2009) the solubility product log<sub>10</sub>K<sub>sp</sub> for the reaction



is 10.5 ±0.5 at 25 °C with decreasing solubility as temperature increases. The *E<sub>h</sub>-pH* diagram in Fig. 7 was derived by using the Outokumpu software “HSC chemistry 5.1” with the integrated thermodynamic and thermochemical database (Roine, 2006). It gives the thermodynamic stability fields of iron species in the Fe–C–Na–Cl–H<sub>2</sub>O system at 80 °C, which simulates the CO<sub>2</sub>-bearing geothermal brine from Soultz-sous-Forêts after the heat exchange. While the carbon in this simulation is considered to originate from the high CO<sub>2</sub> partial pressure, leading to carbonic speciation (Eq. (1)), the iron is considered to come from two sources: it is present as ferrous iron in the native geothermal brine and it is released due to corrosion of iron-based material (Eq. (2)).

Fig. 7 shows that in acidic and reducing environments, siderite is a more stable entity than any of the Fe oxides. This is true for the temperature range up to 200 °C prevailing at most geothermal sites. As a consequence of the low solubility product, once-deposited siderite will not dissolve easily, at least at pH values higher than 4. Siderite layers were often found to provide a good barrier against corrosion, conferring a state of passivation (Heuer and Stubbins, 1999; Han, 2009; Han *et al.*, 2009). The microstructure of the corrosion product is dependent on the temperature of formation affecting its protective effect of the underlying steel (Yin *et al.*, 2009). In case of damage, however, a galvanic cell between covered and uncovered regions can be established and the more severe localized corrosion is likely to occur (Han, 2009).

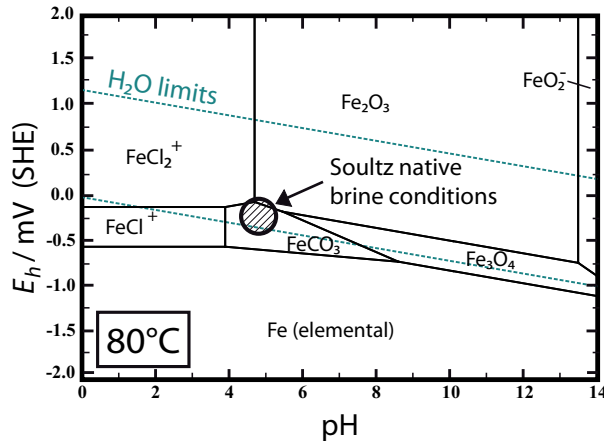


Fig. 7  $E_h$ -pH diagram for the Fe-C-Cl-Na-H<sub>2</sub>O system at 80 °C. Molalities  $M$  ( $\text{mol kg}^{-1}$ ) based upon Soultz brine chemistry: 0.05 M  $\text{Fe}^{x+}$ ; 0.15 M  $\text{CO}_2$ ; 1 M  $\text{Na}^+$ ; 1 M  $\text{Cl}^-$ ;  $E_h$  and pH conditions of the native Soultz geothermal brine are indicated by a hatched circle; the dotted lines indicate the thermodynamic stability field of H<sub>2</sub>O.

In Soultz, scaling is mostly related to the ORC (Organic Rankine Cycle) heat exchanger system and the reinjection side of the geothermal cycle. The heat exchanger cools the brine from 157 to approx. 70 °C. Here, sulfates/sulfides are most sensitive to precipitation and can therefore be found throughout the reinjection side (Scheiber *et al.*, 2012). Sulfur scales often incorporate radiogenic elements (e.g. radium). Scaling requires frequent and time-consuming cleaning procedures. As a preventive measure against scaling due to degassing, a pressure maintenance system is operating at Soultz to keep an operating pressure of approx. 20 bars in the surface installation (Genter *et al.*, 2010). A concept for an inhibitor system has been designed and is currently being set up (Scheiber *et al.*, 2012). So far, however, no process has been established to completely prevent scaling.

Carbonate scales mainly form as a consequence of CO<sub>2</sub> degassing and the resultant shift to more alkaline pH values. Rapid oversaturation often leads to the formation of aragonite, rather than calcite. Due to the retrograde solubility of carbonates the temperature drop on the heat exchanger leads to a higher solubility on the reinjection side. Precipitation of carbonates after reinjection might be a concern which leads to clogging of the reservoir.





## 6 Applied methods and experimental

This chapter summarizes the applied methods, the used instrumentation and gives experimental information. Beside corrosion investigations also the formation of scaling was investigated. The parameters and procedures slightly change in the given studies and are given individually in chapter 7-9.

### 6.1 Weight loss method and exposure instrumentation

Exposure tests were performed in the *in situ* corrosion skid (Fig. 8A) and in the laboratory autoclave (Fig. 8B). The duration of exposure and the experimental conditions are mentioned in the individual chapters.

For the experiments each of the chambers was equipped with a minimum of two coupons, for investigating the scale build-up and for the determination of the corrosion rate. The samples were positioned at the bottom of the chamber.

After extraction, the mild steel samples were treated with inhibited HCl according to ASTM G 1-03 and weighed again. Assuming uniform corrosion recession, the corrosion rate  $\omega$  in  $\text{mm y}^{-1}$  can be obtained from the mass loss  $\Delta m$ , the unit area  $A$ , the exposure time  $t$ , and the density  $\rho$  as follows:

$$\omega = \frac{\Delta m}{At\rho} \quad (\text{eq. 5})$$

Weight loss measurements are often considered to be the “gold standard” of corrosion testing and are certainly the easiest (Frankel, 2003). Nonetheless, important issues have to be considered. Beside the fact that the mass can only be measured easily only to about 0.1 mg, experiments provide an average rate over time as well as over the exposed surface. Thus, the occurrence of localized corrosion phenomena cannot be adequately expressed. Corrosion rate of full-size components may also deviate from corrosion rate of a coupon of the same material.

### 6.1.1 On-site corrosion bypass Soultz-sous-Forêts, France

*In situ* exposure experiments were performed in a corrosion bypass in Soultz-sous-Forêts which was designed by GEIE (Fig. 8A). Previous work and further information are reported in Baticci *et al.* (2009, 2010). The pressure in this section of the geothermal loop is maintained at 20 bars in order to prevent scaling induced by degassing (Genter *et al.*, 2010). The skid is located downstream of the heat exchanger near the well head of the GPK 3 borehole. The skid consists of three chambers with a volumetric capacity of 100 cm<sup>3</sup> each. The chambers are made of brass MS58 with an inner polyether ether ketone (PEEK) coating. The relevant technical and experimental parameters are given in Tab. 2.

Tab. 2 Relevant technical and experimental parameters in the on-site bypass Soultz; \* measured parameters, \*\* Sanjuan (2010), \*\*\*Baticci (2009).

On-site bypass Soultz		
Temperature	≈ 60 – 80*	°C
Pressure	Max. 20	bar
CO <sub>2</sub> fraction in the incondensable gases	50 – 90**	%
pH	≈ 4.6 – 4.8	-
Flow rate	≈ 4***	m <sup>3</sup> h <sup>-1</sup>
Flow velocity	≈ 0.3	m s <sup>-1</sup>
Exposure time	1 - 5	months

### 6.1.2 Laboratory autoclave

A laboratory autoclave was used to conduct exposure tests under simulated geothermal conditions. The autoclave has a volumetric capacity of 1.5 dm<sup>3</sup> and contains a PTFE liner and a PTFE mounting system (Fig. 8B). All autoclave experiments were run with 1 liter of brine. A stirrer ensures homogeneous mixing in cell reaction cell.

Autoclave experiments have been performed with natural and synthetic brines. De-aeration was achieved by degassing with a vacuum pump for at least 1 hour. Afterwards, the brine is filled into the PTFE coated reaction cell. Before heating up to the target temperature and applying pressure the brine is purged with technical-grade CO<sub>2</sub>. The temperature inside the autoclave was monitored with Pt-100 thermocouple during the experiments.

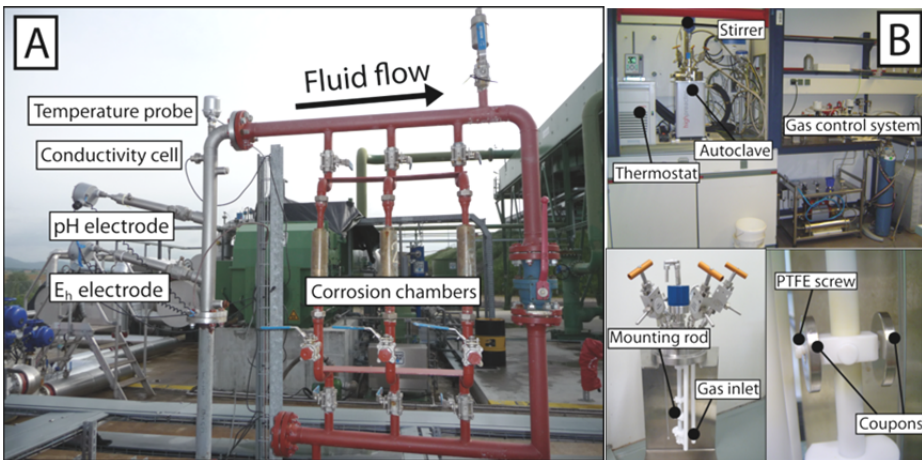


*Fig. 8 Instrumentation for monitoring and corrosion experiments; (A) ‘‘Geochemistry–Corrosion’’ skid designed by GEIE near the wellhead of GPK3 on the reinjection side of the Soultz geothermal cycle; left part: four probes used for continuous fluid monitoring (temperature, conductivity, pH, and  $E_h$ ); central part: chambers for corrosion research and material testing and (B) Laboratory autoclave system with the coupon mounting system.*

## 6.2 Electrochemical experiments

### 6.2.1 Setup

The polarization experiments were carried out in a double-walled glass cell (KMZ 5 AEH by Sensortechnik Meinsberg) which contains a three-electrode setup with test material as the working electrode (exposed surface:  $0.76 \text{ cm}^2$ ), a platinum counter electrode, and a KCl-saturated Ag/AgCl reference electrode. It has a volumetric capacity of 500 ml. A Haber-Luggin capillary was used to connect the working electrode with the reference electrode via a salt bridge. The spacing (4 mm) between the Haber-Luggin capillary was ensured by a Viton<sup>®</sup> spacer. One single surface ( $0.76 \text{ cm}^2$ ) of the test electrode is exposed to the electrolyte. It is encased in a mount with a Viton<sup>®</sup> surface seal. The potential was controlled by the LMremote software provided by Sensortechnik Meinsberg and the output was transferred to a computer. To ensure homogeneous mixing, a magnetic stirrer was used. For the 48 hours *OCF* measurements, a reflux condenser was used to prevent evaporation. Reference experiments with AISI 430 in 1N H<sub>2</sub>SO<sub>4</sub> were performed at regular intervals according to ASTM G5-82.

Electrochemical measurements have been performed with natural and synthetic brines. De-aeration was achieved by degassing with a vacuum pump for at least 1 hour. Afterwards, the brine is pressurized with CO<sub>2</sub> up to 6 bar (4.8 technical grade) for at least 30 minutes in order to achieve CO<sub>2</sub>-saturation. Then the brine is filled into the glass cell and heated up to 80 °C, before the pH is finally adjusted to 4.8 by addition of HCl. To stabilize the pH, CO<sub>2</sub> was added during the experiments.

### 6.2.2 Methods and electrochemical basics

Electrochemical polarization techniques have been used in this study. These were developed some 50 years ago and are widely applied in corrosion research (Pound *et al.*, 1985). Corrosion processes in nature are spontaneous. In electrochemical polarization, these processes are induced by external DC voltage which causes anodic and cathodic reactions on the metal surface. In this way, processes can be accelerated by several orders of magnitude (France, 1969).

Potentiodynamic polarization is one of the established methods and can be used in various ways, depending on the aim of investigation. The experimental procedure of

potentiodynamic polarization is given in ASTM G5-82. The experimental parameters used for the measurements are given in Tab. 3.

Information about the kinetics of an electrode reaction can be obtained by measuring the current density as a function of the applied potential. Scanning over a potential range about  $\pm 200$ -250 mV from the open circuit potential (*OCP*) results in a current density potential curve, or potentiodynamic polarization curve. The current density is the sum of the anodic and cathodic partial current densities. Provided that other anodic and cathodic reactions are small in comparison, this curve can be analyzed for the corrosion rate. Typically presented in a semi-logarithmic plot, polarization curves provide corrosion rate by extrapolation of the linear cathodic and/or anodic regions to the *OCP* (Fig. 9; Frankel, 2008).

According to the Stern–Geary equation (Eq. 6; Stern and Geary, 1957), the corrosion current density  $j_{corr}$  can be calculated from the resulting *Tafel* parameters  $\beta_a$  and  $\beta_c$ :

$$j_{corr} = \frac{\beta_a \beta_c}{2.303 (\beta_a + \beta_c)} \cdot \frac{1}{R_p} = \frac{B}{R_p} \quad (\text{eq. 6})$$

where  $j_{corr}$  is the corrosion current density ( $\mu\text{A cm}^{-2}$ );  $\beta_a$ ,  $\beta_c$  are the anodic and cathodic *Tafel* slopes (mV decade<sup>-1</sup>);  $B$  is the constant (mV) and  $R_p$  is the polarization resistance ( $\Omega\text{cm}^2$ ). The corrosion rate  $\omega$  (mm y<sup>-1</sup>) defined as the mean rate of removal of metal while assuming uniform corrosion is calculated from the corrosion current

$$\omega = 0.00327 \frac{j_{corr} EW}{\rho} \quad (\text{eq. 7})$$

where 0.00327 is a constant (for mm y<sup>-1</sup>),  $EW$  is an equivalent weight (g equivalent<sup>-1</sup>) of the corroding species and  $\rho$  is the density of the corroding metal (g cm<sup>-3</sup>).

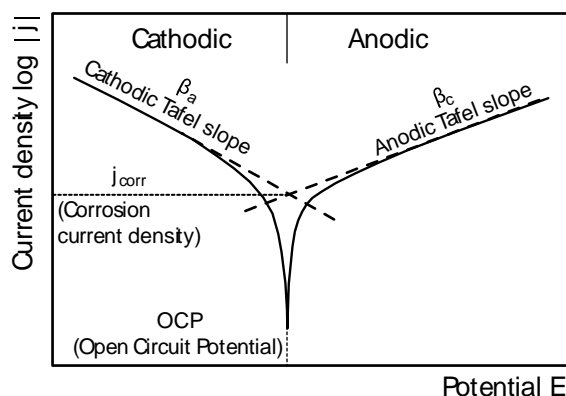


Fig. 9 Polarization curve exhibiting Tafel behavior. Dashed lines indicate the extrapolated fitting lines of anodic and cathodic branches (*Tafel* slopes).

Polarization over a wide range of potentials generates information about the thermodynamic behavior of the metal. Fig. 10 shows a schematic current density potential curve of a passive metal. This figure is a plot of the potential versus the logarithm of the current density. It can be separated in different thermodynamic domains which are delimited by the characteristic potentials. These are the open circuit potential  $OCP$ , the pitting potential  $E_P$  and the transpassive potential  $E_{TR}$ , as well as the repassivation potential  $E_R$ .

The open-circuit potential  $OCP$  develops spontaneously by an electrode without an external current (Landolt, 2007). Preliminary laboratory studies on passivity often overlook or ignore the evolution of the  $OCP$  (Burstein, 2010). It can take hours or even days to reach steady state conditions. In oxidizing environments it usually shifts towards higher values away from more active values, i.e. spontaneous passivation occurs. Generally speaking, the shift of the  $OCP$  of alloys towards higher values suggests an increase in passivity with low current densities (Wang *et al.*, 2009), while the risk for localized corrosion rises due to ennoblement (Blasco-Tamarit *et al.*, 2008). Generally speaking, towards higher potentials, the  $OCP$  ennoblement process is confined by the pitting potential  $E_P$  or rather the transpassive potential  $E_{TR}$  in case no pitting occurs (Wang *et al.*, 2009).

It was found that stable pitting did not occur at an arbitrary potential, but only above

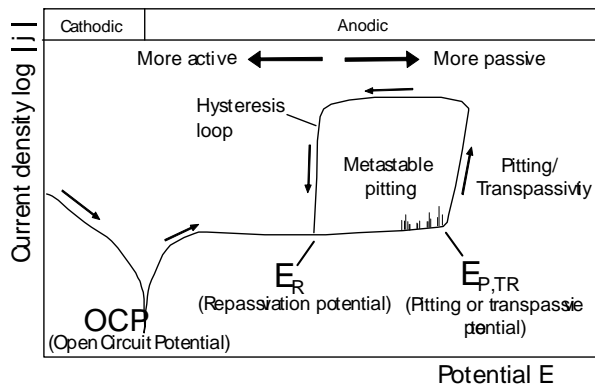


Fig. 10 Schematic current density polarization curve of a passive metal.

a certain potential, called pitting potential  $E_p$  (Burststein, 2010). It marks the transition from passivity to transpassivity and is characterized by a massive increase in current density during polarization. It should be noted that other names and subscripts (e.g. breakdown potential  $E_B$ ) for the pitting potential exist, as pitting is not necessarily the form of corrosion which occurs (Frankel, 2003). By exceeding the  $E_p$  the transpassive regime is entered and that the transpassive behavior may be masked by oxygen evolution at high anodic potentials (McDonald *et al.*, 1979).

The repassivation potential  $E_R$  marks a significant drop of current density to pre-breakdown level after switching the polarization direction and a stably growing pit will cease to grow (Anderko *et al.*, 2004). It is generally accepted that materials with higher values for  $E_p$  and  $E_R$  are more resistant to pitting corrosion (Frankel, 2003). The potential range between  $E_p$  and  $E_R$  is sometimes referred to as the domain of metastable pitting. Metastable pitting means that pit growth continues even at lower potentials than  $E_p$ . These pitting events are on a micron-scale and usually die out within seconds or less (Frankel, 2003).

Once these potentials are experimentally determined by potentiodynamic polarization and *OCP* measurements, they can be used to evaluate the integrity of the passive film and the susceptibility to localized corrosion. The following relations are generally accepted in corrosion research. If  $OCP \ll E_p$ , no pitting corrosion will occur, whereas pitting corrosion takes place when  $OCP \geq E_p$ . If  $OCP \approx E_p$ , pitting corrosion may occur, since even slight changes in the oxidizing capacity of the brine may raise the *OCP* to  $E_p$  (Pohjanne *et al.*, 2008). Therefore, the difference between the  $E_p$  and *OCP*, or domain of passivity, is a margin of safety and can be used as a measure of the susceptibility to pitting corrosion (Neville and Hodgkiess, 1996; Igual-Munoz *et al.*, 2004). Other authors (Blasco-Tamarit *et al.*, 2008; Bäßler *et al.*, 2009) suggest  $OCP < E_R$  as the principal constraint for pitting stability, considering the capability of repassivation. The range of stable passivation between  $E_R$  and *OCP* is a more conservative measure of the pitting susceptibility (Frankel, 2003). The difference between  $E_p$  and  $E_R$ , the domain of metastable pitting or metastable passivation, is related to the extent of hysteresis in a cyclic polarization curve. Generally, alloys that are susceptible to pitting corrosion exhibit a large hysteresis. For a material that is very susceptible to pitting, the *OCP* will be higher than  $E_p$  and the material will spontaneously pit at the *OCP* (Frankel, 2003).

Tab. 3 Technical and experimental parameter for electrochemical measurements.

Electrochemical measurements		
Electrode surface area	0.76	cm <sup>2</sup>
Temperature	80	°C
pH	4.8	
Critical current density	100 (for 0.76 cm <sup>2</sup> )	μA
Start of polarization	200 (cathodic to the <i>OCP</i> )	mV
Scan rate	0.16 (as recommended by ASTM G5-82)	mV s <sup>-1</sup>
Data acquisition (potentiodynamic pol.	1	Hz
Data acquisition ( <i>OCP</i> measurements)	0.1	Hz
Duration of <i>OCP</i> measurements	48	h

### 6.3 Test metals

A total of 13 metals were tested in the entire study. However, the focus changed over the work and so the test materials. The used materials are given in the individual experimental sections of chapter 7-9.

We tested commonly used casing and pipe steels (Fe-based mild steels **API N80**, **API P110**, **P235GH**, and **P265GH**), standard stainless steels (**430F**, **316L**, and **316Ti**), and promising candidates for geothermal applications (**alloy 904L**, duplex alloy **318L**, super-duplex **alloy 31**, Nickel-base **alloys 59**, **625**, and **Titanium gr. 2**). The materials have been chosen on the basis of their specification and commercial availability. The nominal average composition based on four individual elementary analyses, pitting resistance equivalents (*PRENs*) for stainless steels and Nickel alloys, and a cost comparison are given in Tab. 4. The microstructure of the mild steels was determined on the basis of micrographs (Fig. 11).

For the corrosion experiments the samples were either cut as rectangular coupons or slices depending on the received geometry. Maximum size was 50x15x4 mm in case of rectangular coupons or 30 mm in diameter and 4 mm thickness in case of circular slices. The autoclave coupons were provided with a hole for mounting. According to the ASTM G 1-03, the metal samples were manually ground using SiC abrasive paper (120, 320, and 1000 grit), washed with pure water, degreased in acetone, dried, and weighed.



Tab. 4 Chemical compositions of test materials (including subsidiary information); Microstructure: F: Ferrite; P: Pearlite; A: Austenite; D: Duplex (Austenite/Ferrite); \* PREN = %Cr + 3.3 %Mo + 16 %N according to (Gräfen and Kuron, 1996); \*\* In relation to mild steel; costs according to Alloy calculator© (metalprices.com) (date: April 2012).

Material	Mild steels						Stainless steels						Ni-based alloys		Non-ferrous alloy
	API N80	API P110	P235GH	P265GH	430F	316L	316Ti	318LN	904L	31	59	625	Ti gr. 2		
C	0.07	0.413	0.075	0.164	0.17	0.026	0.03	0.029	0.014	<0.002	0.03	0.047	0.0095		
Si	0.308	0.026	0.015	0.221	0.477	0.503	0.596	0.628	0.62	0.059	<0.0019	0.0039	<0.0029		
Mn	0.37	0.152	0.404	0.882	1.49	1.47	1.86	1.54	1.12	1.88	0.214	0.074	<0.0033		
P	0.0028	0.015	0.011	0.0035	0.049	0.044	0.035	0.03	0.027	0.015	<0.002	<0.002	n/a		
S	0.0049	0.0025	0.013	<0.0007	0.227	0.023	0.013	0.01	<0.0011	0.0011	0.0011	0.0028	n/a		
Cr	0.037	0.065	0.032	0.123	16.46	16.52	16.7	22.92	19.37	27.31	23.16	20.83	0.014		
Mo	0.012	0.037	0.004	0.019	0.232	2.1	2.14	2.88	4.2	6.84	16.23	9.27	<0.0068		
Ni	0.042	0.063	0.029	0.024	0.234	10.09	10.72	5.48	24.03	30.63	59.23	61.12	0.014		
Al	0.05	0.004	0.046	0.03	0.0071	0.009	0.018	0.033	0.036	0.055	0.173	0.204	0.0039		
Co	0.0075	0.0097	0.0073	0.004	0.033	0.179	0.177	0.144	0.094	0.07	0.037	0.032	n/a		
Cu	0.096	0.115	0.093	0.021	0.119	0.438	0.494	0.311	1.22	0.966	0.003	0.011	<0.0046		
Nb	<0.0007	0.002	<0.0007	<0.0007	<0.001	<0.001	0.02	<0.001	0.012	<0.001	0.035	3.76	n/a		
Ti	0.0014	0.0021	0.0009	0.0035	0.0052	0.011	0.208	0.0089	0.017	0.017	0.017	0.351	99.85		
V	0.0035	0.137	0.0033	0.0047	0.038	0.077	0.095	0.139	0.089	0.03	0.108	<0.0002	0.0032		
W	0.013	<0.01	0.011	<0.01	<0.013	0.094	0.117	0.04	0.152	0.358	0.115	0.105	n/a		
Pb	<0.0034	0.0041	0.011	<0.0034	0.014	0.013	0.015	0.013	<0.003	<0.003	0.0005	0.001	n/a		
Sn	0.005	0.011	0.0066	0.0033	0.0088	0.013	0.017	0.0085	0.0045	0.0034	0.0079	0.025	n/a		
As	<0.0037	0.021	<0.0037	<0.0037	n/a	n/a	n/a	n/a	n/a	n/a	n/a	n/a	n/a		
Zr	0.0031	0.004	<0.0012	0.0038	n/a	n/a	n/a	n/a	n/a	n/a	0.023	0.051	<0.0072		
Ca	0.0008	0.0002	0.002	0.0009	n/a	n/a	n/a	n/a	n/a	n/a	n/a	n/a	n/a		
Ce	0.0076	0.0051	<0.0035	<0.0035	<0.0036	0.023	0.03	0.015	0.031	0.032	n/a	n/a	n/a		
Ta	0.0099	0.012	<0.0046	0.0069	n/a	n/a	n/a	n/a	n/a	n/a	n/a	n/a	n/a		
B	0.0004	0.0007	0.0014	0.0004	0.05	0.015	0.0054	0.0041	0.0033	0.0031	0.017	0.0007	n/a		
Zn	0.019	0.014	<0.0009	0.014	n/a	n/a	n/a	n/a	n/a	n/a	n/a	n/a	n/a		
La	<0.0009	<0.0009	<0.0009	<0.0009	n/a	n/a	n/a	n/a	n/a	n/a	n/a	n/a	n/a		
Fe	99.22	97.23	99.23	98.47	80.38	68.36	66.7	65.77	48.96	31.71	0.586	4.11	0.02		
Micro-structure	F >95%	P > 50%	F >95%	F, P	F	A	A	D	A	A					
PREN*	-	-	-	-	17	27	27	34	36	52	47	54	-		
Costs**	1	1	1	1	1.7	8.3	8.3	7.1	19.4	31	>50	>50	16.2		

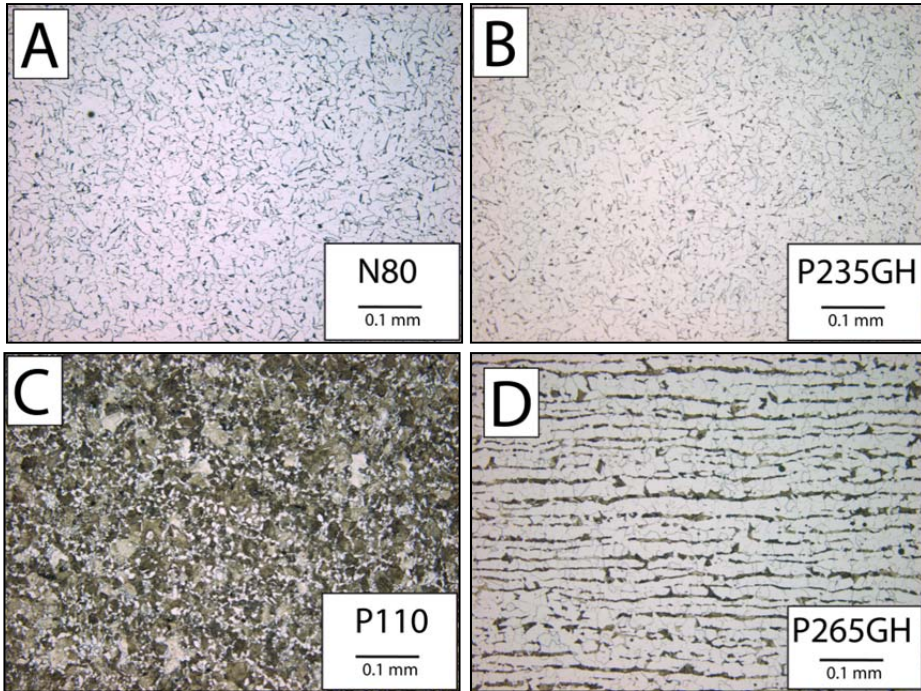


*Fig. 11 Representative micrographs of mild steels grades; (A) N80 and (B) P235GH: Ferrite-dominated microstructure; (C) P110: Pearlite-dominated microstructure; (D) P265GH: Ferrite-Pearlite duplex microstructure.*

## 6.4 Test solutions

The laboratory experiments were carried out with natural geothermal brines or with synthetic solutions which were prepared in the laboratory. The geothermal brines were sampled in the surface installations of the two geothermal sites, Soultz and Bruchsal, by flashing and cooling to ambient pressure and temperature. Representative compositions are given in Tab. 5. A very detailed brine analysis from Soultz is the result of an extensive sampling campaign and is given in Tab. 11. Synthetic solutions for the reverse polarization in chapter 7 were prepared from pure water by mixing with different amounts of lab grade NaCl.

Tab. 5 Representative brine analyses from Soultz-sous-Forêts and Bruchsal (Pauwels et al., 1993).

	pH	Na g l <sup>-1</sup>	K g l <sup>-1</sup>	Ca g l <sup>-1</sup>	Mg mg l <sup>-1</sup>	Cl g l <sup>-1</sup>	SO <sub>4</sub> mg l <sup>-1</sup>	SiO <sub>2</sub> mg l <sup>-1</sup>	Br mg l <sup>-1</sup>
<b>Soultz GPK1</b>	4.5-5	28.2	3.32	6.73	150	58.5	215	97	299
<b>Bruchsal GB2</b>	≈5	36.8	3.22	7.89	403	74.3	243	30.7	-
	B mg l <sup>-1</sup>	F mg l <sup>-1</sup>	Sr mg l <sup>-1</sup>	Li mg l <sup>-1</sup>	Ba mg l <sup>-1</sup>	Fe mg l <sup>-1</sup>	Rb mg l <sup>-1</sup>	Cs mg l <sup>-1</sup>	TDS g l <sup>-1</sup>
<b>Soultz GPK1</b>	34	3.9	480	123	12.3	232	25.1	15.7	98.4
<b>Bruchsal GB2</b>	27.4	0.4	-	166	4	69.8	1.9	2.2	123

## 6.5 Analysis of post-exposure coupons

Scanning electron microscopy (SEM) energy dispersive x-ray (EDX) were used to analyze the characteristics of corrosion and scalings on post-exposure samples. Furthermore, the penetration depth in case of localized corrosion was determined. Prior to the analysis, the samples were sputtered with a 5–10 nm carbon layer. SEM images were made with an FEI Quanta 650 FEG at an acceleration voltage of 15 kV. EDX analyses were performed with a BRUKER Quantax.

In order to evaluate and analyze corrosion and scaling the corrosion results were complemented by several analytical techniques. Light optical microscopy was used to determine the corrosion morphology and the microstructure of the metal samples.

## 6.6 $E_h$ - $pH$ diagrams

Pourbaix (1963) established his electrochemical concepts to the study of corrosion and published the “Atlas of Electrochemical Equilibria” for all elements known at that time. He defined the terms of passivity, immunity and corrosion. His biggest achievement is the derivation of  $E_h$ - $pH$  diagrams, often referred to as Pourbaix diagrams, which are still invaluable tools in understanding complex corrosion mechanisms and enable the relevant thermodynamic parameters in a corrosion system to be evaluated.

The  $E_h$ - $pH$  diagrams generated in this study were derived by using the Outokumpu software “HSC chemistry 5.1” with the integrated thermodynamic and thermochemical database (Roine, 2006).



## 7 Laboratory and on-site studies on metal corrosion

### 7.1 Objectives

This work represents the foundation for the whole research on corrosion and scaling in the Upper Rhine graben with its enormous geothermal potential. The hot brines encountered in deep rock formations carry some corrosive constituents (e.g. chloride, carbon dioxide) and set up a harsh environment which challenges many engineering materials. In this study we applied electrochemical measurements and conducted *in situ* exposure tests and compared the results. We intended to get a better understanding of corrosion processes taking place in hot geothermal brines and to evaluate influencing parameters.

### 7.2 Methodology and experimental

The first step was to develop the experimental skills to apply methods from corrosion research in the geothermal framework. Two established methods of corrosion research have been applied in this work: (1) potentiodynamic polarization measurements on coupons exposed to Soultz brine have been carried out in the laboratory, and (2) weight loss method has been used to quantify corrosion on coupons, which were exposed to 80 °C geothermal brine in the *in situ* corrosion bypass at the Soultz site. A special remark has been done on the comparison of the results obtained by the different methods. While the weight loss method is relatively straightforward, electrochemical techniques require a more profound knowledge of the corrosion system and often produce rather qualitative than quantitative results. For this reason we checked the accuracy and reproducibility of potentiodynamic polarization in several runs.

The experiments were carried out in order to study the corrosion behavior of alloyed and non-alloyed metals exposed to hot brine. The chosen material spectrum includes conventional mild steels (**P235GH**, **N80**, and **P110**), which are commonly used for casing or tubing applications. Furthermore standard stainless steels (**430F**, **316L**, **316Ti**, and **904L**), which are often the choice for corrosive media in related industries. Nickel-base alloy **625** was chosen due to its specification as a promising material. The compositions of the materials are given in Tab. 4.

The experiments were carried out in the on-site corrosion bypass in Soultz or by using water sampled on the surface installation in Soultz. A detailed brine composition and details about the on-site corrosion bypass are given in Tab. 2 and chapter 6.1.1, respectively.

## 7.3 Results and discussion

### 7.3.1 Mild steels

Mild steel coupons were exposed to geothermal brine in the corrosion bypass at Soultz. Maximum exposure time was 5 months. Exemplarily SEM images of corroded surfaces are shown in Fig. 13 for steel **N80**. The surfaces were roughened and both uniform corrosion and shallow pitting could be observed. After 5 months, the maximum penetration depth was 101  $\mu\text{m}$  for **N80**. For all mild steels, corrosion rates calculated by weight loss method were below 0.19  $\text{mm y}^{-1}$ . As shown in *Tab. 6* the corrosion rate are in a relatively narrow range.

*Tab. 6 Corrosion rates of mild steels after in situ exposure; \*Baticci (2009).*

<b>Mat'l</b>	<b>Exposure time h</b>	<b><math>\omega</math> <math>\text{mm y}^{-1}</math></b>
<b>N80*</b>	645.5	0.15
<b>N80</b>	3693.5	0.13
<b>P110*</b>	645.5	0.15
<b>P110</b>	3693.5	0.19
<b>P235GH</b>	886.33	0.14

During both time spans, scales formed on the surface becoming successively adherent. However, this increasing strength does not lead to a significant reduction of the corrosion rate. The scale formed after 5 months could only be removed by acid treatment. The composition of the scale was inhomogeneous. Nevertheless, exemplarily compositions from spot analysis of different samples are given in Tab. 7. Scales on **N80** and **P235GH** samples mainly consist of Fe phases, most likely oxides and/or hydroxides. **P110** shows a Pb-rich carbonate scale with minor amounts of Sb. The results of the scale analysis agree with observations made by Baticci (2009, 2010).

Tab. 7 Scaling analysis from spot analysis (wt%).

	C	O	Cl	Na	Ca	Mn	Fe	As	Sr	Mo	Sb	Ba	Pb
<b>N80</b>	3.5	25.8	3.5	-	1.2	1.3	39.5	3.1	0.7	3.4	1.7	4.8	9.8
<b>P110</b>	16.5	7.4	-	-	-	-	1.1	2.8	1.2		8.3	-	61
<b>P235GH</b>	4.5	26.4	2.6	1.8	1.2	-	30.2	6.5	0.6	3.8	2.8	1.6	16.1

Potentiodynamic polarization measurements were performed with mild steels exposed to geothermal brine. Current density potential curves are given in Fig. 12. They reveal a very similar electrochemical behavior of the different mild steels, even though the microstructure is different. **N80** and **P235GH** have a ferrite-dominated microstructure and **P110** a pearlite-dominated microstructure (Fig. 11).

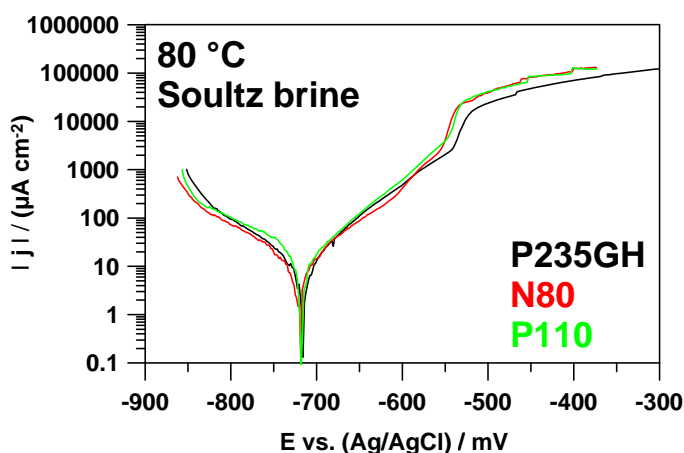


Fig. 12 Potentiodynamic polarization curves of mild steels (P235GH, N80, and P110) exposed to 80 °C Soutz brine.

The anodic and cathodic branches of the polarization curves exhibit *Tafel* behavior. Consequently, the corrosion rates can be determined. Eq. 7 yields uniform corrosion rates  $<0.2 \text{ mm y}^{-1}$ . All electrochemical data are given in Tab. 8. After polarization, **N80** samples were examined by SEM (Fig. 13). No scales could be observed on the surface. The form of attack, however, is comparable to the *in situ* experiments. In general, roughening of the surface could be discerned. In addition, uniform attack and surface shallow pitting was found. Maximum penetration depth was about 26  $\mu\text{m}$ .

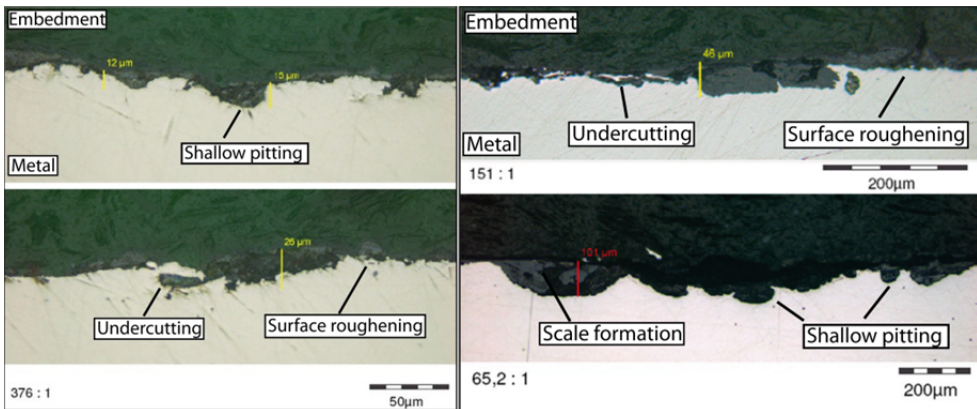


Fig. 13 SEM images of corroded N80 surfaces: (left) post-polarization surface of N80 in Soutz brine; uniform corrosion, shallow pitting and undercutting are the dominant forms of corrosion; (right) after exposure in the in situ corrosion bypass in Soutz; exposure time 50 days (top) and 153 days (bottom); uniform corrosion, shallow pitting and scale formation can be discerned.

### 7.3.2 Stainless steels

Stainless steel coupons were exposed to geothermal brine in the corrosion bypass for 1 month. All stainless steels were macroscopically blank after extraction from the bypass. For **316L** and **904L** no corrosion features could be discerned and weight loss was very low. The calculated uniform, corrosion rates are given in Tab. 9. **430F** exhibited some pits with a depth of around 100  $\mu\text{m}$  (Fig. 14).

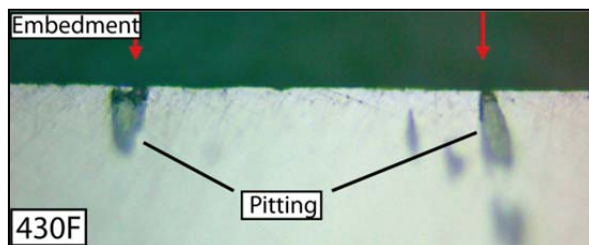


Fig. 14 Pitting corrosion on a **430F** surface after 4-week exposure in the in situ corrosion bypass.

To assess the accuracy of the results, an error analysis has been performed by a series of measurements with **316L** in untreated 80 °C Soutz brine. As can be seen in



Fig. 15, the shape of the curves is almost identical and the  $OCP$  and the  $E_p$  only vary in a narrow range. Significant deviation occurs after switching to cathodic direction. However, this implies that the reproducibility of measurements is fairly good. Moreover, reference experiments were performed at regular intervals according to ASTM G5-82.

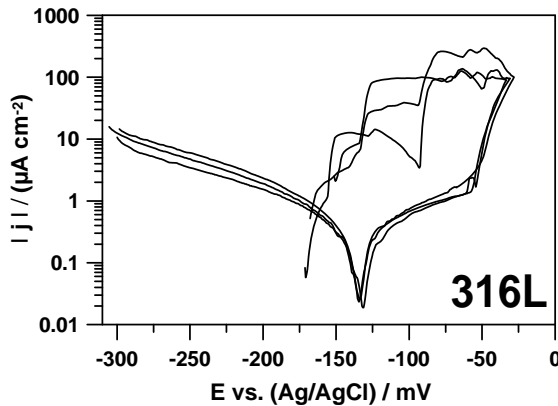


Fig. 15 Reproduction measurements of 316L in untreated 80 °C Sultz brine.

Fig. 16 shows the current density-potential-curves of stainless steels. The curves do not show *Tafel* behavior but active/passive behavior. Post-polarization coupons show that under these test condition pitting is the intrinsic form of corrosion when the stability limit is overstepped. This means that these materials are more or less susceptible to pitting. An assessment of pitting susceptibility can be obtained by comparing  $OCP$  to  $E_p$ .

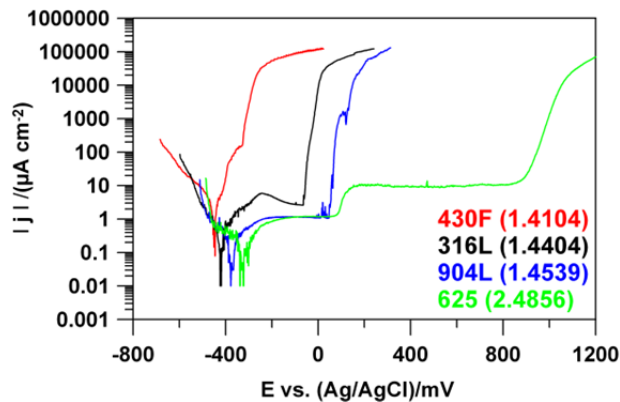


Fig. 16 Polarization curves of different alloys in 80 °C Sultz brine.

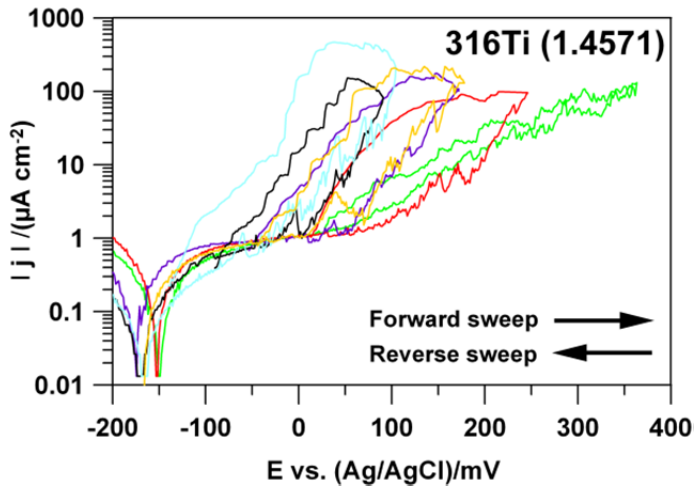


Fig. 17 Cyclic polarization curves of 316Ti in synthetic NaCl brine with different chloride concentrations at ambient temperature; green  $0.5 \text{ g l}^{-1}$ , red  $1 \text{ g l}^{-1}$ , purple  $5 \text{ g l}^{-1}$ , yellow  $10 \text{ g l}^{-1}$ , black  $25 \text{ g l}^{-1}$ , and blue  $50 \text{ g l}^{-1}$ .

**430F** does not exhibit a range of passivity and the current density strongly increases from the *OCP*. In contrast, **316L** and **904L** show a range of passivity with a very discrete  $E_p$ . The passive current density, however, is significantly lower for **904L** and indicates a stronger passive film. The electrochemical data are given in Tab. 8.

This observation can be related directly to the alloy content. The constituents of the alloy and their individual nobility have a major effect on the electrochemical behavior during polarization. The order of corrosion potentials toward more positive values is consistent with the ranking of the alloys toward a more noble behavior. Potentiodynamic polarization with a reverse sweep was performed in a synthetic NaCl solution at room temperature to study the repassivation behavior after pitting initiation. In these experiments, the chloride concentration of the synthetic solution was varied ( $0.5\text{-}50 \text{ g l}^{-1}$ ). The results for **316Ti** in chloride solutions of different concentrations are shown in Fig. 17. Since the chloride ion has a negative effect on the stability of passive films, the pitting potential is shifted toward more negative (less noble) potentials. Furthermore, increasing hysteresis at higher chloride levels can be observed by reverse polarization. Low concentrations of chloride do not initiate pitting corrosion. For concentrations around  $50 \text{ g/l}$ , the repassivation potential is near the *OCP*, meaning that

once pitting initiates, repassivation is hardly possible. Elevated temperatures will increase the susceptibility to pitting corrosion and shift the  $E_p$  in the cathodic direction.

Tab. 8 Electrochemical data from potentiodynamic polarization of different metals exposed to 80 °C Soutz brine (\*Alloy 625 does not show pitting).

Mat'l	OCP mV	$\beta_a$ mV	$\beta_c$ mV	$j_{corr}$ $\mu\text{A cm}^{-2}$	$E_p$ mV	$E_p$ -OCP mV	$\omega$ $\text{mm y}^{-1}$
<b>Mild steels</b>							
P235GH	-716	72.9	-93.3	15.5	-	-	0.180
P110	-717	66.0	-63.0	15.2	-	-	0.177
N80	-717	76.7	-106.0	12.1	-	-	0.140
<b>Stainless steels</b>							
<b>430F</b> (1.4104)	-450	-	-	-	-316	134	-
<b>316L</b> (1.4404)	-415	-	-	-	-50	365	-
<b>904L</b> (1.4539)	-368	-	-	-	58	426	-
<b>Ni-based alloy</b>							
625 (2.4856)	-257	-	-	-	*	-	-

### 7.3.3 Ni-based alloy

**Alloy 625** does not show any visible corrosion attack after *in situ* exposure and has a very low uniform corrosion rate (Tab. 9). After extraction from the bypass, the coupons were blank.

After potentiodynamic polarization measurements, **alloy 625** exhibits uniform corrosion, even at higher anodic potentials. It exhibits a wide range of passivity, with a very low passive current density. The sharp increase in current density at 900 mV indicates breakdown of passivity and transpassive dissolution. It should be noted that at high anodic overpotentials water oxidation will occur on the electrode surface, which masks the inherent transpassive dissolution process.

### 7.3.4 Method comparison

The polarization results and weight loss results from exposure experiments were compared with regard to corrosion rates and modes of corrosion (Tab. 9). It should be noted that corrosion rates obtained by these methods are difficult to compare, since electrochemical measurements are an instantaneous method to determine the electrochemical behavior under scaling-free laboratory conditions, while weight loss exposure take place under flow conditions including scaling effects. Nevertheless, good

agreement was found for mild steels, with the results obtained by polarization being slightly higher than those obtained by weight loss method. This indicates, that scalings formed during the exposure period only offer minor protection.

With regard to the corrosion rate, no comparison can be done for the alloyed materials, as they lack *Tafel* behavior. However, a qualitative evaluation can be given. The polarization curve for **430F** shows no indications for stable passivation and pitting seems to very likely. This could be corroborated with results from *in situ* exposure.

**316L** does not show any weight loss in after exposure and seems to be stable. However, pitting is a spontaneous process and a long-term prediction is hardly possible. The polarization measurements indicate that **316L** is in the passive state with a difference of 365 mV between the  $E_p$  and the *OCP*. Nevertheless, pitting is a permanent threat to this material. **904L** exhibits very good passivation properties in the polarization measurements. The exposure tests corroborate a stable state of passivation. If this material is brought to its stability limits it will also respond undergo pitting. **Alloy 625** has excellent passivation properties and does not respond with pitting after polarization. However, the weight loss of this material is slightly higher than for **316L** and **904L**.

Tab. 9 Comparison between results from potentiodynamic polarization and weight loss experiments; P: pitting corrosion; U: uniform corrosion; \* Baticci (2009).

Mat'l	Cr+Ni+Mo %	Potentiodynamic polarization		Weight loss exposure	
		$\omega$ mm y <sup>-1</sup>	Mode of corrosion	$\omega$ mm y <sup>-1</sup>	Mode of corrosion
<b>Mild steels</b>					
N80	0.091	0.18	U	0.15*	U
P110	0.165	0.14	U	0.15*	U
P235GH	0.065	0.18	U	0.14	U
<b>Stainless steels</b>					
<b>430F</b> (1.4104)	16.9	-	P	0.0028	P
<b>316L</b> (1.4404)	28.7	-	P	0	-
<b>904L</b> (1.4539)	47.6	-	P	0	-
<b>Ni-based alloy</b>					
<b>625</b> (2.4856)	91.2	-	U	0.0008	-

## 7.4 Concluding remarks

This study represents a first step to understand the corrosion of metals exposed to a geothermal environment with its special characteristics. Furthermore, it gives a conservative stability evaluation for common engineering materials. Two different methods of corrosion research have been applied, potentiodynamic polarization measurements in the laboratory and weight loss measurements after *in situ* exposure in Soultz-sous-Forêts.

Particularly the application of electrochemical techniques is very useful on the way to understand corrosion. Corrosion as a rather macroscopic process can be broken down to the surface reactivity of the metal/brine interface. Polarization curves contain information about the thermodynamic behavior of the metal exposed to the electrolyte. The immanent mode of corrosion for each metal could be identified by electrochemical polarization.

Uniform corrosion is the dominant form of corrosion for mild steels. Mild steels corrode with uniform corrosion rates  $<0.2 \text{ mm y}^{-1}$ . Microscopically, shallow pitting and undercutting can be observed. The microstructure seems to have a rather small influence on the involved corrosion modes as well as on the corrosion rate. The results obtained by *Tafels* method and *in situ* exposure tests correlate well, whereas scaling builds up during exposure experiments. The adherence of the scaling increases and we assume that the effect of scaling on corrosion will therefore successively increase.

In contrast to mild steels the stainless steels have a high resistance against uniform corrosion, but are susceptible to pitting corrosion. The vulnerability to pitting can be assessed by potentiodynamic polarization. A useful indicator is  $E_p\text{-OCP}$ , which defines the range of passivity. Corrosion resistance of the steels decreases in the following order: **904L**, **316L**, and **430F**. This directly correlates with the alloy content, expressed by the sum of chromium, nickel, and molybdenum. The latter steel failed in exposure tests, whereas the other two were stable in 4-week exposure tests. However, since corrosion is a spontaneously induced process, long-term stability of stainless steels remains uncertain. Long-term exposure tests are therefore necessary.

A special remark has to be made on the chloride content of geothermal brines. Particularly stainless steels are increasingly susceptible to localized corrosion, when the chloride concentration increases. Reverse polarization scans of the stainless steel **316Ti** were therefore used to evaluate the repassivation tendency, once pitting was initiated.

This capability for repassivation is successively hindered. If pitting occurs in 50 g/L chloride brine (comparable to Soultz brine), no repassivation is possible and existing pits will grow steadily.

The Ni-based **alloy 625** shows the best performance in terms of corrosion resistance. It does not respond with pitting in PP measurements and exposure tests. A wide range of passivity could be observed by PP measurements.

## 8 Corrosion and scaling in an operating geothermal power plant

### 8.1 Objectives

Natural geothermal brines are complex multi-component systems with numerous dissolved constituents that promote corrosion. The degradation of metallic construction materials is therefore a major concern for operators in geothermal industry. Scaling and its prevention are further technical challenges. The knowledge of the process environment with its physicochemical parameters is therefore essential for proper plant design and corrosion engineering.

In the first study the formation of scaling could be observed on post-exposure coupons. We hypothesized that the newly formed scaling will have an effect on corrosion and we can establish a corrosion-scaling relationship to make reliable predictions about long-term materials behavior. Hence, various experiments have been carried out in order to illuminate of time and temperature dependence of corrosion and scaling.

### 8.2 Methodology and experimental

Several aspects have been focused in this study. It provides the results from an *in situ* brine monitoring campaign, which can be regarded as unique, at least for URG geothermal sites. Furthermore, exposure experiments have been conducted in the laboratory autoclave and in the on-site corrosion bypass in Soultz. Corrosion rates were determined by the weight loss method. The scalings have been analyzed via SEM/EDX with regard to compactness and composition. The test conditions for both exposure environments are given in Tab. 10.

Tab. 10 Experimental conditions in the exposure environments; NCG: non-condensable gases; \* Operating parameters measured, \*\* According to Sanjuan et al. (2010), \*\*\* according to Baticci (2009).

Autoclave			On-site bypass Soultz		
Temperature	20,80,160	°C	Temperature	≈ 60– 80*	°C
Pressure	20	bar	Pressure	Max. 20	bar
CO <sub>2</sub> partial pressure	20	bar	CO <sub>2</sub> fraction (NCG)	50 – 90**	%
pH	≈ 4.5	-	pH	≈ 4.6 – 4.8	
Stirring	50		Flow rate	≈ 4***	m <sup>3</sup> h <sup>-1</sup>
Exposure time	1 – 5		Flow velocity	≈ 0.3	m s <sup>-1</sup>
			Exposure time	1 - 5	months

### 8.3 *In situ* brine monitoring during operation

One of the different tasks of BRGM with the funding and collaboration of EEIG “Exploitation Minière de la Chaleur” is a continuous *in situ* monitoring of the conductivity, pH, and  $E_h$  of the fluid circulating in the EGS pilot plant. In March 2009, the probes which continuously measure these parameters as well as temperature were installed in the “Geochemistry–Corrosion” skid located directly upstream of the reinjection of the fluid into the well GPK-3 (Fig. 8A). The temperature and pressure conditions in this skid are generally close to 60–80 °C and 20 bars, respectively. As shown by the most recent chemical analyses performed by the BRGM laboratories, the fluid presently circulating in the pilot plant mainly consists (97–99%) of native geothermal brine (NGB) which is an Na–Ca–Cl fluid with a TDS value close to 100 g/l (Sanjuan *et al.*, 2010; Sanjuan, 2011, 2012; Sanjuan, 2012).

The probes installed in the skid are a YOKOGAWA 4USF-PG-120 cell, a temperature sensor, a DYNAPROBE ST864-R33H-U02E1 combined pH electrode with temperature compensation, and a DYNAPROBE ST864-RPBO-A02EB redox electrode. An LTH MPD53-P2 pH meter and a LTH MPD53-P1 voltmeter located in a cabinet supplied by SYSTEM C INDUSTRIE are applied for the continuous measurements of T, pH, and  $E_h$ . A SC450G-A-A/UM EXA conductimeter by YOKOGAWA is used for conductivity measurements. At the beginning, conductivity was measured using HEITO measurement equipment that was then replaced by the present system in September 2010. EEIG preferred to centralize all the data in an acquisition and transmission system covering the complete pilot plant. Consequently, the acquired data are regularly transferred by EEIG to BRGM.

All the technical instruments used for the continuous measurements were tested, controlled, and validated at 25 °C and atmospheric pressure in the BRGM laboratories (measurement repeatability, uncertainty estimations etc.) in early 2008, before they were installed in the skid. Absolute uncertainty of pH measurements at 25 °C was estimated to be 0.05 pH, relative uncertainties of  $E_h$  and conductivity measurements at 25 °C were evaluated to be 3% and 6%, respectively.

An example of continuous monitoring carried out in the Soultz plant is given in Fig. 18 for the period from September 2010 to February 2011 (the measurements were made every 5 min). The following main conclusions can be drawn from this monitoring program:



Continuous conductivity measurements on a very saline and reduced fluid, such as the Soultz native geothermal brine (NGB), remain problematic, even during a short period of time, because these measurements are not stable in time and very quickly perturbed, probably by the progressive formation of scale deposits on the inner surfaces of the conductivity cell. These scale deposits that are also observed on the surface of the other electrodes and in other surface installations (heat exchangers, down-hole pump, filters, etc.) mainly consist of barite–celestine and polymetallic sulfide, such as galena, pyrite or sphalerite (Gentier *et al.*, 2011; Scheiber *et al.*, 2012). Low radioactivity is induced by  $^{226}\text{Ra}$  and  $^{228}\text{Ra}$  which substitute Ba in the barite–celestine deposits ( $\beta$  and  $\gamma$  radioactivity) and by  $^{210}\text{Pb}$  in the galena deposits ( $\beta$  radioactivity) (Gentier *et al.*, 2011). Contrary to the pH measurements, the response time of the  $E_h$  electrode is relatively slow after some technical operations (exchanger changes, for example) have modified the operation of the “Geochemistry–Corrosion” skid. Although it is difficult to perform accurate continuous measurements of pH and  $E_h$  over periods longer than 2–3 months because of the formation of these scale deposits (electrodes must be cleaned or replaced systematically), these measurements yielded and confirmed the most representative values of pH and  $E_h$  for the NGB at Soultz.

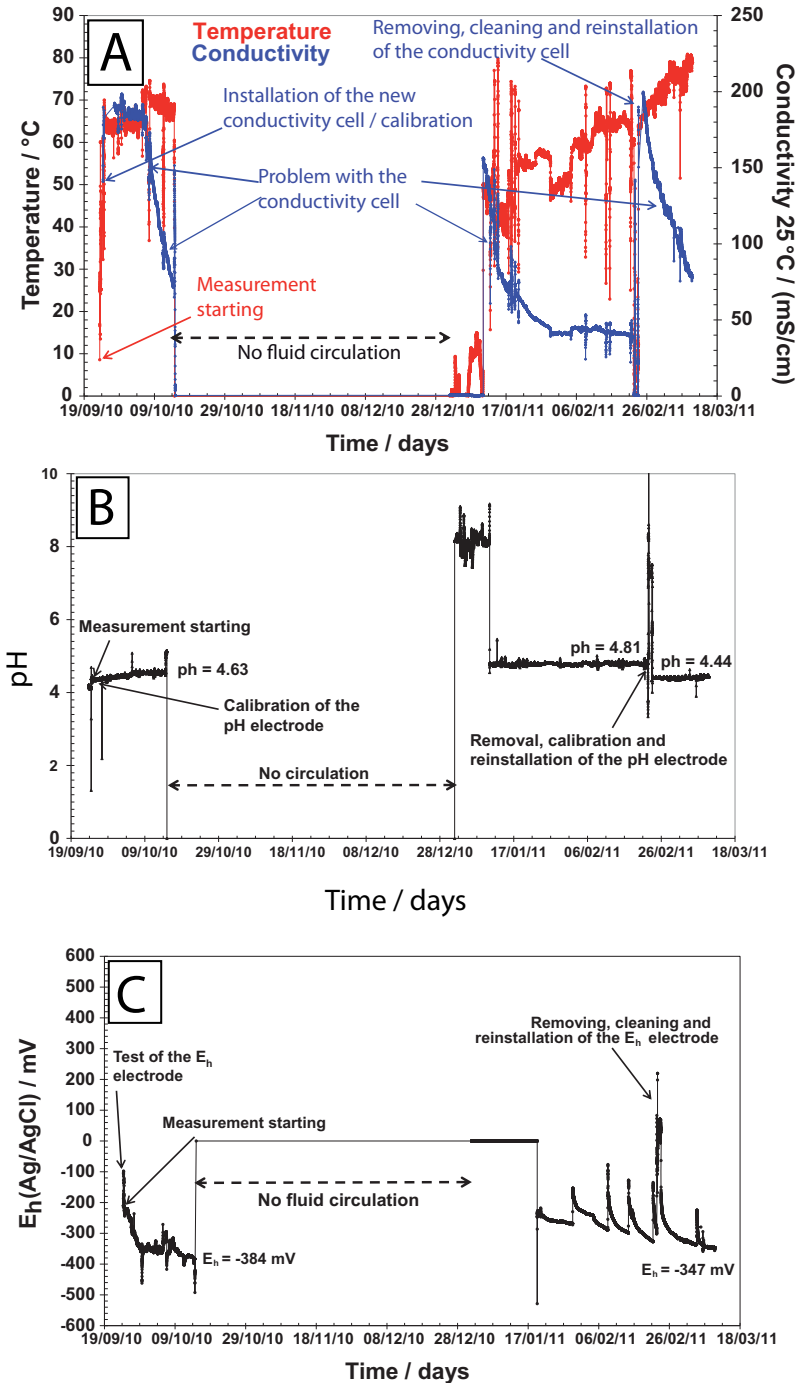


Fig. 18 In situ brine monitoring between September 2010 and February 2011 by the geochemistry–corrosion skid located near the wellhead of the reinjection well GPK-3; (A) Temperature (red) and conductivity (blue); (B) pH measurement; (C) Redox potential  $E_h$  (Ag/AgCl).

The pH values obtained (4.63–4.81) are in a good agreement with the pH value close to  $5.0 \pm 0.2$  estimated for a  $\text{CO}_2$  partial pressure of 6 bars and for temperature values ranging from 200 to 230 °C, at which the NGB is assumed to be equilibrated with the reservoir rocks (Sanjuan, 2011; Gentier *et al.*, 2011; Sanjuan, 2012). Temperature values close to 200 °C were measured in the bottom-hole of the deeper wells (at about 5 km). If the  $E_h$  (Ag/AgCl) values measured around 70 °C (-390 mV/-384 mV) are corrected by eliminating the potential of the reference electrode, a higher value of  $-215 \pm 15$  mV (vs. standard hydrogen electrode SHE) is characteristic of a deep brine in reduced environment. For higher temperatures (230 °C), geochemical modeling yielded estimations around -180 mV (SHE) (Sanjuan, 2012).

Since the beginning of the Soultz investigations, very few representative analyses of the NGB have been made available because of the frequent contamination by drilling circulating fluids or injected waters (Sanjuan *et al.*, 2010). The chemical monitoring of the fluid circulating in the pilot plant (Sanjuan, 2011; Sanjuan, 2012) also is an excellent opportunity to collect the most representative samples of the NGB never sampled before. Several samples of water, steam, and associated incondensable gases were and will be collected using a cyclonic phase mini-separator constructed by EEIG (Sanjuan, 2011; Sanjuan, 2012). Most of the chemical and isotopic analyses were and will be performed in the BRGM laboratories.

A comparative study of all the data acquired since 1999 allows for the identification of the most representative chemical and isotopic compositions of the NGB and associated incondensable gases for the time being. These data are reported in Tab. 11. While the compositions of the dissolved major species and of some dissolved trace elements (Br, Sr, Li, B, Rb, Cs, Ge, etc.) are relatively precise, those of the dissolved infra-trace elements (Al, Fe, Pb, Zn, Cu, Ni, etc.) often remain inaccurate. Additional fluid sampling (in particular, recommended bottom-hole sampling), chemical and isotopic analyses are necessary to improve the accuracy of these data and complete them (in particular, isotopic data for boron or neodymium and radioisotope analyses). For the incondensable gases, the results obtained using the EEIG cyclonic mini-separator differ considerably from previous results (Sanjuan *et al.*, 2010), but seem to be most representative. Additional data will be used to validate and complete them.

Tab. 11 Most representative chemical and isotopic composition of the Soultz native geothermal brine (NGB) and the incondensable gases, reconstructed from a comparative study and the most recent data analysed by BRGM. Radioisotope results were found in Surbeck (2008). Additional results are required to validate and complete these data.

<b>Physicochemical parameters</b>				
Density @ 20 °C	1.07 ± 0.003	g cm <sup>-3</sup>	Cl	59 ± 2 g l <sup>-1</sup>
Conductivity @ 25 °C	130 ± 20	mS cm <sup>-1</sup>	Na	27.5 ± 1 g l <sup>-1</sup>
TDS	98 ± 2	g l <sup>-1</sup>	K	3.0 ± 0.4 g l <sup>-1</sup>
pH @ 70-80 °C	4.7 ± 0.2		Ca	6.7 ± 0.5 g l <sup>-1</sup>
E <sub>h</sub> @ 70-80 °C (Ag/AgCl)	-215 ± 20		Mg	120 ± 10 mg l <sup>-1</sup>
pH @ 200-230 °C	5.0 ± 0.2		HCO <sub>3</sub>	90 ± 20 mg l <sup>-1</sup>
E <sub>h</sub> @ 200-230 °C (Ag/AgCl)	-180 ± 10		SO <sub>4</sub>	190 ± 20 mg l <sup>-1</sup>
<b>Isotopic values &amp; radioactivity (brine)</b>				
δD	-41.3 ± 1.3	‰	NO <sub>3</sub>	< 0.5 mg l <sup>-1</sup>
δ <sup>34</sup> S (SO <sub>4</sub> )	12.8 ± 0.4	‰	SiO <sub>2</sub>	250 ± 40 mg l <sup>-1</sup>
δ <sup>7</sup> Li	0.1 ± 0.5	‰	HS	1.3 ± 0.5 mg l <sup>-1</sup>
δ <sup>18</sup> O	-2.7 ± 0.4	‰	Br	250 ± 30 mg l <sup>-1</sup>
δ <sup>18</sup> SO <sub>4</sub>	5.2 ± 0.3	‰	F	4.5 ± 1.0 mg l <sup>-1</sup>
<sup>87</sup> Sr/ <sup>86</sup> Sr	0.711264		PO <sub>4</sub>	2.7 ± 0.5 mg l <sup>-1</sup>
<sup>226</sup> Ra	844 ± 26	mBq l <sup>-1</sup>	NH <sub>4</sub>	21 ± 3 mg l <sup>-1</sup>
<sup>228</sup> Ra	716 ± 41	mBq l <sup>-1</sup>	B	35 ± 3 mg l <sup>-1</sup>
<sup>234</sup> U	12 ± 4	mBq l <sup>-1</sup>	Sr	430 ± 30 mg l <sup>-1</sup>
<sup>238</sup> U	5 ± 3	mBq l <sup>-1</sup>	Ba	10 ± 3 mg l <sup>-1</sup>
<sup>222</sup> Rn	25 ± 2	Bq l <sup>-1</sup>	Li	150 ± 20 mg l <sup>-1</sup>
			Rb	22 ± 3 mg l <sup>-1</sup>
<b>Isotopic values &amp; radioactivity (gas)</b>				
δ <sup>13</sup> C (CO <sub>2</sub> ) <sub>PDB</sub>	-3.9 ± 0.1	‰	Cs	14 ± 2 mg l <sup>-1</sup>
δ <sup>18</sup> O (CO <sub>2</sub> ) <sub>PDB</sub>	-4.8 ± 0.1	‰	As	8 ± 2 mg l <sup>-1</sup>
δ <sup>18</sup> O (CO <sub>2</sub> ) <sub>SMOW</sub>	26 ± 0.1	‰	Ge	50 ± 5 μg l <sup>-1</sup>
<sup>222</sup> Rn	94 ± 1	kBq m <sup>-3</sup>	Al	70 ± 30 μg l <sup>-1</sup>
<b>Gas composition</b>				
Gas liquid ratio	0.16	mass%	Fe	60 ± 40 mg l <sup>-1</sup>
CO <sub>2</sub>	86.0 ± 3	mol%	Mn	15 ± 3 mg l <sup>-1</sup>
N <sub>2</sub>	10.0 ± 0.5	mol%	Pb	280 ± 100 μg l <sup>-1</sup>
CH <sub>4</sub>	2.3 ± 0.2	mol%	Zn	2800 ± 700 μg l <sup>-1</sup>
H <sub>2</sub>	0.9 ± 0.1	mol%	Cu	2 - 260? μg l <sup>-1</sup>
He	1.0 ± 0.1	mol%	Ni	0.4 - 205? μg l <sup>-1</sup>
Ar	0.05 ± 0.01	mol%	Cr	<0.1 - 43? μg l <sup>-1</sup>
C <sub>2</sub> H <sub>6</sub>	0.014 ± 0.002	mol%	Co	1.8 - 60? μg l <sup>-1</sup>
H <sub>2</sub> S	<0.005	mol%	Cd	2.1 - 28? μg l <sup>-1</sup>
O <sub>2</sub>	<0.001	mol%	Ag	0.9 ± 0.4 μg l <sup>-1</sup>
C <sub>3</sub> H <sub>8</sub>	0.0008 ± 0.0002	mol%	U	<0.05 μg l <sup>-1</sup>
ΣC <sub>4</sub> H <sub>10</sub>	0.00025 ± 0.00005	mol%	Th	<0.1 - 1.0? μg l <sup>-1</sup>

## 8.4 Results and discussion

### 8.4.1 Mild steels

#### 8.4.1.1 Corrosion observations

Autoclave and *in situ* exposure tests with mild steel coupons (**P110**, **N80**, **P235GH**, and **P265GH**) were performed in Soultz geothermal brine. All mild steel grades were subject to corrosion in the test environments, uniform corrosion being the most prominent form of attack (Fig. 19A and Fig. 19B). The corrosion rates are given in Fig. 20.

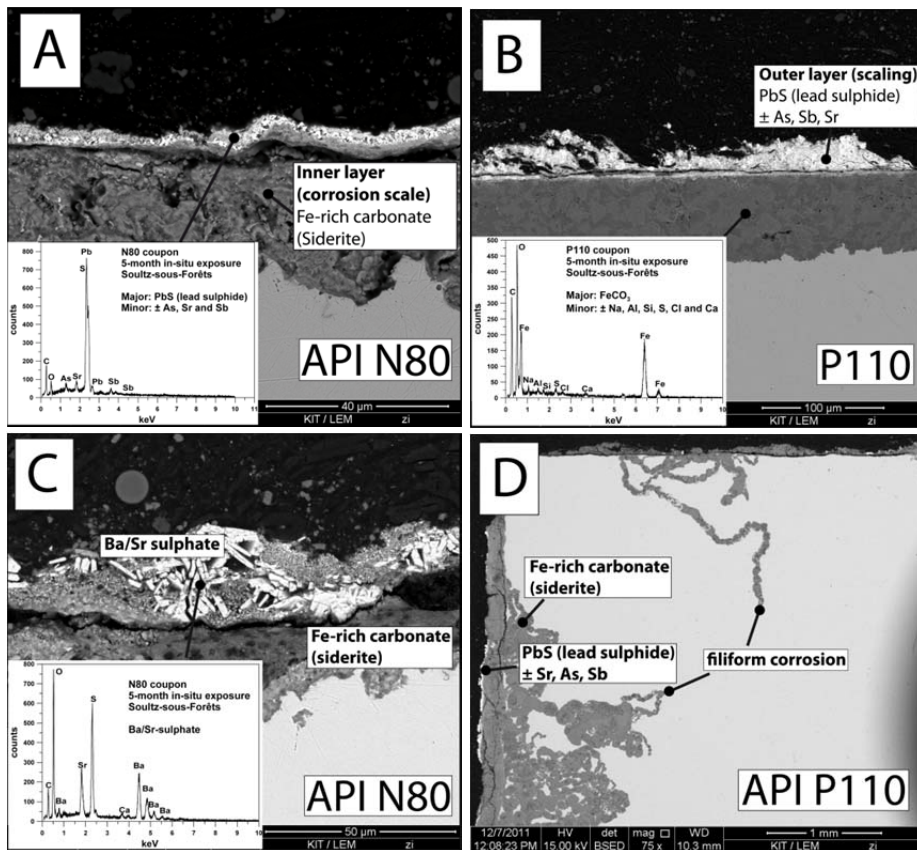


Fig. 19 SEM images of post-exposure mild steel coupons and EDX spectra of encountered mineral phases: (A) API N80 after 4 weeks in situ exposure, (B) API P110 after 5 months in situ exposure, (C) API N80 after 5 months in situ exposure, (D) API P110 after 5 months in situ exposure with filiform corrosion features.

Autoclave experiments at 20, 80, and 160 °C with **P235GH** samples were conducted. They reveal a strong temperature and time dependence of the corrosion intensity as can be seen from Fig. 20. The corrosion rates for all three temperatures were below  $0.75 \text{ mm y}^{-1}$  after 800 h, with decreasing tendency. We consider long-term corrosion rates below  $0.2 \text{ mm y}^{-1}$  to be a realistic estimation, which is acceptable for thick-walled components. This corresponds to a wall thickness reduction of 4 mm within 20 years of service life. The highest corrosion intensity occurs in the 80 °C corrosion environment. Consequently, this has implications for operating geothermal systems. Higher corrosion intensity will occur on the reinjection side of the power plant. The observation that mild steel corrosion rates in  $\text{CO}_2$ -containing media decrease with increasing temperature was made by other researchers (Zhao *et al.*, 2009). *In situ* corrosion rates are generally below  $0.19 \text{ mm y}^{-1}$  after 5 months of exposure. Surprisingly, ferritic **N80** seems to be superior to pearlitic **P110**. However, in this concern more experiments have to be conducted, in order to corroborate the results.

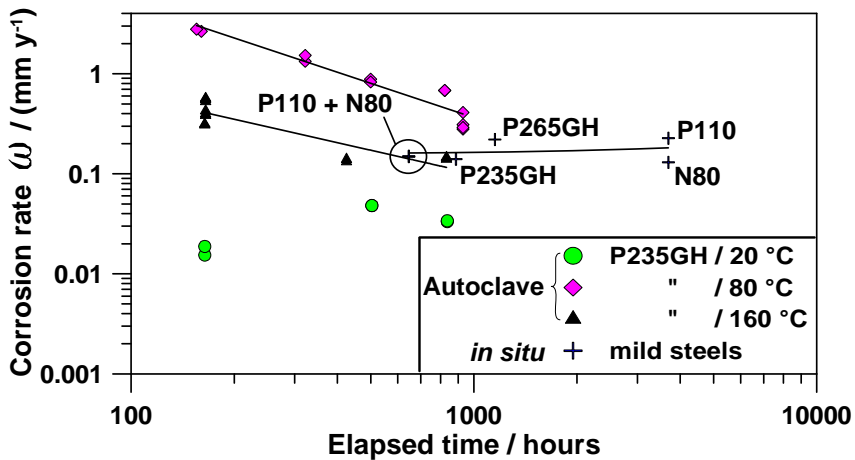


Fig. 20 Mild steel corrosion rates from *in situ* and autoclave exposure tests at different temperatures.

The observations in this study are consistent with results reported in literature, where mild steels corrode in all geothermal corrosion campaigns. Corrosion rates of up to  $2.4 \text{ mm y}^{-1}$  are reported for 1020 carbon steel and 4130 steel (Carter and Cramer, 1992). Localized corrosion with pit depths of up to 0.4 mm could also be found after 15 days of exposure. However, it was found that the corrosion rates also decrease strongly with time due to the formation of a corrosion scale. Miranda-Herrera *et al.* (2010) report

corrosion rates of  $3.3 \text{ mm y}^{-1}$  for ASTM A53 B and API L80 in the room temperature geothermal brine from Cerro Prieto, Mexico.

Beside uniform corrosion, localized corrosion features, mainly shallow pitting and filiform corrosion (Fig. 19D) could be observed after *in situ* exposure. Filiform corrosion appears to be the most severe form of corrosion as penetration depths can exceed 1 mm. These threadlike features could be observed primarily on pearlitic **P110** coupons and may be the result of the microstructural heterogeneity of the corroding metal (Gutman *et al.*, 1969). The electrochemical heterogeneity of the microstructure (e.g. ferrite, pearlite, carbide) can induce potential differences (galvanic cells) and force localized corrosion. Han proposed a model in which localized corrosion is explained by galvanic coupling of two distinct areas, a bare steel surface (acting as an anode) and an siderite-covered steel surface (acting as a cathode) in a conductive  $\text{CO}_2$ -bearing brine (Han, 2009). Palacios and Shadley (1991) also suggest that an incomplete or loose coverage can induce pitting and that localized attack beneath pores can weaken the base of the scale and lead to disbonding.

#### **8.4.1.2 Scaling observations**

Corrosion of mild steels was accompanied by the formation of scaling on the initially blank surface. Hence, post-exposure coupons from *in situ* experiments were examined by SEM to study the scaling characteristics (Fig. 19).

SEM/EDX analyses reveal a characteristic duplex pattern on most of the samples, (Fig. 19A and Fig. 19B). Characteristic EDX spectra for the identified phases are also given. Fe-rich carbonate (siderite) of variable thickness with minor amounts of Na, Al, Si, S, Cl, and Ca formed the inner layer and can be regarded as corrosion scale. Tabular-shaped Ba/Sr sulfates (barite–celestine solid solution) are the main constituents of the outer layer, often accompanied by a thinner layer of PbS containing minor amounts of As, Sb, and Sr (Fig. 19B and Fig. 19C). The outer layer can reach a thickness of around 50  $\mu\text{m}$  and can only be found on *in situ* coupons. As it is very porous and fragile, however, it is expected to provide no additional protection. The microstructure and mineralogy are consistent with observations made by Scheiber *et al.* (2012) and during the *in situ* brine monitoring. This deposit is mainly associated with the geothermal brine chemistry. The observation that sulfide minerals precipitate from the brine, even though the concentration of sulfide ions in the pristine brine is very low, suggests that sulphate-reducing mechanisms are involved. Anaerobic microbial activity might affect both

scaling and corrosion processes (Dinh *et al.*, 2004). The scaling dynamic and prevention are subjects of on-going research in Saultz (Scheiber *et al.*, 2012).

Scaling starts instantly after immersion and a siderite layer could be found after a few days of exposure, at least for 80 and 160 °C experiments. It is formed mainly by the Fe<sup>2+</sup> released from the substrate surface by corrosion and not from the bulk solution. The corrosion rate consequently has a strong effect on siderite precipitation. The fact that lower corrosion rates occur in the 160 °C experiments indicates that the formation of siderite is accelerated at higher temperatures. This seems plausible considering the retrograde solubility of siderite. It is assumed that two competing factors come into play. In general, a higher temperature directly causes higher corrosion rates by accelerating chemical and electrochemical reactions. Prior to any layer formation, the corrosion rate increases with temperature as expected. However, the solubility of siderite (Fe-carbonate) decreases and, thus, the precipitation rate increases with increasing temperature.

#### **8.4.1.3 Corrosion and scaling interaction**

In the following section, several aspects affecting the corrosion/scaling mechanisms will be elucidated on the basis of experimental observations and theoretical considerations. In general, there is a controversy about the passivating capability of siderite formed in CO<sub>2</sub> environments, as it is often found to be loose and porous, thus lacking its protective effect on the underlying substrate material. However, beneficial environmental circumstances can lead to the formation of a dense and adherent corrosion scale (siderite), which is capable of effectively preventing direct contact of the substrate material and the bulk solution. Our experimental observations show a strong interaction between corrosion and scaling. We found reliable evidence that the siderite layer formed in the test environments (*in situ* and autoclave) effectively lowers the corrosion intensity of the metal substrate. As a consequence, the performance of mild steels depends on the characteristics (microstructure and morphology) of the newly formed corrosion scale (Palacios and Shadley, 1991) which is, in turn, controlled by the microstructure and chemical composition of the substrate material and the temperature of formation (Lopez *et al.*, 2003). This passivating effect of siderite on mild steels was described by various authors (Palacios and Shadley, 1991; Heuer and Stubbins, 1999; Lopez *et al.*, 2003; Pfennig and Bäßler, 2009).



With regard to compactness, siderite of variable quality could be found on the post-exposure coupons. API **N80** exhibits a rather porous type of siderite layer (thickness approx. 30  $\mu\text{m}$ ) with a rather weak bonding to the substrate (Fig. 19A and Fig. 19C). In some parts, the layer is detached from the substrate or even missing. These characteristic features could be found on many of the samples with exposure times less than 5 weeks. Fig. 19B reveals that after 5 months of exposure, the siderite layer on **P110** had a thickness of around 100  $\mu\text{m}$  and was found to be more compact with a stronger bonding to the substrate. However, areas with weaker coverage and porous areas can be observed, too. Another observation is that the siderite layer thickens over time and that the layer can reach a thickness of around 200  $\mu\text{m}$  within 5 months of exposure. However, the average thickness is around 100  $\mu\text{m}$ . Considering a long-term corrosion rate of 0.2 mm  $\text{y}^{-1}$ , this means that the volumetric loss by surface recession was superimposed by the volumetric gain of siderite formation. However, it is difficult to establish a corrosion-scaling correlation on the basis of the samples available and more systematic research has to be conducted in this respect.

With respect to corrosion and scaling another aspect deserves attention. The hydrodynamic conditions (flow velocity, laminar or turbulent flow) in a pipe system affect corrosion and scaling (Palacios and Shadley, 1991; Nescic and Lee, 2003). However, it is still discussed how and to what extent corrosion is affected. Generally, it is accepted that corrosion intensity is lower in low-velocity environments (Nescic and Lee, 2003). Lopez *et al.* (2003) report higher corrosion rates in high-velocity environments due to the prevention of formation or removal of the corrosion scale. Nescic and Lee (2003) developed a mechanistic model which predicts a less protective siderite layer under flow conditions. At very high flow rates, erosion corrosion becomes another serious problem (Karlsdottir, 2012). However, as no reliable information about the flow conditions in the experiments is available, the corrosion and scaling results reported in this study cannot be evaluated with regard to flow conditions.

#### **8.4.2 Corrosion and scaling observations on alloyed and non-ferrous metals**

*In situ* and autoclave exposure experiments were conducted with various alloyed materials and non-ferrous **Ti gr. 2**. Tab. 12 summarizes the results obtained from the exposure tests. In most cases, the corrosion rates for each material are in good agreement, indicating sufficient reproducibility. Generally, the stainless steels and alloys

show a high resistance against uniform corrosion in the test environments. Most of the post-exposure coupons did not show any macroscopic corrosion and the surfaces were smooth and scaling-free, as revealed also by the SEM images (Fig. 21A). In case no localized corrosion occurred, uniform corrosion rates were below  $0.005 \text{ mm y}^{-1}$ . Previous research showed that Cr, Ni, and Mo-alloys passivate during exposure in the geothermal brine (Mundhenk *et al.*, 2013a, 2013b). It should be noted that longer exposure increase the significance of results.

Steel grade **430F** exhibits the lowest resistance of all alloyed materials with the highest weight loss in both exposure environments. SEM images reveal that pitting corrosion occurred along manganese sulfide inclusions, which represent chemical heterogeneities. This form of attack creates voids and preferable spots for further pit propagation (Fig. 21B).

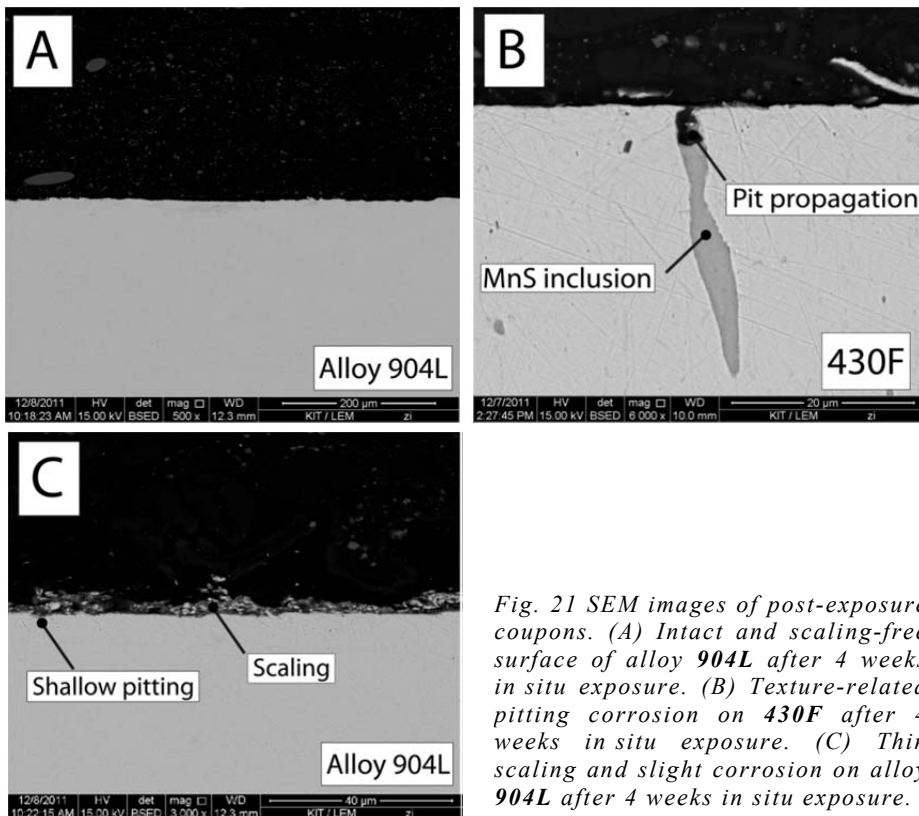


*Fig. 21 SEM images of post-exposure coupons. (A) Intact and scaling-free surface of alloy 904L after 4 weeks in situ exposure. (B) Texture-related pitting corrosion on 430F after 4 weeks in situ exposure. (C) Thin scaling and slight corrosion on alloy 904L after 4 weeks in situ exposure.*

No weight loss was measured for **316L**, **904L**, **alloy 31**, and **alloy 59** coupons after *in situ* exposure. The corrosion rate of  $0.0008 \text{ mm y}^{-1}$  for **alloy 625** appears surprisingly high compared to the other alloys, but is consistent for two samples. Some of the **316L** and **904L** coupons were partly covered with patches of a loose 10-20  $\mu\text{m}$  scaling layer of unknown composition after *in situ* experiments (Fig. 21C). Underneath this scaling layer, a slight corrosion attack can be recognized, showing slight uniform corrosion and shallow pitting of a few  $\mu\text{m}$  penetration depth. Thus, it is assumed that local corrosion cells develop between covered and uncovered regions. The local flow regime will be affected by scaling deposition promoting the formation of concentration cells. These observations indicate that scaling promotes corrosion and, most probably, vice versa.

The corrosion rates obtained by autoclave experiments are significantly higher for most materials. One **316L** sample underwent pitting, whereas one showed uniform corrosion only. This illustrates the spontaneous character of pitting. **316Ti** and **318LN** show a high resistance with very low and consistent corrosion rates. The corrosion rates for **904L** are consistent, but significantly higher than measured for the **316Ti** and **318LN** samples. **Alloys 59, 625, 31** and **Titanium gr. 2** show a slight weight gain after autoclave exposure.

Generally, a comparison of corrosion rates is complicated, as materials, procedures, exposure times, and environments usually differ in the studies available. However, they may be used to verify own results. For this purpose, literature results from exposure experiments in low-saline to highly-saline geothermal environments are summarized in Tab. 12. This table does not claim to be complete.

It should be noted that uniform corrosion is not the decisive corrosion form for this material group, as their susceptibility to pitting is of higher relevance. The use of electrochemical polarization techniques provides a powerful tool to characterize material behavior and to define limitations for each material. An electrochemical study of pitting susceptibility under geothermal conditions is subject of on-going research.

Considering the *in situ* and autoclave corrosion rates in comparison, it is apparent that the corrosivity in the autoclave experiments is higher than in the *in situ* environment. Possible explanations of the elevated corrosion intensity in the autoclave are: (1) a higher  $\text{CO}_2$  partial pressure leads to a lower pH than in the on-site environment, (2) flow conditions in the *in situ* experiments lead to a good mixing of the bulk brine solution, exacerbating the formation of concentration cells, and (3) the redox

state of the sampled and transported brine does not reflect its *in situ* state. This means that despite degassing and purging with CO<sub>2</sub>, no absolute absence of oxygen could be achieved.

Tab. 12 Uniform corrosion rates for stainless steels and alloys from *in situ* and autoclave exposure tests; results from exposure tests in geothermal environments for comparison; Square brackets [ ] indicate calculated ‘virtual’ uniform corrosion rates, neglecting localized corrosion; <sup>a</sup> Shut-down period from 04/06 to 08/10/11; effective exposure time under flow conditions in round brackets ( ).

	In situ exposure				Autoclave				Comparative results from literature					
	Exposure time / days	Corrosion rate / (mm y <sup>-1</sup> )	Localized corrosion?	Exposure time / days	Corrosion rate / (mm y <sup>-1</sup> )	Localized corrosion?	Exposure time / days	Corrosion rate / (mm y <sup>-1</sup> )	Localized corrosion?	Exposure time / days	Corrosion rate / (mm y <sup>-1</sup> )	Localized corrosion?	Test environment / site	Reference
Mat'l														
430F	34	[0.0019]	-	9	[0.091]	+	45	0.305	-				Salton Sea brine / TDS 160-210 g/l / 215 °C	Carter and Cramer, 1992
	34	[0.0028]	+	9	[0.063]	+	22	0.048	-				East Mesa brine / TDS ≈ 20 g/l / 152 °C	McCawley et al., 1981
				35	[0.027]	+	15	0.0025	+				East Mesa brine / TDS ≈ 20 g/l / 152 °C	DeBerry et al., 1978
				35	[0.027]	+								
316L	35	0	-	7	[0.0048]	+	168	0.0004	-				Artificial MB fluid / TDS ≈ 1 g/l / 100 °C	Klapper et al., 2012
	35	0	-	7	0.0005	-	168	0.0009	-				Artificial MB fluid / TDS ≈ 1 g/l / 150 °C	McCawley et al., 1981
	185 <sup>a</sup> (61)	0	-			-	22	<0.0025	-				East Mesa brine / TDS ≈ 20 g/l / 152 °C	DeBerry et al., 1978
185 <sup>a</sup> (61)	0	-			-	15	<0.00127	+				East Mesa brine / TDS ≈ 20 g/l / 152 °C	DeBerry et al., 1978	
316Ti				28	0.0009	-								
				28	0.0007	-								
318LN				35	0.0005	-	168	0.0009	-				Artificial MB fluid / TDS ≈ 1 g/l / 100 °C	Klapper et al., 2012
				35	0.0005	-	168	0.0009	-				Artificial MB fluid / TDS ≈ 1 g/l / 150 °C	
Alloy 904L	27	0	-	7	0.0027	-								
	27	0	-	7	0.0027	-								
	185 <sup>a</sup> (61)	0	-			-								
	185 <sup>a</sup> (61)	0	-			-								
Alloy 31	29	0	-	32	0	-	168	0.0007	-				Artificial NGB fluid / TDS ≈ 260 g/l / 100 °C	Klapper et al., 2012
	29	0	-	32	0	-	168	0.0007	-				Artificial NGB fluid / TDS ≈ 260 g/l / 150 °C	
Alloy 59	29	0	-	35	0	-	168	0.0006	-				Artificial NGB fluid / TDS ≈ 260 g/l / 100 °C	Klapper et al., 2012
	29	0	-	35	0	-	168	0.0005	-				Artificial NGB fluid / TDS ≈ 260 g/l / 150 °C	
Alloy 625	21	0.0008	-	28	0	-	15	0	-				Salton Sea brine / TDS 160-210 g/l / 232 °C	Carter and Cramer, 1992
	21	0.0008	-	28	0	-	22	<0.0025	-				East Mesa brine / TDS ≈ 20 g/l / 152 °C	McCawley et al., 1981
				15	<0.00127	-	15	<0.00127	-				East Mesa brine / TDS ≈ 20 g/l / 152 °C	DeBerry et al., 1978
Ti gr.2				35	0	-	109	<0.025	-				Raft River brine / TDS ≈ 1.2 g/l / 133 °C	DeBerry et al., 1978

## 8.5 Concluding remarks

The present study represents another step towards a better understanding of the interrelated processes of corrosion and scaling in the geothermal brine of Soultz-sous-Forêts. The available instrumentation provides a unique opportunity to acquire physicochemical data of the processed brine over a long-term period. This data set is the basis of corrosion engineering considerations.

$E_h$  and pH measurements yield good results, which are consistent with modeling approaches. The brine is slightly acidic ( $\text{pH} \approx 4.7$ ) and is strongly reducing with respect to the SHE,  $E_h \approx 215 \text{ mV}$ . However, continuous *in situ* brine monitoring under operating conditions remains challenging. For example, conductivity measurements are quickly perturbed. Frequent cleaning of the electrodes is inevitable for accurate data acquisition. Several brine analyses identify Na, Ca, and Cl as the main constituents of the brine, contributing to more than 95% of the total salinity ( $\text{TDS} \approx 98 \text{ g l}^{-1}$ ). K, Mg,  $\text{SO}_4$ , Br, B,  $\text{NH}_4$ , Li, and Sr contribute to the overall chemistry in stable amounts. F, Ba, Ti, As, Rb, Cs, Fe, Ni, Cu, Co, Cr, Cd, Zn, Ag, and Pb are present in unstable concentrations. Some of these constituents are of special interest, as they either have a toxic nature (e.g. As, Pb) or are a potential source of precious elements (e.g. Li). The gas content accounts for approx. 0.16 mass% of the brine. Its composition is strongly dominated by  $\text{CO}_2$  with minor fractions of  $\text{N}_2$ ,  $\text{CH}_4$ ,  $\text{H}_2$ , and He.

Corrosion experiments were performed *in situ* and in the laboratory autoclave using the weight loss method. This method was applied successfully to quantify the corrosion and scaling behavior under operating geothermal conditions. The following conclusions can be drawn from coupon exposure experiments:

(1) Long-term uniform corrosion rates of mild steels are below  $0.2 \text{ mm y}^{-1}$ , with the highest corrosion rates measured in  $80 \text{ }^\circ\text{C}$  experiments; this corresponds to a wall thickness reduction of 4 mm within 20 years of service life; however, localized corrosion (filiform corrosion) can reach considerable penetration depths ( $>1 \text{ mm}$ ) and can lead to short-term failure.

(2) Corrosion of mild steels was accompanied by scaling, which contributes to the materials' resistance. The scaling is characterized by a duplex structure with an inner siderite layer of variable thickness and an outer layer of low-soluble Ba/Sr-sulfates and Pb-sulfides with minor amounts of As, Sb, and Sr. Especially the toxic nature of Pb and As has implications for filter cleaning and scale removal.

(3) Steel grade **430F** suffered pitting corrosion in *in situ* and simulated environments. The attack occurred along MnS inclusions in the microstructure. Hence, a low sulfur content is recommended for materials in contact with the processed brine. **316L** also suffered pitting corrosion, however, only in the autoclave experiments. Both steel grades are considered as inappropriate options for service under Upper Rhine graben geothermal conditions.

(4) Alloyed grades show a high resistance against uniform corrosion with corrosion rates below  $0.005 \text{ mm y}^{-1}$ . However, it should be noted that uniform corrosion is not necessarily the decisive corrosion form for this material group. Some of the alloyed test materials may be susceptible to localized forms of corrosion (e.g. shallow pitting), particularly underneath scaling patches. Long-term *in situ* tests and an electrochemical study with varying environmental factors are parts of ongoing research and will elucidate the individual pitting resistance of alloyed materials.

This experimental campaign is unique for the Upper Rhine graben (URG) with its enormous geothermal potential. Regarding the hydrochemistry and process parameters, Soultz and other operating and prospected geothermal sites in the URG have more similarities than differences. As a consequence, the observations made in Soultz, including the material selection guidelines, have regional relevance. This successful approach will be complemented by further investigations, including electrochemical polarization measurements and exposure tests under geothermal production conditions ( $T \approx 165 \text{ }^\circ\text{C}$ ).





## 9 Electrochemical study on corrosion of different alloys

### 9.1 Objectives

In a previous study various test metals (stainless steels, Ni-alloys and Titanium gr. 2) have been exposed to an 80 °C *in situ* environment in Soultz in order to evaluate and quantify the corrosion behavior (Mundhenk *et al.*, 2013). Most metals remain unaltered and the coupons show only little weight loss. Others, however, show features of degradation. For example, **316L** stainless steel was obviously challenged and some coupons showed pitting corrosion after few days of exposure. Given these results, the following question came up: How do these metals react in such a corrosive environment and in which way do we measure ongoing corrosion processes?

### 9.2 Methodology and experimental

This work is a pure laboratory work which focuses on the electrochemical behavior of alloys exposed to deaerated 80 °C geothermal brines containing CO<sub>2</sub>. Test materials were **316L**, **318LN**, **904L**, **alloy 31**, **alloy 625**, and **Titanium gr. 2**. Two natural brines, from Soultz and from Bruchsal, have been used for these experiments. Even though both brines are considered to be genetically related, they have unique characteristics in terms of composition (Pauwels *et al.*, 1993; Sanjuan *et al.*, 2010).

Electrochemical measurement (cyclic potentiodynamic polarization and *OCP* measurements) have been carried out with the parameters given in Tab. 13. Post-polarization coupons have been examined via light optical microscopy to study the corrosion behavior of the different alloys.  $E_h$ -*pH* diagrams have been computed in order to compare the calculated equilibrium potentials with results from *OCP* measurements and cyclic polarization.

Tab. 13 Test conditions for electrochemical measurements.

Test conditions for electrochemical measurements		
Electrode surface area	0.76	cm <sup>2</sup>
Temperature	80	°C
pH	4.8	
Chloride concentration	59 (Soulzt), 75.2 (Bruchsal)	g l <sup>-1</sup>
Total dissolved solids	97 (Soulzt), 123 (Bruchsal)	g l <sup>-1</sup>
Critical current density	100 (for 0.76 cm <sup>2</sup> )	μA
Scan rate	0.16 (as recommended by ASTM G5-82)	mV s <sup>-1</sup>
Data acquisition (potentiodynamic pol.)	1	Hz
Data acquisition ( <i>OCP</i> measurements)	0.1	Hz
Duration of <i>OCP</i> measurements	48	hours
Gas chemistry	CO <sub>2</sub> (technical grade 4.8)	

## 9.3 Results and discussion

### 9.3.1 Passivation observations

The electrochemical behavior in the test environments was derived by two series of measurements: potentiodynamic polarization and *OCP* measurements. Potentiodynamic polarization was used to study the passivation characteristics and the anodic and cathodic corrosion kinetics. Here, the corrosion process is accelerated by external voltage. In contrast, the *OCP* history is recorded without external stimulus, revealing the spontaneous behavior.

#### 9.3.1.1 Potentiodynamic polarization experiments

The cyclic polarization curves of all test materials in Soulzt and Bruchsal brine are shown in Fig. 22a-f. The curves exhibit pertinent features in the anodic branch, such as active/passive behavior, metastable pitting, and the onset of pitting or transpassive dissolution, respectively.

Except the **Ti alloy**, all materials show a hysteresis loop of various extents, which is confined by the  $E_{P(TR)}$  and  $E_R$ . Metastable pitting can but does not necessarily occur in this potential range. For **alloy 31**, **625**, and the **Ti alloy**, current density transients scarcely appeared in the curves, indicating an absence of metastable pitting, and good properties of the passive film. The hysteresis loops tend to be larger in Soulzt brine, at least for **316L**, **318LN**, and **904L** and indicate an inhibited capability for repassivation. For **alloy 31**, a larger hysteresis loop could be discerned in Bruchsal brine. In Soulzt brine, a distinct passivation potential can be observed. In general, the passive current densities are  $<3 \mu\text{A cm}^{-2}$ . Only in the case of **316L**, the passive current densities in both

brines exceed  $10 \mu\text{A cm}^{-2}$ . The passive current densities are similar, regardless of whether exposed to Soultz or Bruchsal brine. This indicates that the integrity of the passive film expressed by the passive current density is not sensitive to the increased salt content in Bruchsal brine. The  $E_p$  measured in Bruchsal brine is consistently lower than in Soultz brine and suggests an increased susceptibility to pitting corrosion. This observation that the  $E_p$  primarily depends on the chloride ion activity is generally accepted (Gräfen and Kuron, 1996; Burstein, 2010).

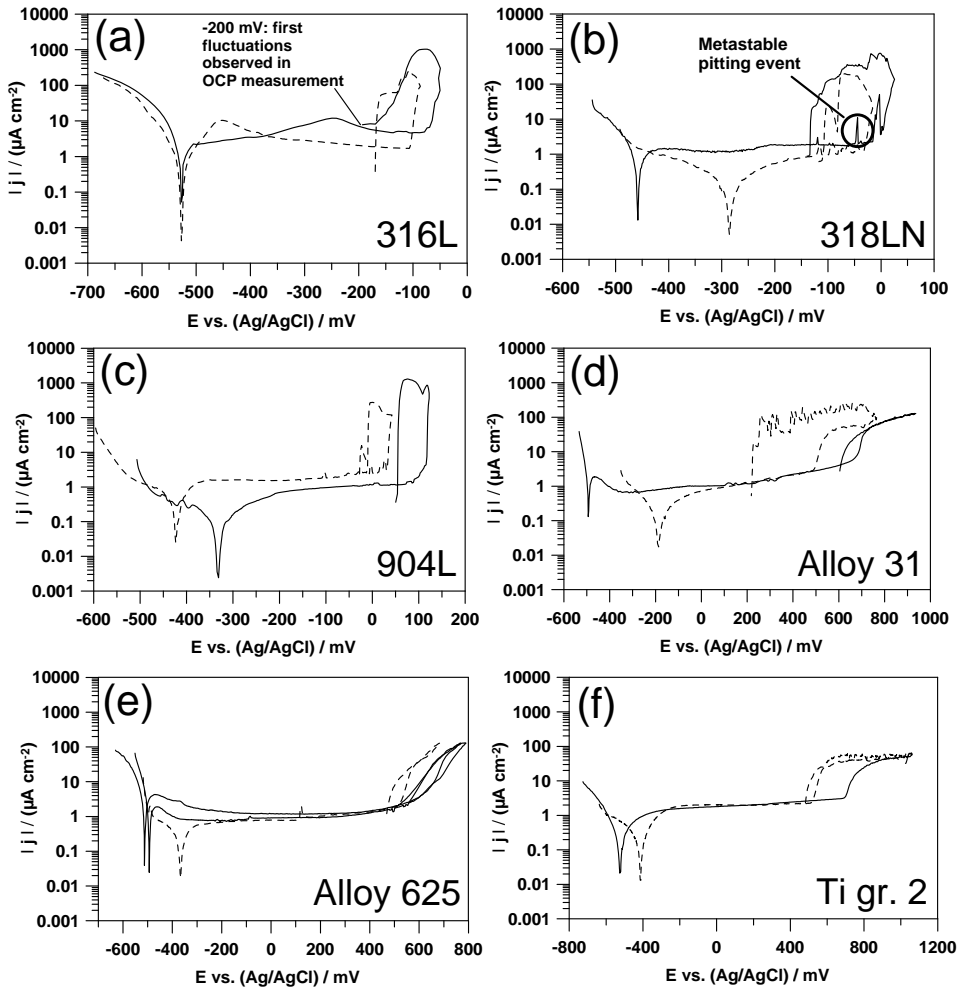


Fig. 22 Current density potential curves for all materials in both geothermal brines (Soutz: solid line; Bruchsal: dashed line; 80 °C, pH 4.8, CO<sub>2</sub> purged).

While the  $E_{PS}$  were found to be highly reproducible, the  $OCPs$  in the polarization curves and the  $E_{RS}$  have a larger scatter band in identical but independent measurements. It should be noted that the  $OCP$  from the polarization curves is less significant than the  $OCPs$  derived by  $OCP$  measurements over time. The electrochemical results are summarized in Tab. 14.

### 9.3.1.2 *OCP Measurements (spontaneous passivation observations)*

In the previous chapter, it could be shown that passivation could be achieved by anodic polarization. However, whether or not passivation also occurs spontaneously, which represents a more realistic corrosion scenario, is illuminated in this chapter.

Incipient  $OCP$  ennoblement during exposure could be observed in virtually all measurements in both, Bruchsal and Sultz brine. This indicates a high tendency for spontaneous passivation. If localized corrosion does not occur, the  $OCP$  will shift harmonically to noble direction until leveling off to a stable value. In the case of **318LN**, **alloy 31**, **625**, and the **Ti alloy** (Fig. 23b, d), the dislocation can approach several hundred millivolts, approx. 450 mV for the **Ti alloy**. This behavior reveals very good passivation properties. Incipient spontaneous passivation followed by an unsteady evolution, exhibiting potential drops and/or  $OCP$  fluctuations, could be observed for **316L** and **904L** (Fig. 23a, c), whereas the evolution of the  $OCP$  is both, hardly predictable and irreproducible. The given curves have to be considered exemplarily.

In most cases, the  $OCP$  ennoblement in Sultz is faster and more pronounced than in Bruchsal brine, i.e. the time to reach spontaneous passivation is shorter. Furthermore, the  $OCP$  evolution achieves higher values in Sultz brine, which indicates a higher tendency for passivation.

We found ambiguous behavior for **316L** in totally independent measurements (Fig. 23a). In Sultz brine, the spontaneous passivation process is interrupted by fluctuations. One curve exhibits discrete sets of  $OCP$  oscillation with increasing amplitudes, which can be explained by short-term activation and passivation changes. Discrete pits surrounded by tempering colors could be detected on this post-exposure coupon, which proves insufficient stability. Another measurement shows a very smooth spontaneous passivation, depassivation/activation and repassivation development (Fig. 23a, red curve), where it took more than 5 hours to achieve full  $OCP$  recovery. It is therefore assumed that a more substantial surface alteration occurred. In both cases, the interruptions start after exceeding a potential of -200 mV. The  $OCP$  in Bruchsal brine

shows a different evolution. The *OCP* is leveling off at a stable value around -165 mV with increased fluctuations towards the end of the experiment.

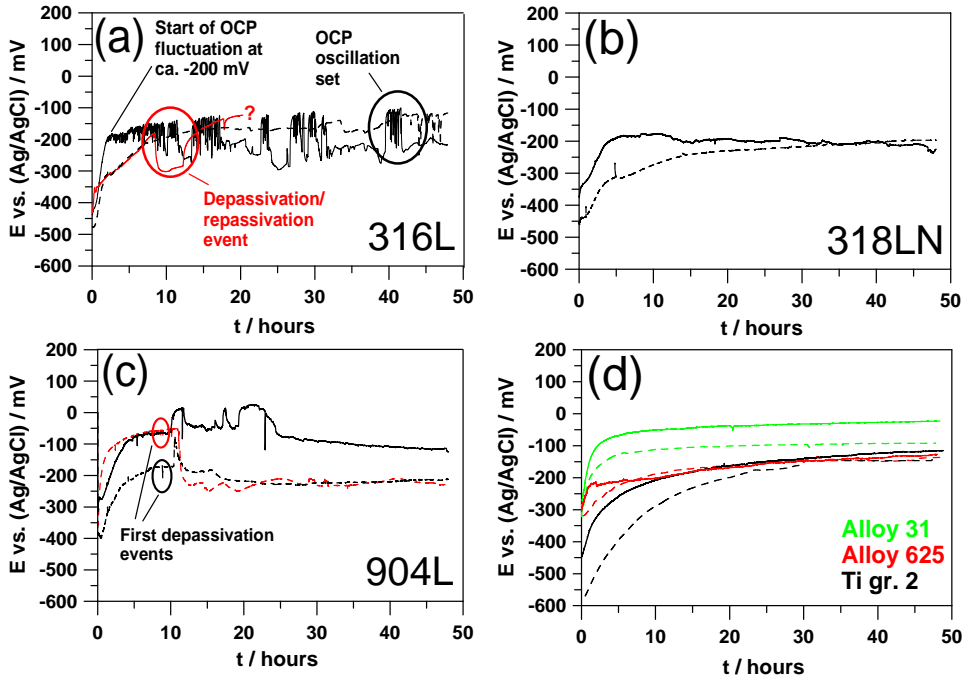


Fig. 23 48-hour *OCP* measurements of all materials in both geothermal brines (Soutlz: solid line; Bruchsal: dashed line); 80 °C, pH 4.8,  $CO_2$  purged.

Fig. 23c shows the *OCP* evolution for **904L**. Spontaneous passivation in Bruchsal brine is interrupted by drops to a more active potential. Incipient depassivation events as precursors can be discerned in the curve. The reproducibility is low in the first 10 hours but higher as the experiment proceeds. The major depassivation event takes place after approx. 10 hours, however, on a different potential level. One curve in Bruchsal brine shows a distinctive peak before dropping to more active values. In Soutlz brine, a more random evolution on a more passive potential level can be identified, lacking major depassivation events. The behavior in both brines, however, suggests incomplete passivation.

To sum up, the *OCP* measurements delivered significant results with regard to the passivation process. If depassivation occurs and the *OCP* fluctuates, this relates to

incomplete passivation, metastable or stable pitting activity, as in the case of **316L** and **904L**. We found a good reproducibility with regard to the onset of metastable pitting and/or depassivation events during the spontaneous ennoblement process. **318LN**, **alloy 31**, **625**, and the **Ti alloy** exhibit harmonic *OCP* equilibration with no depassivation tendency. These materials are present in a stable state of passivity.

### 9.3.2 Stability evaluation and corrosion observations

The stability in the test environment is discussed on the basis of electrochemical results,  $E_h$ -*pH* diagrams, the concept of pitting resistance equivalent number (*PREN*), and micrographic observations. The results from cyclic polarization and *OCP* measurements are summarized in Tab. 14. To reveal the individual corrosion characteristics, the alloys were polarized to high anodic overpotentials, simulating extreme conditions. Of principal interest is to determine the form of corrosion when the material is polarized beyond its stability. Given the limitations and simplistic nature of electrochemical measurement, the results enable us to make a conservative estimation whether or not corrosion, in whatever form, is likely to occur in 80 °C geothermal brine. It should be noted that this is a thermodynamic consideration. Pitting remains a spontaneous process and is related to the stochastic nature of corrosion.

Fig. 24 gives the  $E_h$ -*pH* diagrams for chromium and molybdenum (molality:  $10^{-6}$  each) in a 2-molal NaCl aqueous solution at 80 °C. These were computed by the Outokumpu software “HSC chemistry 5.1” with the integrated thermodynamic and thermochemical database (Roine, 2006). It should be noted that the chosen molality is fairly high for a dissolved corrosion product (Cook and Olive, 2012).

The passive region, where  $\text{Cr}_2\text{O}_3$  is thermodynamically stable, is relatively narrow from pH 3 to 5. The concentration of Cr strongly affects the extension of the  $\text{Cr}_2\text{O}_3$  stability field towards higher pH. For this reason the diagram has to be interpreted with caution. The location of the *OCPs* indicate, that the Cr-containing alloys that rely upon  $\text{Cr}_2\text{O}_3$  for corrosion protection are close to the  $\text{Cr}_2\text{O}_3/\text{Cr}(\text{OH})_4^-$  -transition and may therefore be at risk to corrode.

The passive region, where  $\text{MoO}_2$  is stable, widens towards lower pH. To higher potentials the region is bounded to stability fields of dissolved species. Especially the transition from  $\text{MoO}_2/\text{HMoO}_4^-$  puts the Mo-containing alloys at risk to corrode. The *OCPs* are very close to this transition and many of the major fluctuations in the *OCP* measurements occur in the range -100 to -200 mV. In particular, **316L** is in a good

agreement with this result. Depassivation and fluctuations (as a precursor of pitting corrosion) observed in the *OCP* measurement start by exceeding a potential of -200 mV, which marks the  $\text{MoO}_2/\text{HMoO}_4^-$  transition at a pH of 4.8. From a thermodynamic consideration it is supposed that the  $\text{MoO}_2$  component is crucial in conferring passivity to this alloy and that its selective dissolution accounts for the initiation of pitting.

On a cautionary note, however, MacDonald *et al.* (1979) demonstrated that minor components in alloys can have a strong influence on the electrochemical behavior. This illustrates the difficulties inherent in using  $E_h$ -*pH* diagrams for only the major components when analyzing the corrosion behavior of an alloy. For alloys that consist of essentially one component usually better predictions can be made. The property of  $\text{TiO}_2$  to serve as an excellent corrosion barrier is described elsewhere (e.g. Shoosmith and Noël, 2010).

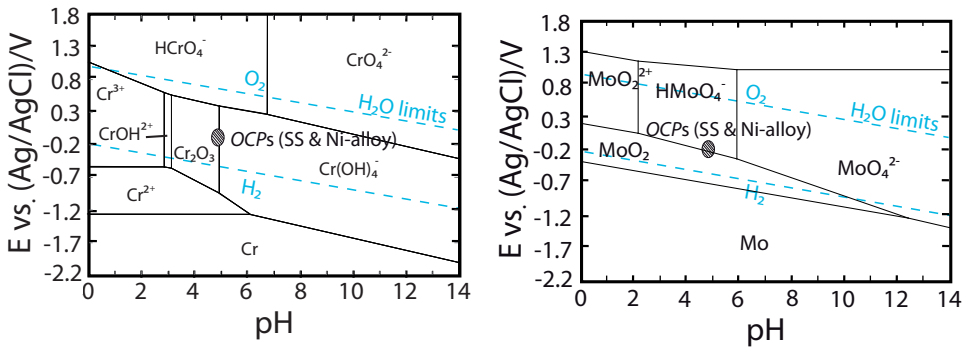


Fig. 24  $E_h$ -*pH* diagrams for the (Cr, Mo)-Na-Cl- $\text{H}_2\text{O}$  system at 80 °C; Molalities: Cr and Mo  $10^{-6} \text{ mol kg}^{-1}$ , NaCl  $2 \text{ mol kg}^{-1}$ ; the dotted lines indicate the thermodynamic stability field of  $\text{H}_2\text{O}$ . The OCPs are indicated by hatched ovals (SS: stainless steels).

Optical micrographs of selected post-polarization surfaces including the profile sections are shown in Fig. 25. Polarization information (max. polarization potential and resulting current) is given in the caption. It is evident that **316L**, **318LN**, and **904L** are prone to localized corrosion, mostly pitting, shallow pitting and crevice corrosion. The pit morphology of **318LN** is different to **316L** and **904L** and seems to be more controlled by the microstructural heterogeneity (austenite/ferrite). Alloy **31** shows an



affinity to crevice corrosion but usually tends to corrode in a uniform manner. In contrast, **alloy 625** and **Ti gr. 2** do not show any localized corrosion.

In general, the corrosion features discerned after exposure to Bruchsal and Soultz brine is similar, and comparable to the corrosion form observed in pure sodium chloride solutions of similar salinity. One interesting observation from a preliminary series of experiments is that the corrosivity in terms of current density, pitting potential, and hysteresis is higher in pure sodium chloride solutions compared to natural geothermal brines. Among the constituents in the geothermal brines, some may have an inhibiting effect. However, which chemical constituents or combination of constituents account for this effect is not adequately discovered for geothermal brines. Extensive research on this field has been conducted elsewhere (*i.a.* Leckie and Uhlig, 1966; Linter and Burstein, 1999).

As a measure for pitting stability, we used  $E_R - OCP$  to define the range of stable passivity, instead of using  $E_{P(TR)} - OCP$  for the whole range of passivity. This is due to the observation that metastable pitting events are common as the potential approaches  $E_p$ . For the  $OCP$  value, we either give the stabilized value or the maximum value ( $OCP_{max}$ ) in the case of a fluctuating or unsteady  $OCP$ .

The electrochemical results were combined with the  $PREN$  (eq.8) concept, which is an established way to rank the pitting susceptibility of stainless steels (Sedriks, 1979; Gräfen and Kuron, 1996; Frankel, 2003).

$$PREN = \%Cr + 3.3\%Mo + 16\%N \quad (\text{eq. 8})$$

It is based on observations that some elements, including Cr, Mo, N, Si, and W, are beneficial alloying elements against pitting corrosion. The concept can be regarded as a helpful decision support tool in a material selection process. However, the  $PREN$  concept is only acceptably tested for stainless steels and not for Nickel- or Titanium alloys. A  $PREN$  of 32 is generally considered as the minimum for seawater pitting resistance of stainless steel (DIN81249-1). When we apply this concept to geothermal situations with even higher salinities and temperatures and usually lower pH, it is evident that a higher  $PREN$  is recommended to provide sufficient resistance.

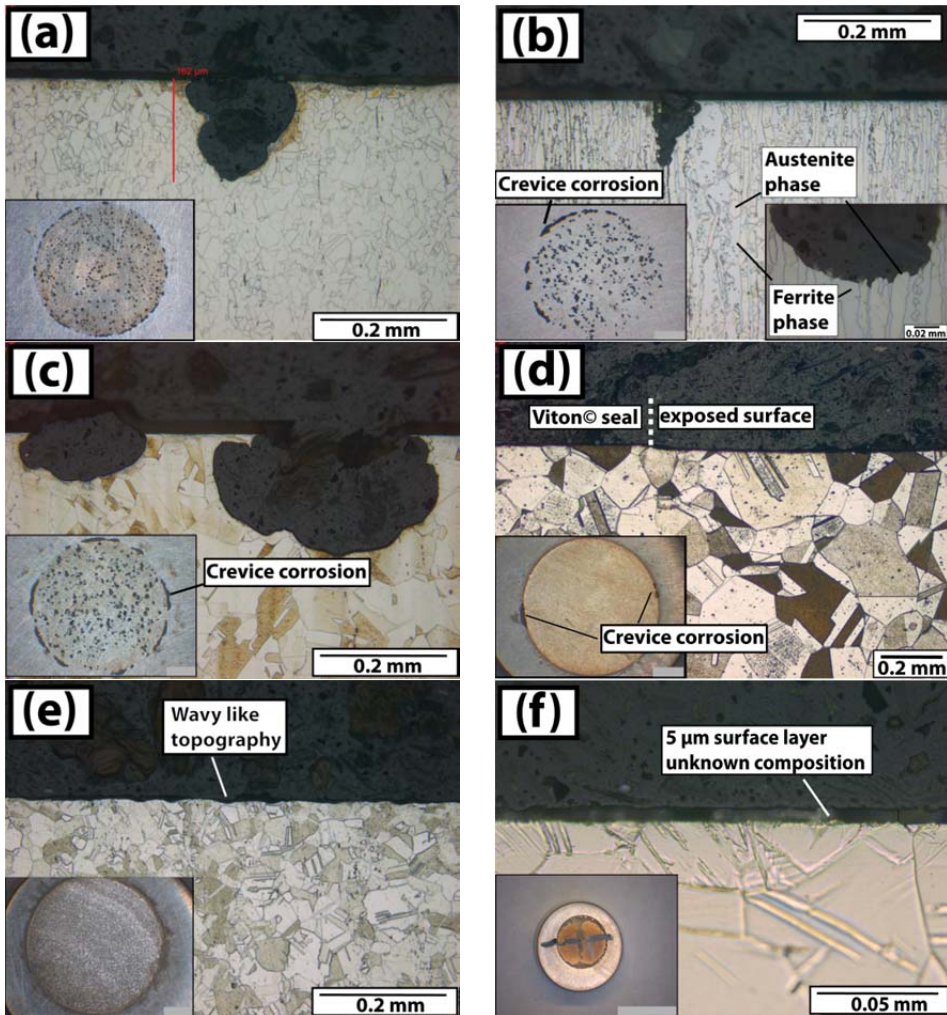


Fig. 25 Optical micrographs of post-polarization samples tested in 80 °C geothermal brine; the diameter of the exposed surface is 0.76 cm<sup>2</sup>; (a) **316L** polarized in Sultz brine to +274 mV and 10<sup>5</sup> µA; (b) **318LN** polarized in Bruchsal brine to +214 mV and 10<sup>5</sup> µA; (c) **904L** polarized in Bruchsal brine to +260 mV and 10<sup>5</sup> µA; (d) **Alloy 31** polarized in Sultz brine to +1239 mV and 10<sup>5</sup> µA; (e) **Alloy 625** polarized in Sultz brine to +1308 mV and 10<sup>5</sup> µA; (f) **Titanium gr. 2** polarized in Sultz brine to +1754 mV and 30 µA.

Fig. 26 shows the  $E_R$ - $OCP$  as a function of the  $PREN$ . A negative value indicates that the  $OCP$  exceeds the  $E_R$  and enters the metastable pitting domain. The grey vertical bar indicates the seawater criterion of  $PREN$  32.

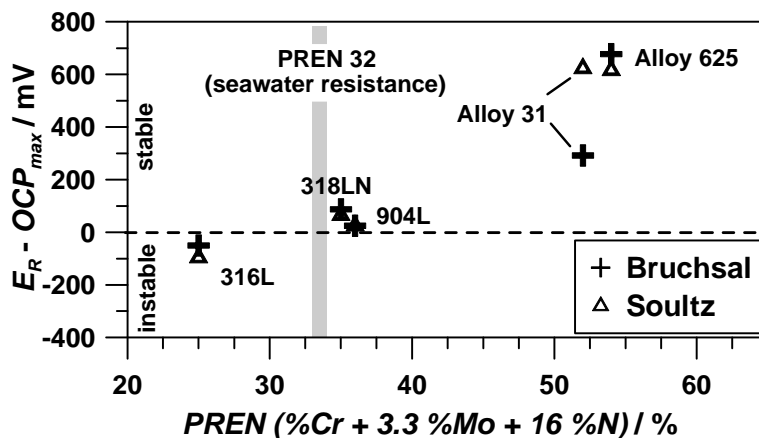


Fig. 26  $E_R$ - $OCP$  vs.  $PREN$  diagram for **316L**, **318LN**, **904L**, and **alloy 31** in Bruchsal and Sultz brine; 80 °C, pH 4.8,  $CO_2$  purged.

The above-mentioned  $PREN$  criterion states insufficient resistance to pitting for **316L** ( $PREN$  25), which could be corroborated by electrochemical results (negative  $E_R$ - $OCP$ ). Fragile passivity is also indicated by very high current densities. The strong fluctuations during the  $OCP$  measurement in Sultz brine, starting at ca. -200 mV, could be clearly correlated with pit growth. A few pits, surrounded by tempering colors, could be found on the post-exposure surface. Note the gap of approx. 25 mV (Sultz) and 10 mV (Bruchsal) between the maximum  $OCP$  value and the corresponding  $E_p$ . The  $OCP$  measurement proved that pitting can also occur at lower potentials than the measured  $E_p$ . Insufficient stability was observed in previous exposure experiments. In the micrographs of post-polarization coupons, both, pitting and shallow pitting could be discerned, while the remainder of the surface is slightly discolored but unaltered (Fig. 25a). The penetration depths can reach 162  $\mu\text{m}$ . It is concluded that **316L** will sooner or later undergo pitting polarization in the environment.

Tab. 14 Electrochemical data derived by measurements in Bruchsal (Br.) and Sultz (S.) brine (80 °C, pH 4.8); P: pitting; U: uniform corrosion; C: crevice corrosion.

Mat'l	PREN %	OCP <sub>max</sub> mV		i <sub>p</sub> μA cm <sup>-2</sup>		E <sub>p</sub> or E <sub>TR</sub> <sup>*</sup> mV		E <sub>R</sub> mV		E <sub>R</sub> -OCP <sub>max</sub> mV		Observed forms of corrosion
		Br.	S.	Br.	S.	Br.	S.	Br.	S.	Br.	S.	
316L	23	<-120	<-100	<10	<12	-110	-75	-170	-196	-50	-96	P
318LN	35	-197	<-190	≈1	<2	-33	5	-110	-135	87	65	P/C
904L	36	<-50 (-220)	<+25	≈2	≈1	35	115	-25	50	25	25	P/C
Alloy 31	52	-92	-23	≈1	≈1	500*	700*	200	600	292	623	U/C
Alloy 625	54	-136	-127	≈1	≈1	530*	600*	480	550	616	677	U
Ti gr. 2	-	-132	-115	≈2	<3	520*	700*	-	-	-	-	-

Both, **318LN** and **904L**, have a *PREN* of 36. **318LN** achieves a stable state of passivation with no major indications of depassivation. The *E<sub>R</sub>-OCP* is positive in both brines, whereas significantly higher in Sultz brine. Post-polarization coupons reveal that primarily shallow pitting with penetration depths <100 μm occur (Fig. 25b). In most cases the attacks occur along austenite-rich zones in the duplex microstructure, which agrees with Deng *et al.* (2008) observations, where pitting corrosion in duplex alloy preferentially occurs in the austenite phase rather than in the ferrite phase. However, this is in contrast to the observation that austenite grains stick out from the pit bottom, and seem therefore to be more resistant (Fig. 25b bottom right). If it comes to corrosion for this material, it will most likely involve crevice corrosion. **904L** shows major depassivation events in the *OCP* measurements, but achieves relatively active *OCPs*. The resulting *E<sub>R</sub>-OCP* is only slightly positive and metastable pitting, although not discernible from the polarization curve, is likely. If it comes to corrosion a mixture of pitting and shallow pitting with maximum penetration depths <200 μm can be expected. It also exhibits an affinity to crevice corrosion. **318LN** is superior to **904L**, which may be related to the beneficial duplex microstructure.

**Alloy 31** (*PREN* 52), **625** (*PREN* 54), and the **Ti alloy** exhibit excellent electrochemical performances. The *OCPs* are very low in comparison to the *E<sub>TR</sub>* and the smooth curves lack indications for depassivation events. The stabilized *OCPs* in both brines are in the stable passivity domain far from transpassivity. It is worth noting that for these alloys a strong current density increase is not related to pitting, but rather to transpassive dissolution. At high anodic overpotentials, oxygen evolution due to water oxidation will occur on the electrode surface, which masks the inherent transpassive

dissolution process (MacDonald, 1999). For **Alloy 31** and **625**, uniform corrosion is the dominant form of attack with a surface recession less than 22  $\mu\text{m}$ . Very smooth and shallow depressions  $<24 \mu\text{m}$  often give the surface a wavy topography. Only **alloy 31** shows an affinity to suffer crevice corrosion which limits its applicability. This observation has also been made by Klapper *et al.* (2011). The **Ti alloy** does not suffer noticeable corrosion, except for a brownish surface discoloration. A 5  $\mu\text{m}$  thick surface film of unknown composition can be observed under the microscope, which is, however, too thick to be the  $\text{TiO}_2$  passive film alone (Fig. 25f).

To evaluate the corrosivity of the geothermal test brines is not straightforward and we obtain ambiguous results. Certainly the pitting potentials are lower in Bruchsal than in Soultz brine, denoting a higher pitting susceptibility. From this observation alone one could state an increased corrosivity of Bruchsal brine. However, the more pronounced *OCP* ennoblement observed in Soultz brine may compensate the difference. The current density is another measure to evaluate the corrosivity, mainly in terms of the passive current density. For **alloy 31**, **625** and **Ti gr. 2** the passive current density is similar. **316L**, **318LN** and **904L** show a deviant behavior and the current is higher in Bruchsal brine than in Soultz brine (**904L**) or vice versa (**318LN**). This obviously contradicts the assumption that a higher salinity weakens the resistance of the passive film and subsequently keeps the metal in a more active state.

There are indications that other mechanisms, associated with the concentrations of minor constituents, are involved, but it remains hard to explain in which way they act or interact and more directed research would be required.

## 9.4 Concluding remarks

The electrochemical measurements discover corrosion and passivation characteristics of different alloys subjected to geothermal brines from Soultz and Bruchsal. The following main conclusions can be drawn:

(1) Spontaneous passivation, expressed by *OCP* ennoblement, is a key process for alloyed materials during the first hours of exposure. The ennoblement shifts the *OCP* away from more active values towards the passive regime. However, this process increases the risk of passivity breakdown, which most likely occurs in the form of pitting corrosion.

(2) Stable passivity is indicated by a harmonic *OCP* equilibration. Unsteady evolution, the occurrence of massive drops and short-term fluctuations (activation/passivation changes) reveal deficient passivity and are related to metastable, or even stable, pit growth.

(3) The range of stable passivation ( $E_R - OCP_{max}$ ) was found to be a good measure to rank the materials according to their pitting resistance.

(4) The combination of electrochemical results, the *PREN* concept, and thermodynamic considerations was useful with regard to a resistance evaluation. Stainless steel **316L** suffers pitting corrosion. **904L** has a higher resistance but is obviously challenged. As for **316L**, corrosion protection of **904L** most likely relies upon  $MoO_2$ . **318LN** shows very good passivation properties. However, the stability of **318LN** and **904L** is limited by the susceptibility to pitting and crevice corrosion. **Alloy 31** shows stable passivation but an increased affinity to crevice corrosion. **Alloy 625** and the **Ti alloy** show stable passivity far from the transpassive domain.

(5) Bruchsal brine is more corrosive in terms of the position of the  $E_p$ . This can be explained by the higher chloride concentration. However, this does not come along with the passive current density, which appears to be more random. Furthermore, the *OCP* ennoblement is more pronounced in Sultz brine and compensates the difference of the  $E_p$ .

## 10 Conclusions

The research campaign was performed in close cooperation with industrial partners from geothermal or energy industry (GEIE and EnBW AG) and steel industry (ThyssenKrupp VDM). The vicinity to operating geothermal sites of the Upper Rhine graben was very beneficial to use the available instrumentation most efficiently and to cooperate in a way that high-relevance aspects are focused. The integrated approach followed in this work is unique for the URG with its enormous geothermal potential. It comprises a physicochemical monitoring campaign, on-site and laboratory experiments, and thermodynamic modeling to corroborate or complement the observed results. Exposure experiments as well as electrochemical polarization methods have been applied in simulated and *in situ* environments.

Through this more integrated approach, this research stands out from research campaigns which are currently conducted by other researchers. It is not only a classical material qualification program but also discovers several processes on the metal-electrolyte interface at elevated temperatures, which account for corrosion and scaling. The output from this research covers different aspects and can be subdivided in rather fundamental and practical findings. Fundamental in a way that observations can now be broken down to basic processes, which depend on the reactivity of the metal-electrolyte interface. Practical in a way, that the outcome provides practical insights into the operation-relevant processes of corrosion and scaling. The results can be implemented in existing systems in order to enhance the reliability of components. The work establishes a framework of background information and gives experiences and results upon which future corrosion research can start. On the basis of the *in situ* brine monitoring in Soultz, which was performed by B. Sanjuan (BRGM), an improved understanding of the brine chemistry could be achieved and a very detailed dataset is now available. Since then, a better characterization and evaluation with regard to the corrosion/scaling potential of the brine is possible.

Following conclusions could be drawn from exposure and electrochemical experiments. Mild steels exhibit long-term uniform corrosion rates below  $0.2 \text{ mm y}^{-1}$ , accompanied by the formation of a corrosion scale which progressively controls the corrosion process. It could be anticipated and later observed on post-exposure coupons that the considered environments lead to the formation of siderite ( $\text{FeCO}_3$ ) from the reaction of the anodically released iron with dissolved carbon species in the brine.

Corrosion of mild steels and the formation of a corrosion scale are inextricably linked. The newly formed corrosion scale, mainly siderite, can have both, beneficial and detrimental properties with regard to the protection of the metal substrate. At higher temperatures the increased rate of siderite deposition decelerates the corrosion rate but promotes localized corrosion forms with considerable penetration depths (e.g. filiform corrosion with more than 1 mm depth) in case of loose or incomplete coverage. It was observed that with increasing exposure time the siderite layer becomes successively dense and adherent.

Autoclave exposure experiments in Soultz brine at different temperatures (20, 80, and 160 °C) reveal a complex interaction between corrosion and scaling on mild steel coupons and both, temperature and time play a significant role. In the considered temperature range the corrosion rate has a local maximum and the corrosion rate is highest in the 80 °C environment. This is mainly due to the retrograde solubility of siderite. A decrease of the corrosion rate over time documents the precipitation of siderite and the build-up of an increasingly protective corrosion scale. A thicker and denser layer of siderite could be observed at higher temperatures, which indicates a higher deposition rate. However, ambiguous observations were made and a generalized statement on the interaction is hard to give. The influence of chemistry, flow conditions, and time on the formation of the corrosion scale requires further investigations.

The observed forms of scaling (siderite, Ba/Sr-sulfates and Pb-sulfides) are in good agreement with what operators observed on a bigger scale. One issue is of special relevance for operators. The newly formed siderite layer has a rough surface and provides the substrate for brine-related scaling (mainly Ba/Sr-sulfates and Pb-sulfides) and a strong adherency was observed. The toxic and radioactive nature of these sulfur deposits has consequences for cleaning procedures and disposal.

Alloys and non-ferrous metals corrode to a much lower extent than mild steels and only weak scale adherency could be observed. However, conventional stainless steels **430F** and **316L** undergo pitting corrosion in 80 °C environments, mainly associated with chemical heterogeneities. Manganese sulfide inclusions in the **430F** microstructure act as preferred pit initiation sites. Post-exposure coupons of **316L** also show pitting on open surfaces. The exposure results could be partly corroborated by electrochemical measurements. Deficient passivity is indicated by an unsteady *OCP* evolution with massive drops and short-term fluctuations (activation/passivation changes). The *OCP* strongly approaches the  $E_R$  and leads to metastable, or even stable, pitting. Higher-alloyed stainless steels **904L** and **318LN** do not undergo pitting corrosion in the 80 °C exposure environment but electrochemical measurements indicate that these alloys are



also challenged. In case of a “zero-corrosion allowance” high-strength CrNiMo alloys with a  $PREN > 36$  or non-ferrous materials, e.g. Titanium, have to be chosen.

The alloyed materials generally show only little weight loss in exposure tests and often remain macroscopically unaltered. Potentiodynamic polarization was used to determine electrochemical potentials, which define the pitting resistance and the repassivation capability of a given metal in a specific environment. The response on polarization also gives a measure about the integrity of the passive film. Furthermore, the evolution of the  $OCP$  has been measured, which reveals the tendency to oxidize in the environment. The concept of comparing the  $OCP$ , the pitting potential, and the repassivation potential has been applied for all metals in original geothermal brines, which is an original piece of work. On the basis of electrochemical measurements a performance ranking could be derived.

The “lack of corrosion” for the higher-strength alloys in weight loss experiments means that no information about the intrinsic corrosion behavior of the alloy is obtained. At this point potentiodynamic polarization was used to exceed the stability limits of the materials and to induce significant corrosion. Now we can assign an intrinsic corrosion behavior for all materials in, simulating extreme conditions. For instance, stainless steels (**430F**, **316L**, **318LN**, and **904L**) are prone to suffer pitting, while **alloy 31** shows uniform corrosion with an increased susceptibility to crevice corrosion. **Alloy 625** and **Ti gr. 2** show uniform corrosion with no localized features of degradation. This information is valuable, regardless of whether or not corrosion is likely to occur spontaneously in the considered environment. This proves that the combined use of methods has an additional benefit and increases the significance of results.

A remark has been made on the comparison of laboratory and *in situ* results. The laboratory environments have therefore been designed to simulate the *in situ* conditions, in terms of temperature, pressure, pH and chemistry. Two conclusions can be drawn: (1) the weight loss in the autoclave is always higher than in the on-site bypass, often increased by a factor of 5; (2) if the mild steels show *Tafel* behavior in the polarization curves, the corrosion rates are in good agreement with on-site results. However, if we review the entire research we can sum up, that the comparison between lab and on-site results often produces ambiguous results and should only be drawn with precaution.

$E_h$ - $pH$  diagrams were conducive to understand the behavior of different thermodynamic systems. By this means, the formation of siderite at elevated

temperatures was predicted and could be observed on post-exposure mild steel coupons. Furthermore, the oxidation behavior of alloying elements, such as chromium and molybdenum could be predicted and reconciled with potentiodynamic polarization results. The breakdown of passivity and the onset of pitting could be comprehended on the basis on these diagrams.

On the basis of the applied methodology fundamental principles on how corrosion takes place in geothermal brine systems could be discovered site-independently. On a regional scale, however, geothermal waters often have more similarities than differences, as so for the URG. Soultz, Bruchsal and other operating and prospected geothermal sites have similar characteristics. It can therefore give some decision-support for selecting materials on a regional scale. The future development of geothermal energy may therefore benefit from this experimental approach to corrosion.

### **10.1 Outlook and perspective**

The interaction of different materials with geothermal brines is a wide topic and many challenges remain to be understood and quantified. The experimental approach from this work will therefore be pursued by further investigations. The results for the 80 °C reinjection environment will be complemented by results carried out in Soultz under production conditions ( $T \approx 165$  °C). For this reason a new bypass system has been installed by GEIE and experiments are currently conducted by Julia Scheiber. The comparison of results from the high-temperature bypass and autoclave experiments up to 200 °C with already available data will allow a more integrated view on the temperature-influenced processes corrosion and scaling. This will help in order to achieve an improved understanding of corrosion, scaling and their interaction.

The construction of a mobile test stand is currently envisaged. This facility would allow to monitor physiochemical parameters and to perform coupon exposure tests. Currently, comparing the results from different sites is difficult since they were acquired under “non-standardized” circumstances. A big step forward would be to establish a monitoring and testing procedure which generates comparable results for different geothermal sites.

The data acquisition from experiments will be complemented by modeling of corrosion processes and scaling. Hereby, experimental results can serve as a benchmark

for modeling results. Based on simplified corrosion and scaling scenarios a stepwise integration of “real world” parameters from natural systems will be pursued in future research.

One aspect which deserves attention is the role of microbiology in geothermal systems. At least on the reinjection side microbial activity has been observed and most probably accounts of sulfide scaling, which forms in sharp contrast to sulfates. Local changes in the redox environment are the most likely reason. Like in many geoenvironments, microbiology acts as a catalyst and accelerates chemical and electrochemical reactions, which is why we hypothesize an influence of microbiology on the corrosion process.

Corrosion engineering and scaling control in geothermal industry is still underdeveloped and will gain importance in the future development of geothermal utilization. Strategies to avoid corrosion and scaling also include the use of inhibitors, which have to be developed and tested. At least with increasing plant size improved strategies to control corrosion and scaling will have to be implemented in order to eliminate downtime periods.



---

## References

- Anderko, A., Sridhar, N., Dunn, D.S., A general model for the repassivation potential as a function of multiple aqueous solution species, *Corros. Sci.* 46 (2004) 1583–1612.
- Aquilina, L., Pauwels, H., Genter, A., Fouillac, C., 1997. Water-rock interaction process in the Triassic sandstone and the granitic basement of the Rhine graben: geochemical investigation of a geothermal reservoir. *Geochimica et Cosmochimica Acta* 61, 4281–4295.
- ASTM G 1-03: Standard practice for preparing, cleaning, and evaluating corrosion test specimens, in: G.S. Haynes, R. Baboian (Eds.) *Laboratory Corrosion Tests and Standards*. ASTM Committee G-1 on Corrosion of Metals, ASTM Special Technical Publication, vol. 866, 1985.
- ASTM G5-82, 1985. Standard practice for standard reference method for making potentiostatic and potentiodynamic anodic polarization measurements. In: Haynes, G.S., Baboian, R. (Eds.), *Laboratory Corrosion Tests and Standards*. ASTM Committee G-1 on Corrosion of Metals. ASTM Special Technical Publication 866, pp. 513–521.
- Bäßler, R., Burkert, A., Kirchheiner, R., Saadat, A., Finke, M., *Proceedings of NACE Corrosion 2009*, Paper No. 09377, NACE International, Atlanta 2009.
- Baticci, F., 2009. Material study on geothermal EGS (Enhanced Geothermal System) power plant: application to the Soultz-sous-Forêts site. Diploma thesis of the Politecnico di Milano, Italia, Facolta di Ingegneria Industriale, p. 202.
- Baticci, F., Genter, A., Huttenloch, P., Zorn, R., 2010. Corrosion and scaling detection in the Soultz EGS power plant, Upper Rhine graben, France. In: *Proceedings World Geothermal Congress, Bali, Indonesia, 25–29 April*, p. 11.
- Baumgärtner, J., Menzel, H., Hauffe, P., The Geox GmbH project in Landau, The first geothermal power project in Palatinate / Upper Rhine valley, at First European Geothermal Review, *Geothermal Energy for Electric Power Production*, Mainz, Germany, 2007.
- Bénézech, P., Dandurand, J.L., Harrichoury, J.C., Solubility product of siderite ( $\text{FeCO}_3$ ) as a function of temperature (25–250 °C), *Chem. Geol.* 265 (2009) 3–12.
- Bertani, R., *Geothermal energy: an overview on resources and potential*, IGA Geothermal workshop, Istanbul (2009).
- Birch, F., Heat from radioactivity, in: H. Faul (Ed.), *Nuclear Geology*, Wiley, New York (1954) pp. 148–174.
- Blasco-Tamarit, E., Igual Munoz, A., Garcia Anton, J., Garcia-Garcia, D., Effect of temperature on the corrosion resistance and pitting behaviour of **Alloy 31** in LiBr solutions, *Corrosion Science* 50 (2008) 1848-1857.
- BMWi, *Die Energiewende in Deutschland*, Bundesministerium für Wirtschaft und Technologie, Berlin (2012).

- Burgassi, P., Cappetti, G., One Hundred Years History of Geothermal Power Production at Larderello, IGA News 56 (2004) 5-6.
- Burstein, G.T., Electrochemistry of Pit Formation, Electrochemical Society Joint International Meeting, Honolulu, 2004.
- Burstein, G.T., Passivity and localized corrosion, in: Shreir's corrosion Volume 2, Corrosion in Liquids, Corrosion evaluation, Cottis, B., Graham, M., Lindsay, R., Lyon, S., Richardson, T., Scantlebury, D., Stott, H. (Eds.), Elsevier Publishing (2010).
- Carter, J.P., Cramer, S.D., Materials of Construction for High-Salinity Geothermal Brines, U.S. Department of the Interior, Report of Investigations 8792, 1992.
- Conover, M., Ellis, P., Curzon, A., Material selection guidelines for geothermal power systems – An overview, in: L.A. Casper, T.R. Pinchback (Eds.), Geothermal Scaling and Corrosion, vol. 717, ASTM Special Technical Publication, 1980, pp. 24–40.
- Conrad, R.K., Carter, J.P., Cramer, S.D., Corrosion of Selected Metals and a High-Temperature Thermoplastic in Hypersaline Geothermal Brine, U.S. Department of the Interior, Report of Investigations 8792, 1983.
- Cook, W.G., Olive, R.P., Pourbaix diagrams for chromium, aluminum and titanium extended to high-subcritical and low-supercritical conditions, Corrosion Science 58 (2012) 291-298.
- Czernichowski-Lauriol, I., Fouillac, C., The chemistry of geothermal waters: its effects on exploitation, Terra Nova 3 (1991) 477–491.
- DeBerry, D.W., Ellis, P.F., Thomas, C.C., Material Selection Guidelines for Geothermal Power Systems, first ed., ALO-3904-1, EG-77-C-04-3904, US Department of, Energy, 1978.
- Deng, B., Jiang, Y., Gong, J., Zhong, C., Gao, J., Li, J., Critical pitting and repassivation temperatures for duplex stainless steel in chloride solutions, Electrochimica Acta 53 (2008) 5220-5225.
- DeWarrd, C., Lozt, U., Prediction of CO<sub>2</sub> corrosion of carbon steel, Corrosion/93 NACE, Paper No. 69, NACE International, Houston, TX, 1993.
- Dinh, H.T., Kuever, J., Mußmann, M., Hassel, A.W., Stratmann, M., Widdel, F., Iron corrosion by novel anaerobic microorganisms, Nature 427 (2004) 829–832.
- DiPippo, R., Geothermal Power Plants, 3<sup>rd</sup> edition: Principles, Applications, Case Studies and Environmental Impact, Elsevier Ltd. 2012.
- Ellis, A.J., Mahon, W.A.J., Chemistry and Geothermal Systems, Academic Press, New York, 1977.
- Fournier, R.O., Chemical geothermometers and mixing models for geothermal systems, Geothermics 5 (1977) 41-50.
- France Jr., W.D., 1969. Controlled potential corrosion tests, their applications and limitations. Test Methods Forum, Materials Research and Standards, 21–26.

- 
- Frankel, G.S., Electrochemical Techniques in Corrosion: Status, Limitations, and Needs, *Journal of ASTM International* 5 (2008).
- Frankel, G.S., Pitting Corrosion, in: Cramer, S.D. and Covino, B.S. (Eds.), *Metals Handbook Vol. 13A*, ASM International, 2003.
- Frick, S., Regenspurg, S., Kranz, S., Milsch, H., Saadat, A., Francke, H., Brandt, W., Huenges, E., 2011. Geochemical and process engineering challenges for geothermal power generation. *Chemie-Ingenieur-Technik* 83 (12), 2093–2104.
- Gallup, D.L., Geochemistry of geothermal fluids and well scales, and potential for mineral recovery, *Ore Geol. Rev.* 12 (1998) 225–236.
- Genter, A., Evans, K., Cuenot, N., Fritsch, D., Sanjuan, B., Contribution of the exploration of deep crystalline fractured reservoir of Soultz to the knowledge of enhanced geothermal systems (EGS), *C. R. Geoscience* 342 (2010) 502–516.
- Gentier, S., Rachez, X., Peter, M., Blaisonneau, A., Sanjuan, B., Transport and Flow Modelling of the Deep Geothermal Exchanger Between Wells at Soultz-sous-Forêts (France), in: *Proceedings of the Geothermal Research Council (GRC) Annual Meeting*, San Diego, USA, 2011, 12 pp.
- Gerard, A., Menjot, A., Schwoerer, P., L'anomalie thermique de Soultz-sous-Forêts, *Geotherm. Actual* 3 (1984) 35–42.
- Gräfen, H., Kuron, D., Pitting corrosion of stainless steels, *Mater. Corros.* 47 (1996) 16–26.
- Gupta, H., Roy, S., *Geothermal Energy*, first edition, Elsevier Publishing Amsterdam, 2007.
- Gutman, E.M., Zamostyanik, I.E., Karpenko, G.V., Microelectrochemical heterogeneity of Ferritic–Pearlitic structures, *Fiz.-Khim. Mekh. Mater.* 5 (1969) 509–510.
- Han, J., Galvanic Mechanism of Localized Corrosion for Mild Steel in Carbon Dioxide Environments, Ph.D. Thesis, Department of Chemical and Biomolecular Engineering, Russ College of Engineering and Technology of Ohio University, 2009.
- Han, J., Nescic, S., Yang, Y., Brown, B.N., Spontaneous passivation observations during scale formation on mild steel in CO<sub>2</sub> brines, *Electrochimica Acta* 56 (2011) 5396–5404.
- Han, J., Young, D., Colijn, H., Tripathi, A., Nescic, S., Chemistry and structure of the passive film on mild steel in CO<sub>2</sub> corrosion environments, *Ind. Eng. Chem. Res.* 48 (2009) 6296–6302.
- Herzberger, P., Tiefengeothermisches Projekt Bruchsal, Diploma thesis of the University of Karlsruhe, Germany, (2008), p. 182.
- Heuer, J.K., Stubbins, J.F., An XPS characterization of FeCO<sub>3</sub> films from CO<sub>2</sub> corrosion, *Corros. Sci.* 41 (1999) 1231–1243.
- Hoffmann, M.R., *Brine Chemistry – Scaling and Corrosion*, Geothermal Research Study in the Salton Sea Region of California, California Institute of Technology, 1975.

- Hooijkaas, G.R., Genter, A., Dezayes, C., Deep-seated geology of the granite intrusions at the Soultz EGS site based on data from 5 km-deep boreholes, *Geothermics* 35 (2006) 484–506.
- Huenges, E., *Geothermal Energy Systems: Exploration, Development and Utilization*, Wiley-VCH (2010).
- Igual Munoz, A., Garcia Anton, J., Lopez Nuevalos, Guinon, J.L., Perez Herranz, V., Corrosion studies of austenitic and duplex stainless steels in aqueous lithium bromide solution at different temperatures, *Corrosion Science* 46 (2004) 2955-2974.
- Ilevbare, G.O., Burstein, G.T., The role of alloyed molybdenum in the inhibition of pitting corrosion in stainless steels, *Corrosion Science* 43 (2001) 485-513.
- IPCC Special report, O. Edenhofer, Pichs-Madruga R., Sokona Y., Seyboth K., Matschoss P., Kadner S., Zwickel T., Eickemeier P., Hansen G., Schloemer S., von Stechow, C. (Eds.), Cambridge University Press, Cambridge, United Kingdom and New York, NY, USA, 1075 pp.
- Karlsdottir, S.N., Corrosion, scaling and material selection in geothermal power production, in: A. Sayigh (Ed.), *Comprehensive Renewable Energy*, vol. 7 *Geothermal Energy*, Elsevier Publishing, 2012, pp. 239–258.
- Klapper, H.S., Bäßler, R., Weidauer, K., Stuerzbecher, D., Evaluation of Suitability of High-Alloyed Materials for Geothermal Applications in the North German Basin, *Proceedings of the NACE 2011*, Vol. 68, NACE International, Houston, TX.
- Klapper, H.S., Bäßler, R., Sobetzki, J., Weidauer, K., Stürzbecher, D., Corrosion resistance of different steel grades in the geothermal fluid of Molasse Basin, *Mater. Corros.* 63 (2012).
- Kohl, T., Bächler, D., Rybach, L., Steps towards a comprehensive thermo-hydraulic analysis of the HDR test site Soultz-sous-Forêts, *Proc. World Geothermal Congress, Kyushu-Tohoku, Japan* (2000) 3459-3464.
- Landolt, D., *Corrosion and Surface Chemistry of Metals*, EFPL Press (2007).
- Leckie, H.P., Uhlig, H.H., Environmental factors affecting the critical potential for pitting 18-8 stainless steel, *J. Electrochem. Soc.* 113 (1966) 1262-1267.
- Lichti, K.A., Soylemezoglu, S. and Cunliffe, K.D., *Geothermal Corrosion and Corrosion Products*, New Zealand Geothermal Workshop 1981.
- Linter, B.R., Burstein, G.T., Reactions of pipeline steels in carbon dioxide solutions, *Corros. Sci.* 41 (1999) 117–139.
- Lopez, D.A., Perez, T., Simison, S.N., 2003. The influence of microstructure and chemical composition of carbon and low alloy steels in CO<sub>2</sub> corrosion. A state-of-the-art appraisal. *Materials and Design* 24, 561–575.
- Lu, Y.C., Ives, M.B., Clayton, C.R., Synergism of alloying elements and pitting corrosion of stainless steels, *Corrosion Science* 35 (1993) 89-96.



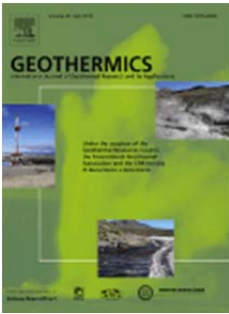

- MacDonald, D., Theory of the Transpassive State, 1999.  
<http://www.electrochem.org/dl/ma/206/pdfs/0812.pdf>
- MacDonald, D.D., Syrett, B.C., Wing, S.S., The use of potential-pH diagrams for the interpretation of corrosion phenomena in high salinity geothermal brines, NACE Corrosion 35 (1) (1979) 1–11.
- McCawley, F.X., Cramer, S.D., Riley, W.D., Carter, J.P., Needham, P.B., Corrosion of Materials and Scaling in Low-Salinity East Mesa Geothermal Brines, U.S. Department of the Interior, Report of Investigations 8504, 1981.
- Mergner, H., Eggeling, L., Kölbel, T., Münch, W., Genter, A., Geothermische Stromerzeugung: Bruchsal und Soultz-sous-Forêts, Mining + Geo 4 (2012) 666–673.
- Miller, R.L., Chemistry and materials in geothermal systems, in: L.A. Casper, T.R. Pinchback (Eds.), Geothermal Scaling and Corrosion, vol. 717, ASTM Special Technical Publication, 1980, pp. 3–10.
- Miranda-Herrera, C., Saucedo, I., Gonzalez-Sanchez, J., Acuna, N., Corrosion degradation of pipeline carbon steels subjected to geothermal plant conditions, Anti-Corros. Methods Mater. 57 (4) (2010) 167–172.
- MIT report, J. Tester *et al.*, The future of geothermal energy, Massachusetts Institute of Technology (2006). Available at: [http://www1.eere.energy.gov/geothermal/pdfs/future\\_geo\\_energy.pdf](http://www1.eere.energy.gov/geothermal/pdfs/future_geo_energy.pdf)
- Mundhenk, N., Huttenloch, P., Kohl, T., Steger, H., Zorn, R., Metal corrosion in geothermal brine environments in the Upper Rhine graben - laboratory and *in situ* studies -, Geothermics 46 (2013) 14–21.
- Mundhenk, N., Huttenloch, P., Sanjuan, B., Kohl, T., Steger, H., Zorn, R., Corrosion and scaling as interrelated phenomena in an operating geothermal power plant, Corros. Sci. 70 (2013) 17–28.
- Nesic, S., Lee, K.-L.J., A mechanistic model for carbon dioxide corrosion of mild steel in the presence of protective iron carbonate films—Part III: The film growth model, J. Corros. 5 (9) (2003) 616.
- Neville, A., Hodgkiess, T., An assessment of the corrosion behavior of high-grade alloys in seawater at elevated temperature and under a high velocity impinging flow, Corrosion Science 38 (1996) 927–956.
- Olsson, C.-O.A., Landolt, D., Passive films on stainless steels - chemistry, structure and growth, Electrochimica Acta 48 (2003) 1093–1104
- Palacios, C.A., Shadley, J.R., Characteristics of corrosion scales on steels in a CO<sub>2</sub>-saturated NaCl brine, NACE Corrosion 47 (1991) 122–127.
- Pauwels, H., Fouillac, C., Fouillac, A.M., Chemistry and isotopes of deep geothermal saline fluids in the Upper Rhine Graben: origin of compounds and water-rock interactions, Geochim. Cosmochim. Acta 51 (1993) 2737–2749.
- Pfennig, A., Bäßler, R., Effect of CO<sub>2</sub> on the stability of steels with 1% and 13% Cr in saline water, Corros. Sci. 51 (2009) 931–940.

- Pfennig, A., Kranzmann, A., Effect of CO<sub>2</sub> and pressure on the stability of steels with different amounts of chromium in saline water, *Corrosion Science* 65 (2012) 441-452.
- Pfennig, A., Wiegand, R., Wolf, M., Bork, C.-P., Corrosion and corrosion fatigue of AISI 420C (X46Cr13) at 60 °C in CO<sub>2</sub>-saturated artificial geothermal brine, *Corrosion Science* 68 (2013) 134-143.
- Phillips, S.L., Mathur, A.K., Garrison, W., Treatment methods for geothermal brines, in: L.A. Casper, T.R. Pinchback (Eds.), *Geothermal Scaling and Corrosion*, vol. 717, ASTM Special Technical Publication, 1980, pp. 207–224.
- Pohjanne, P., Carpen, L., Hakkarainen, T., Kinnunen, P., A method to predict pitting corrosion of stainless steels in evaporite conditions. *Journal of Constructional Steel Research* 64 (2008) 1325–1331.
- Pound, B.G., Abdurrahman, M.H., Glucina, M.P., Wright, G.A., Sharp, R.M., 1985. The corrosion of carbon steel and stainless steel in simulated geothermal media. *Australian Journal of Chemistry* 38, 1133–1140.
- Pourbaix, M., *Lectures of Electrochemical Corrosion*, Plenum Press, New York-London, 1973. 336 pp, ISBN 0-306-30449-X.
- Pribnow, D., Schellschmidt, R., 2000. Thermal tracking of upper crustal fluid flow in the Rhine graben. *Geophysical Research Letters* 13 (27), 1957–1960.
- Roine, A., *Outokumpu HSC Chemistry\_6.0 User's Guide Volume 1/2 – Chemical Reaction and Equilibrium Software with Extensive Thermochemical Database and Flowsheet Simulation* Outokumpu Research Finland, 2006.
- Sanjuan, B., Millot, R., Dezayes, C., Brach, M., Main characteristics of the deep geothermal brine (5 km) at Soultz-sous-Forêts (France) determined using geochemical and tracer test data, *CR. Geosci.* 342 (2010) 546–559.
- Sanjuan, B., Soultz EGS Pilot Plant Exploitation – Phase III: Scientific Program about *In situ* Operations of Geochemical Monitoring and Tracing (2010–2013). First Yearly Progress Report BRGM/RP-59902-FR, 2011, 92 pp.
- Sanjuan, B., Soultz EGS Pilot Plant Exploitation – Phase III: Scientific Program about *In situ* Operations of Geochemical Monitoring and Tracing (2010–2013). Second Yearly Progress Report BRGM/RP-61030-FR, 2012, 48 pp.
- Scheiber, J., Nitschke, F., Seibt, A., Genter, A., Geochemical and mineralogical monitoring of the geothermal power plant in Soultz-sous-Forêts (France), in: *Proceedings 37th Workshop on Geothermal Reservoir Engineering*, Stanford University, California, 2012.
- Scheiber, J., Ravier, G., Sontot, O., Hensch, C., Genter, A., In Situ Material Studies at the High Temperature Skid (HTS) Bypass System of the Geothermal Power Plant in Soultz-sous-Forêts, France, *Proceedings: Workshop on Geothermal Reservoir Engineering*, Stanford Geothermal Workshop, 2013.

- 
- Schmitt, G., Rothman, R., Corrosion of unalloyed and low alloyed steels in carbonic acid solution, *Mater. Corros.* 29 (1978) 237–245.
- Sedriks, J., *Corrosion of Stainless Steels*, Sponsored by the Electrochemical Society, Wiley, New York, 1979. 282 pp, ISBN 0-471-05011-3.
- Shoosmith, D.W., Noël, J.J., Corrosion of Titanium and its alloys, in: *Shreir's Corrosion*, Volume 3, 2010, Pages 2042-2052.
- Stern, M., Geary, L.A., 1957. Electrochemical polarization: I, a theoretical analysis of the shape of polarization curves. *Journal of the Electrochemical Society* 104, 56–62.
- Stober, I., Jodocy, M., Hydrochemical characteristics of deep-seated waters in the Upper Rhine Graben, *Z. geol. Wiss.* 39 (2011) 39-57.
- Surbeck, H., Assessment of Radiological Risks at the Geothermal Pilot Plant Soultz-sous-Forêts. First results. CHYN technical report, University of Neuchâtel, Switzerland, 2008.
- Thomas, R., Titanium in the geothermal industry, *Geothermics* 32 (2003) 679–687.
- Wang, W., Zhang, X., Wang, J., Pits with coloured halos formed on 1Cr18Ni9Ti stainless steel surface after ennoblement in seawater, *Material Science and Engineering C* 29 (2009) 851-855.
- Zhao, G., Lu, X., Xiang, J., Han, Y., Formation Characteristic of CO<sub>2</sub> corrosion product layer of API P110 steel investigated by SEM and electrochemical techniques, *J. Iron. Steel Res. Int.* 16 (2009) 89–94.
- Zhao, G., Lu, X., Xiang, J., Han, Y., Formation Characteristic of CO<sub>2</sub> corrosion product layer of API P110 steel investigated by SEM and electrochemical techniques, *J. Iron. Steel Res. Int.* 16 (2009) 89–94.
- Zhu, S.D., Fu, A.Q., Miao, J., Yin, Z.F., Zhou, G.S., Wei, J.F., Corrosion of API N80 carbon steel in oil field formation water containing CO<sub>2</sub> in the absence and presence of acetic acid, *Corros. Sci.* 53 (2011) 3156–3165.
- Ziegler, P.A. (1992): *European Cenozoic rift system - Tectonophysics*, 208, S. 91-111.



## Declaration of authorship

<p style="text-align: center;"><b>Study 1</b></p> 	<p><b>Authors:</b> Niklas Mundhenk, Thomas Kohl, Hagen Steger (all KIT), Petra Huttenloch, Roman Zorn (both European Institute for Energy Research, Karlsruhe)</p> <p><b>Citation:</b> N. Mundhenk, P. Huttenloch, T. Kohl, H. Steger, R. Zorn, Metal corrosion in geothermal brine environments of the Upper Rhine graben – Laboratory and on-site studies, <i>Geothermics</i> 46 (2013) 14-21.</p> <p><b>Declaration of authorship:</b> Niklas Mundhenk (NM) planned and conducted the experiments in cooperation with Petra Huttenloch (PH). Hagen Steger and Roman Zorn were responsible for the setup of the laboratory devices. NM evaluated the results in consultation with PH and wrote the manuscript. The final manuscript was reviewed by all authors, particularly by Thomas Kohl.</p>
<p style="text-align: center;"><b>Study 2</b></p> 	<p><b>Authors:</b> Niklas Mundhenk, Thomas Kohl, Hagen Steger (all KIT), Petra Huttenloch, Roman Zorn (both European Institute for Energy Research, Karlsruhe), Bernard Sanjuan (Bureau de Recherches Géologiques et Minières (BRGM), Orléans, France)</p> <p><b>Citation:</b> N. Mundhenk, P. Huttenloch, B. Sanjuan, T. Kohl, H. Steger, R. Zorn, Corrosion and scaling as interrelated phenomena in an operating geothermal power plant, <i>Corrosion Science</i> 70 (2013) 17–28</p> <p><b>Declaration of authorship:</b> Niklas Mundhenk (NM) planned and conducted the experiments in cooperation with Petra Huttenloch (PH). Hagen Steger and Roman Zorn were responsible for the setup of the laboratory devices. Bernard Sanjuan contributed the data from the <i>in situ</i> brine monitoring. NM evaluated the results in consultation with PH and wrote the manuscript. The final manuscript was reviewed by all authors, particularly by Thomas Kohl.</p>
<p style="text-align: center;"><b>Study 3</b></p>	<p><b>Authors:</b> Niklas Mundhenk, Thomas Kohl, Hagen Steger (all KIT), Petra Huttenloch, Roman Zorn (both European Institute for Energy Research, Karlsruhe), Ralph Bäßler (Federal Institute for Material testing and research, BAM)</p> <p><b>Citation:</b> To be submitted July 2013 (<i>Corrosion Science</i>, <i>Electrochimica Acta</i>, or <i>Materials and Corrosion</i>)</p> <p><b>Declaration of authorship:</b> Niklas Mundhenk (NM) planned and conducted the experiments in cooperation with Petra Huttenloch (PH). Hagen Steger and Roman Zorn were responsible for the setup of the laboratory devices. NM evaluated the results in consultation with PH and Ralph Bäßler and wrote the manuscript. The final manuscript was reviewed by all authors, particularly by Thomas Kohl.</p>



## Acknowledgements

This work developed with the well-meaning help and support of many people. I would like to thank...

...my supervisor Prof. Dr. Thomas Kohl for “adopting” me in his working group and for his good advice in various situations, both in good and bad times.

...Prof. Dr. Landolt for his marvelous publications and for his uncomplicated willingness to be the co-referent.

...Leif Wolf, Hagen Steger, and Detlev Rettenmaier for giving me the chance to do a PhD at the KIT. Leif left soon, but Hagen and Detlev accompanied me on my way.

...Petra Huttenloch for her invaluable help and her accurateness in laboratory affairs. I still owe you a dinner with “Ziegra-Knobelsdorf memorial beer”. Tell me the date!

...the many researchers who established the methods and principles this work relies on.

...Roman Zorn who was always keen for a quick discussion and was a big help in technical issues.

...Albert Genter and Julia Scheiber from GEIE for their well-meaning cooperation and fruitful discussions.

...ThyssenKrupp VDM for providing high-strength materials which were used for our research.

...Thomas Kölbel (EnBW AG) for his advice and support and for his confidence.

...the BMU (Federal Ministry for the Environment, Nature Conservation and Nuclear safety) for project funding (FKZ: 0325111C).

...Pia Orywall for her review and always having an open ear for me and my issues, Felix, Thilo and Tom for giving me a residence in the final phase. Thank you, Miss “chocolate-banana-cake” for your vividness and for the good times.

...Caro for her constant tea supply and Robin for his endurance in standing my humor during the final phase of the dissertation.

...and last but not least my family for their invaluable background support.

...and all the others to whom I owe gratitude, both personally and professionally.





## Curriculum Vitae

### Personal information

Name: Niklas Johann Caspar Mundhenk  
Date of birth: 01/15/1981  
Place of birth: Hamburg  
Nationality: Germany

### Education

1987 – 1990 Primary school Steinfeld  
1990 – 2001 Secondary school Klaus Harms (Kappeln) and  
Friedrich List (Lübeck)  
2001 University entrance diploma

### Civilian service

2001 - 2002 Lebenshilfe, Bad Schwartau

### Academic studies

2002 - 2009 Albert-Ludwigs University, Geological Institute,  
Freiburg  
**Diploma degree in Geology**  
Thesis: “Impact of CO<sub>2</sub>-rich waters on the  
mineralogy and alteration of clastic sediments in the  
Middle Rhine region“

### Professional experience

2009-2013 **PhD position**  
Institute for Applied Geosciences, working group  
Geothermics (Prof. T. Kohl)  
Karlsruhe Institute of Technology  
Thesis: “Corrosion and scaling in geothermal  
operation / Material qualification for geothermal  
service / Electrochemistry of engineering materials

Oct.-Nov. 2011 &  
Feb.-Mar. 2012 Visiting scientist, Energy & Geoscience Institute,  
Salt Lake City, Utah (USA)

### **Publications in peer-reviewed journals**

Mundhenk, N., Huttenloch, P., Kohl, T., Steger, H., Zorn, R., Metal corrosion in geothermal brine environments in the Upper Rhine graben - laboratory and *in situ* studies, *Geothermics* 46 (2013) 14–21.

Mundhenk, N., Huttenloch, P., Sanjuan, B., Kohl, T., Steger, H., Zorn, R., Corrosion and scaling as interrelated phenomena in an operating geothermal power plant, *Corrosion Science* 70 (2013) 17-28.

Mundhenk, N., Huttenloch, P., Kohl, T., Steger, H., Zorn, R., Electrochemical study on corrosion of different alloys exposed to deaerated 80 °C geothermal brines containing CO<sub>2</sub>, *Electrochimica Acta* (to be submitted June 2013).

### **Other publications (co-author)**

LOGRO final report (2013), Detlev Rettenmaier, Emmanuel Gaucher, Julia Ghergut, Petra Huttenloch, Thomas Kohl, Jörg Meixner, Niklas Mundhenk, Gerd Möllmann, Kerstin Rauppach, Manfred Rinke, Martin Sauter, Andrea Seibt, Hagen Steger, Markus Wolfgramm, Roman Zorn, BMU project FKZ 0325111 A.

### **Conference contributions**

Mundhenk, N., Huttenloch, P., Kohl, T., Steger, H., Zorn, R., Laboratory and *in situ* corrosion studies in geothermal environments, *GRC Transactions* 36 (2012) 1101-1105. (**Publication in Proceedings + Presentation**).

Mundhenk, N., Huttenloch, P., Kohl, T., Steger, H., Zorn, R., Corrosion and scaling in geothermal environments – Identifying suitable materials, *International Geothermal Conference*, May 2013. (**Invited talk**).

Mundhenk, N., Huttenloch, P., Korrosion metallischer Werkstoffe unter geothermischen Bedingungen, *Deutscher Geothermiekongress 2010*. (**Presentation**).

Mundhenk, N., Corrosion and Scaling in geothermal systems, *French and German Ph.D. student day 2013*. (**Presentation**).

Mundhenk, N., Huttenloch, P., Scheiber, J., Genter, A., Zorn, R., Corrosion and scaling in the geothermal cycle of Soultz-sous-Forêts, France, *NACE 2014 San Antonio*. (**Accepted for presentation & Proceedings**).